Philipps Universität Marburg

Chemical vapor deposition and physical characterization of gallium and carbon-related structures on Si (001) and GaP/Si (001) templates for the growth of graphene layers

Dissertation

zur
Erlangung des Doktorgrades
der Naturwissenschaften
(Dr. rer. nat.)

dem

Fachbereich Physik
der Philipps-Universität Marburg

vorgelegt von

Katharina Werner

aus

Zomba (Malawi)

Marburg/Lahn, 2015

Vom Fachbereich Physik der Philipps-Universität Marburg
als Dissertation angenommen am: 08.09.2015
Erstgutachter: Herr Dr. habil. Wolfgang Stolz
Zweitgutachter: Herr Prof. Dr. Wolfram Heimbrodt
Tag der mündlichen Prüfung: 30.09.2015
Hochschulkennziffer 1180

Contents

List of acronyms

3% HF	dilute hydrofluoric acid
30% HCl	dilute hydrochloric acid
96% H_2SO_4	concentrated sulphuric acid
a.u.	arbitrary units
AFM	atomic force microscopy
Al	aluminium
APBs	anti-phase boundaries
APCVD	atmospheric pressure chemical vapor deposition
Ar	argon
C	carbon
C_2H_2	acetylene
C_2H_4	ethylene
CH_4	methane
Co	cobalt
Cs	cesium
Cu	copper
CVD	chemical vapor deposition
EDX	energy dispersive X-ray spectroscopy
Fe	iron
FME	flow rate modulated epitaxy
Ga	gallium

GaP	gallium phosphide
Ge	germanium
GFR	gas-foil-rotation
H	hydrogen
$\mathbf{H_2}$	molecular hydrogen
$\mathbf{H_2O}$	water
$\mathbf{H_2O_2}$	hydrogen peroxide
HAADF	high angle annular dark field
$\mathbf{HNO_3}$	nitric acid
HOPG	highly oriented pyrolytic graphite
iLO	in-plane longitudinal optical
Ir	iridium
iTO	in-plane transversal optical
LPCVD	low pressure chemical vapor deposition
LPE	liquid phase epitaxy
MBE	molecular beam epitaxy
MFC	mass flow controller
ML	monolayer
$\mathbf{N_2}$	molecular nitrogen
$\mathbf{NH_4OH}$	ammonium hydroxide
Ni	nickel
nm	nanometer
O	oxygen
P	phosphorous
Pd	palladium
PIPS	precision ion polishing system

PE	primary electron
P_P	partial pressure
Pt	platinum
Ru	ruthenium
S	sulphur
SE	secondary electron
SEM	scanning electron microscopy
Si	silicon
SiC	silicon carbid
SiH_4	monosilane
SIMS	secondary ion mass spectrometry
STEM	scanning transmission electron microscopy
STM	scanning tunnelling microscopy
TEM	transmission electron microscopy
TBEthyne	tert-butylethyne
TBEthylene	tert-butylethylene
TBP	tert-butylphosphine
TEGa	triethylgallium
TMGa	trimethylgallium
UHV	ultra-high vacuum

CHAPTER 1

Introduction

In 2004, Andre Geim and Konstantin Novoselov successfully isolated graphene, a two-dimensional form of carbon [1]. A mere six years later, in 2010 they were awarded the Nobel Prize in Physics for their ground-breaking experiments with this material [2]. This unusually swift recognition by the Nobel Committee underscores the tremendous expectations and hopes placed on this new material in the field of solid state physics.

After it was found possible to produce graphene, an increasing number of work groups initiated studies in this special field of research. The exploratory focus of these groups varies from the production of high-quality, large-area graphene films or large quantities of graphene flakes to the detailed investigation of the experimental properties of graphene or a targeted manipulation of particular characteristics, such as electronic properties. The strong interest in this remarkable material is revealed by the steep rise in the number of publications per year on this topic, which has increased exponentially from next to none prior to 2005 to well over 18,000 in 2014 [3].

Above all, the electronic properties of graphene have attracted the interest of fundamental research and industry. This is due to its particular band structure in which the valence and conduction band touch in six conical points at the boundaries of the Brillouin zone (see section 2.1.1). As a consequence, the charge carriers behave like mass-less Dirac fermions for low-energy excitation of graphene [4]. Such Dirac fermions could only be studied theoretically until graphene was discovered and give rise to the occurrence of such phenomena as the half-integer quantum Hall effect [5]. In addition, the charge carrier mobility in graphene is unusually high as ballistic transport occurs and charge carriers can travel up to sub-micrometer distances without scattering. The mobility remains high even for increasing charge carrier concentrations and temperatures. A potential electric mobility limit of 200,000 $\frac{\mathrm{cm}^2}{\mathrm{Vs}}$ was predicted theoretically. While this limit is still out of reach, room-temperature mobility of up to 140,000 $\frac{\mathrm{cm}^2}{\mathrm{Vs}}$ was measured for graphene layered in a heterostructure with boron nitride [6]. This value is larger by two magnitudes than the room-temperature electron mobility in silicon of 1,400 $\frac{\mathrm{cm}^2}{\mathrm{Vs}}$ [7]. Additionally, the position of the Fermi energy can be adjusted in single layer graphene by applying an electric field, and charge carriers can be tuned continuously between electrons and holes; this is known as ambipolar electric field effect. Numerous graphene-based devices, such as transistors or transparent electrodes, enter the realm of feasibility due to these particular electronic characteristics. Therefore, it is not astonishing that market-leaders such as Samsung, IBM or Google are investing in this high-potential material and battling to acquire the patents that might revolutionize electronic devices of the future.

Besides its electronic properties, the mechanical and elastic characteristics of graphene are remarkable. Graphene was calculated to possess a mechanical strength that outreaches any other known material. At the same time, one square meter of graphene weighs only roughly one thousandth of one square meter of paper. Being formed by a single layer of carbon, this extremely stable and light carbonic material has captivated the attention of the aerospace sector, including such companies as Airbus and Boeing, as well as research facilities like NASA. Various additional applications for graphene are imaginable and are being developed, such as gas sensors, liquid crystal displays, water filtration systems, anti-corrosion coatings and batteries. Despite this, until now graphene has only found its way into commercial use as support for samples prepared for transmission electron microscopy, while some other graphene based devices such as flexible transparent conductors or humidity sensors have reached a prototype, demonstration stage [8]. One reason the commercialization of graphene is lagging behind its potential is the difficulty of producing graphene on suitable substrates for each application. Nowadays, researchers have found ways to produce high-quality graphene or graphene flakes (see section 2.1.3). Until now though, the production of graphene for particular devices has generally been connected to a transfer of the carbon layer from a growth substrate to an appropriate target substrate. This transfer, however, is accompanied by a potential reduction in the graphene's quality due to arising defects and especially by an increase in production costs due to an additional production stage. At present complementary metal-oxide-semiconductor electronics are based on Si (001) substrates. If graphene could directly be deposited on Si (001), the advantages of graphene could be combined with these widely used devices.

This study, therefore, focuses on the direct deposition of graphene on silicon (001) by chemical vapor deposition. At present, chemical vapor deposition of graphene is realized primarily on transition metals such as copper or nickel. Transition metals, however, can induce deep defects in semiconductor crystals and therefore reduce the electronic and optical performance of these materials. To avoid such contamination, this study approaches the deposition of graphene by using the catalytic effect of gallium, a standard material in silicon technology, on the growth of this two-dimensional carbonic material. This catalytic effect was shown before for a different growth method [9]. Applying this technique to the deposition of graphene on silicon, however, requires a profound understanding of gallium deposition and the characteristics of gallium on silicon.

While the epitaxial growth of gallium-containing crystalline semiconductors on silicon was discussed in many studies, the processes during the deposition of pure metallic gallium were scarcely investigated. Therefore, the deposition of gallium on silicon (001) was investigated for two standard precursors triethylgallium and trimethylgallium, and will be discussed in the present study. A special focus was put on analyzing the interaction between gallium and silicon, for example by identifying preferred deposition sites induced by the silicon structure, or by investigating a potential alloying of the two compounds. Additionally, possibilities for tailoring the characteristics of the deposited gallium, for example by adjusting the deposition temperature, were examined and will be introduced. Combining gallium deposition with gallium phosphide growth was studied, which can prevent direct contact between the metallic gallium or the graphene and the silicon substrate. This might be of significance since the melt-back etching effect of Ga etching into silicon is known for the deposition of gallium-containing alloys, such as gallium nitride, on silicon [10]. While this was mostly observed for the relatively high growth temperatures used for gallium nitride growth, the possible occurrence of a similar effect for deposition of pure gallium on silicon might reduce the quality of the gallium-pretreated silicon surface. Besides comparing the characteristics gallium exhibits on silicon to those it shows on gallium phosphide, the deposition of a few layers of gallium phosphide and pure phosphorous on silicon was also analyzed. The influence of post-growth annealing was investigated for all mentioned materials, as a chemical vapor deposition of graphene is expected to require growth temperatures in the range of several hundred degrees Celsius. The results obtained were then applied to study the chemical vapor deposition of carbon on silicon or, more explicitly, on the differently pretreated silicon surfaces. These results build an important foundation for the growth of graphene on silicon-based semiconductor surfaces. Additionally, new insights into the formation of interfaces between silicon and gallium-containing alloys, such as gallium phosphide, were gained.

The following parts of this thesis are divided into four sections. Chapter 2 gives a short overview of the most important physical foundations of this study. In this section, the characteristics of graphene, the chemical vapor deposition of graphene on substrates such as copper or nickel, and the silicon (001) surface will be presented. An introduction of the experimental methods used for sample preparation and characterization is given in Chapter 3. Chemical vapor deposition was used to prepare all samples in this study. Atomic force microscopy, scanning tunnelling microscopy and scanning electron microscopy were utilized to analyze the sample surfaces, scanning transmission electron microscopy to examine the crystal structure and energy dispersive X-ray spectroscopy as well as secondary ion mass spectrometry for an investigation of the composition. Additionally, Raman spectroscopy was applied to identify ordered carbon structures after deposition. The results of this study are displayed and discussed in Chapter 4, which represents the main part of this thesis. The preparation of silicon (001) and gallium phosphide (001) surfaces is examined as well as the deposition of gallium, phosphorous, and carbon with various precursors on these substrates. The last section, Chapter 5, gives a summary of the most important results and makes recommendations for prospective investigations.

CHAPTER 2

Physical foundations

This chapter describes the physical foundations, that build the motivation for this study as well as the basis for the sample growth and the sample analysis performed for this research. Since this study aimed to deposit graphene on silicon (Si) (001), the first part of this overview, section 2.1.1, illustrates the basic properties of graphene, with respect to its crystal structure as well as mechanical and electronic properties, i.e., its band structure. The vibrational modes of graphene will be discussed in section 2.1.2. Since these modes are characteristic for graphene and change for small variations in the crystal structure, analysing these modes by means of Raman spectroscopy allows conclusions on the properties of the examined graphene. Section 2.1.3 summarizes the current knowledge on the chemical vapor deposition (CVD) of graphene, which is the foundation for the experiments performed for this study. The Si (001) surface was used as substrate for deposition and the surface structure will have an influence on any structures grown. Therefore, the structure of this particular surface is described in section 2.2.
Obviously not all physical foundations for this research can be described in the framework of this study and only a brief insight can be given. A more detailed overview on semiconductors can be found in [11]. An extensive discussion of CVD and crystal growth is given in [12] and [13].

2.1 Graphene

2.1.1 Structural, mechanical and electronic properties of graphene

Basically speaking, graphene is a two-dimensional allotrope of carbon (C). It is formed by a single layer of C atoms, which are bonded in-plane via sp^2-hybridization. A simplified illustration of this hybridization is given in fig. 2.1. Hybridization describes a mixing of the atomic orbitals. The C ground state configuration is $1s^2\ 2s^2\ 2p^2$, as C holds 2 core and 4 valence electrons. To form covalent bonds, one electron can be excited from the doubly occupied 2s state to the empty 2p state. This results in the C^* state with four singly occupied orbitals, as shown in image 2.1 (a). For sp^2-hybridization the 2s-orbital combines with only two of the three available 2p-orbitals, forming three equivalent sp^2-hybrid-orbitals and leaving the third 2p-orbital unchanged. This is pictured in fig. 2.1 (b). Each orbital still contains a single unpaired electron. The three sp^2-orbitals are coordinated in a trigonal planar geometry, while the last, unhybridized p-orbital is oriented orthogonal to them. This is illustrated in (c) from top and side view.

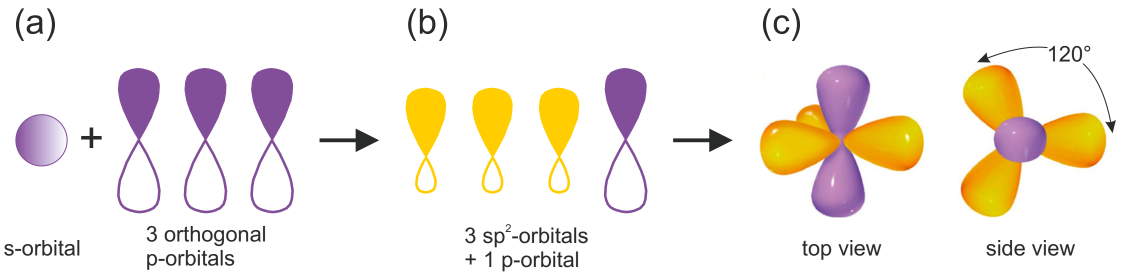

Figure 2.1: Scheme of the sp^2-hybridization, partly taken from [14]. An excited C* atom with one singly occupied 2s and three singly occupied 2p-orbitals (a) can form three sp^2-orbitals leaving the third p-orbital unaffected (b). The three sp^2-orbitals will be coordinated in-plane separated by 120° angles, while the remaining p-orbital is coordinated out-of-plane (c).

Each C atom therefore has three covalent, in-plane σ-bonds, with a bond length of 1.42 Å, formed by the sp^2-hybrid-orbitals. Another delocalized out-of-plane π-bond is formed by the remaining p-orbital. The C atoms are tightly packed into a hexagonal arrangement with a two-atom basis, known as honeycomb lattice. The lattice structure of graphene in real space is depicted schematically in fig. 2.2 (a). It is built up by two equivalent sublattices A and B, which are visualized in the image by blue and red atoms respectively. One unit cell, containing a basis of two C atoms, is highlighted in yellow. The graphene lattice constant, i.e., $|\vec{a_1}|$ and $|\vec{a_2}|$, is 2.46 Å.

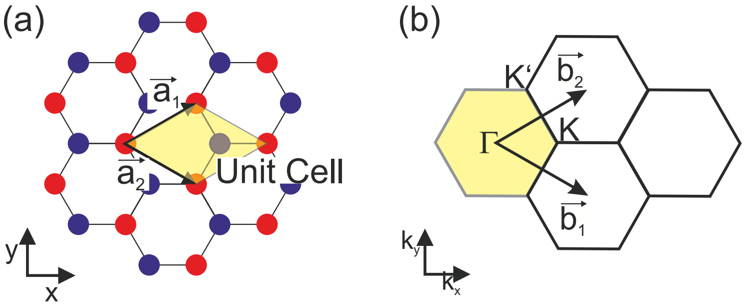

Figure 2.2: Scheme of the lattice structure of graphene in real (a) and in reciprocal space (b); adapted from [15].

The reciprocal lattice of graphene in momentum space is displayed in fig. 2.2 (b). The highly symmetrical unit cell, known as the Brillouin zone, is again highlighted in yellow. The corners of this Brillouin zone, the $\bar{K}$- and the $\bar{K}'$-point, are of great importance for the electronic properties of graphene, as will be discussed later. Image 2.3 displays a stack of three graphene layers. Such a formation of multiple layers of graphene is known as graphite. The single graphene sheets are separated by a distance of 3.55 Å and bond only by weak van der Waals forces.

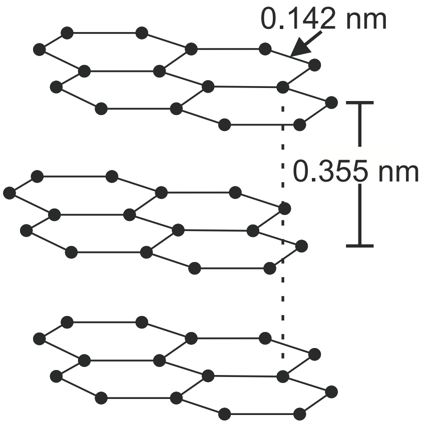

Figure 2.3: Schematic presentation of a graphene stack

Therefore, the exfoliation and isolation of single graphene sheets is possible, due to the strong intra- but weak interlayer bonds. Besides the two-dimensional graphene and three-dimensional graphite, other forms of carbon, such as quasi-zero-dimensional fullerenes or quasi-one-dimensional nanotubes are known. Graphene is the basic building block for all these structures, as they can be formed by rolling or stacking of graphene sheets. Diamond, another prominent C formation, on the other hand, differs from these structures, as the C atoms are tetrahedrally coordinated in a three-dimensional formation. Therefore, diamond is formed by sp^3-bonded C atoms. This means that each C atom exhibits four tetrahedrally coordinated hybrid-orbitals. The so-called diamond cubic crystal structure can be built by two face-centered cubic lattices, which are shifted by $\frac{1}{4}$ of the body diagonal of the unit cell.

The combination of extraordinary mechanical and electronic properties observed in graphene [16] attracted great interest in this particular material for applications as well as for basic research. The activation energy for defect formation in C nanotubes, the rolled-up modification of graphene, was calculated to be well beyond that of other known materials [17]. This implies an intrinsic strength that considerably exceeds that of other materials, since this energy determines the mechanical resistance to an applied tension. The calculations made for C nanotubes were later transferred to flat graphene, which led to similar results [18]. In reality the strength of experimentally available graphene is usually reduced in comparison to the calculated ideal value, due to the presence of defects and grain boundaries in the crystal structure. However, the exceptional mechanical strength of defect-free graphene, which is caused by the short and stable covalent σ-bonds, was verified experimentally by nanoindentation in an atomic force microscopy (AFM) [19]. Additionally, graphene is an extremely light material with a weight of merely 0.77 mg per square meter, since it consists only of an atomically thin mesh of C atoms [20]. This makes it an ideal material, for example, for aerospace applications, once large-area graphene can be produced with a low defect density.

The electronic properties of graphene, however, attract an even larger interest in this remarkable material. These properties are founded on the C's unhybridized p-orbitals, which form delocalized out-of-plane π-bonds with neighbouring atoms. Only electrons from these orbitals contribute to charge carrier transport in graphene. Since each p-orbital is initially occupied by one unpaired electron, a filled valence band π and a unfilled conduction band π^* are formed. A scheme of the three-dimensional π-band structure in reciprocal space, calculated using the tight-binding approach [21], is displayed in fig. 2.4.

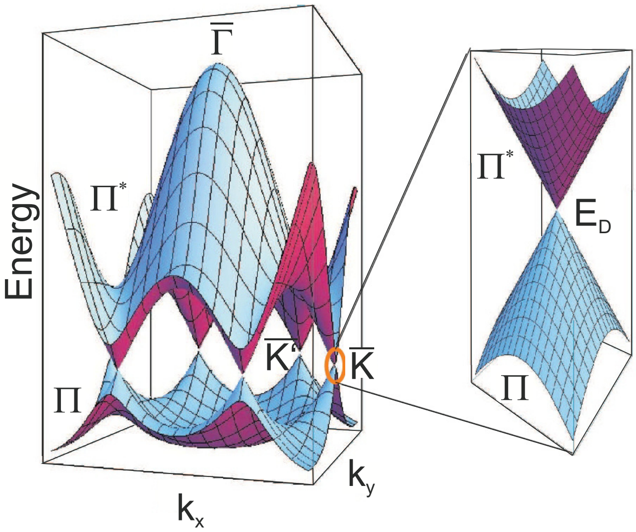

Figure 2.4: Illustration of the three-dimensional π-band structure of graphene in reciprocal space; taken from [15].

The valence band and the conduction band of graphene touch in conical points at the $\bar{K}$- and the $\bar{K}'$-points of the Brillouin zone. No energy gap appears, making graphene a zero-gap semiconductor or zero-overlap semimetal. Remarkable is the fact that the π-bands display a linear dependency on the wave vector around the $\bar{K}$- and the $\bar{K}'$-points. Therefore, charge carriers in graphene are described by the Dirac equation rather than the Schrödinger equation and, thus, behave like mass-less Dirac fermions. For this reason, the six corners of the Brillouin zone are referred to as Dirac points. Their energy position, the Dirac energy E_D, is exactly at the Fermi level E_F, as the π-band is completely filled, while the π^*-band is completely empty. This exceptional band structure is a direct consequence of the symmetry of the graphene's crystal lattice, consisting of two equivalent sublattices. Cosine-like energy bands, which are related to the two sublattices, cross close to the edges of the Brillouin zone [22]. An extremely high carrier mobility for the so-called π-electrons in these bands was predicted theoretically by the tight-binding approximation [21] and verified experimentally by field effect and magnetoresistance measurements [1]. Electronic conductivity, however, is rather low for perfect graphene, due to the zero density of states at the Dirac points. This can be overcome by doping, as this changes the position of the Fermi level. This position can also be tuned by supplying an external electrical field, as pictured schematically in image 2.5, displaying the dependency of the band structure of graphene at a Dirac point and its sheet resistivity on an external voltage.

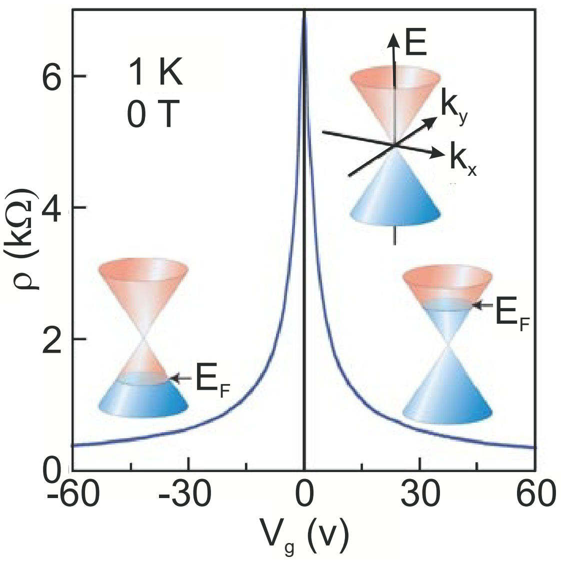

Figure 2.5: Illustration of the ambipolar electric field effect in graphene; taken from [22].

The position of the Fermi level can be shifted below or above the Dirac point, into the valance and the conduction band respectively, by applying a negative or a positive gate voltage V_g. This so-called ambipolar field effect induces a considerable quantity of free carriers. Additionally, charge carriers can be tuned continually between electrons and holes. The sheet resistivity ρ is at a maximum if no electric field is applied and decreases with increasing voltage, as an increasing number of charge carriers is available.

While strictly by definition graphene relates only to a single layer of C atoms, it is often also used for bilayer or few layer graphene. The electronic properties just discussed, however, can only be found in single layer graphene and to a good approximation in bilayer graphene. It was shown that the electronic structure rapidly evolves with the number of layers, approaching the 3D limit of graphite at 10 layers.

2.1.2 Vibrational modes of graphene

Raman spectroscopy describes the interaction of light with the lattice vibrations, which are referred to as phonons. It utilizes the inelastic scattering of photons at these vibrations. The scattered photons either lose energy by creating a phonon (Stokes Raman scattering) or gain energy while absorbing the energy of a phonon (anti-Stokes Raman scattering). The photon's energy shift corresponds to the energy differences between two vibrational states of the interacting system and is characteristic for the vibrational modes of this system. First measurements of the Raman spectrum of graphene were published in 2006 [23], [24]. It was soon found that the investigation of the vibrational modes of carbonic material could not only be used to identify graphene, but also to thoroughly analyse the characteristics of the studied material. The Raman peaks of graphene-type structures noticeably change in dependency of particular characteristics, such as the number of graphene layers or the defect density [23].

The phonon dispersion relation of graphene is displayed in fig. 2.6. Since graphene possesses a two-atomic basis, its dispersion relation contains six branches; three of these are acoustic branches (A) and three are optic branches (O). They are divided into out-of-plane (o) or in-plane (i) as well as into longitudinal (L) and transversal (T) motions. Transversal modes describe vibrations which move along the C-C bonds for the Γ-point mode. Longitudinal modes vibrate perpendicular to these bonds for the Γ-point mode. Only the three optic branches contribute to Raman scattering. The interaction of light with acoustic phonons is referred to as Brillouin scattering. This scattering can also be detected with a sufficiently well resolving monochromator system, but affects the scattered phonons to a lesser degree than Raman scattering.

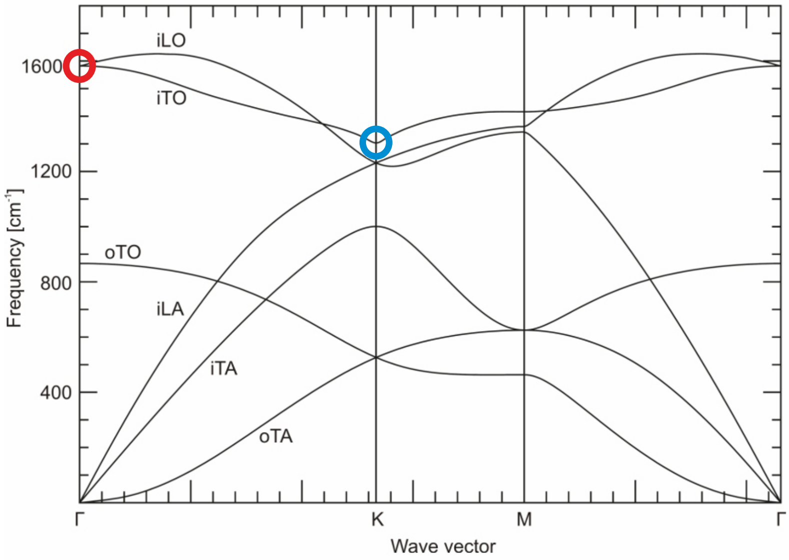

Figure 2.6: Phonon dispersion relation of graphene; taken from [25].

Only phonons close to the Γ-point of the Brillouin zone, i.e., phonons with a momentum $q \approx 0$, can be active for first-order (one-phonon) Raman scattering of visible light. Such a first-order scattering process occurs at the doubly-degenerate zone-center in-plane C-C stretching mode, and gives rise to the so-called G band. Thereby “G” refers to graphite, since this peak always appears for graphite samples. The band frequency, of approximately $1580\,\mathrm{cm}^{-1}$, and the momentum of this mode are highlighted by the red circle at the Γ-point in fig. 2.6. A visual representation of the two degenerated G band vibrations, an in-plane transversal optical (iTO) and an in-plane longitudinal optical (iLO) mode, is shown in fig. 2.7 (a). The electronic process of this one-phonon Raman scattering is displayed in fig. 2.7 (b). A virtual electron-hole pair is resonantly excited by an incident photon. The electron or the hole is scattered by either of the Γ-stretching modes, before the electron-hole pair radiatively recombines, emitting a photon. The emitted photon is red shifted by the energy, that was given to the phonon.

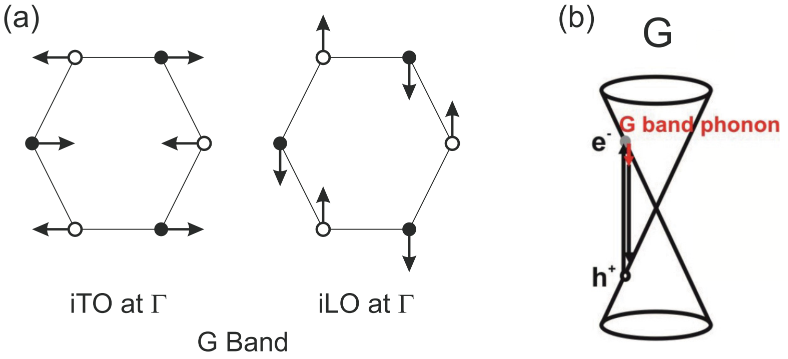

Figure 2.7: Scheme of the degenerated Γ-point in-plane C-C stretching modes (a); adapted from [26]. Illustration of the Raman process leading to the G band; taken from [27].

Fig. 2.6 exposed a second optic phonon, an oTO, at the Γ-point with a frequency of approximately 870 cm^{-1}. However, this phonon is not Raman active, but can be seen by infrared absorption spectroscopy.

Zone-boundary phonons, i.e., phonons with a momentum $q \neq 0$, are also Raman allowed, when higher-order or defect-induced Raman scattering processes are considered. For graphene such processes can occur at the zone-boundary in-plane breathing mode of the C$_6$-ring. An illustration of this breathing mode, an iTO mode at the K-point, is displayed in fig. 2.8 (a). The band frequency, of approximately 1350 cm^{-1}, and the momentum of this vibrational mode are highlighted by the blue circle at the K-point in fig. 2.6.

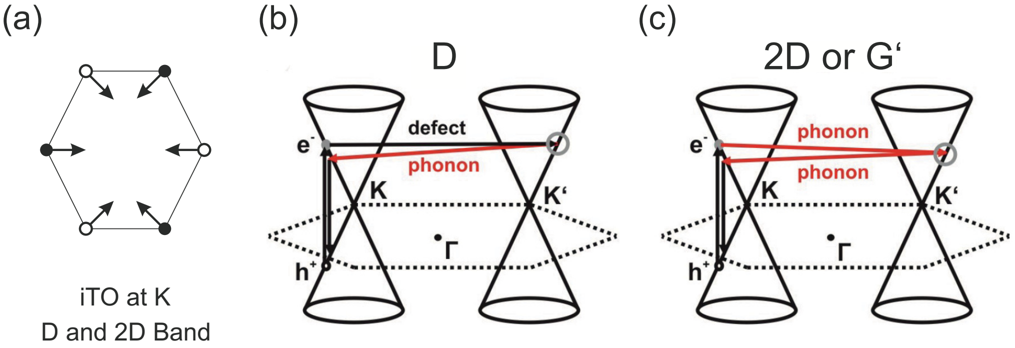

Figure 2.8: Display of the zone-boundary in-plane breathing mode of the C$_6$-ring (a); adapted from [26]. Visualisation of the scattering processes leading to the D (b) and 2D (c) Raman band of graphene; taken from [27].

Two different scattering processes can occur at this vibrational mode and give rise to the defect-induced D band at 1350 cm^{-1} ("D" referring to defect) as well as to the second-order 2D band at 2700 cm^{-1}. The electronic process resulting in the D band is shown in fig. 2.8 (b). An electron-hole pair is created by an incident photon. The electron is inelastically scattered to the K'-point by a C breathing phonon and then back-scattered to the K-point by a defect before recombining. The back-scattering process obtains the conservation of the momentum in this Raman process. The same process can also occur for a hole instead of an electron. The D band only appears in the presence of crystal defects, such as sp^3-bonds, vacancy sites, grain boundaries or lattice edges. It, therefore, contains information about the quality of the studied graphene.

The generation of the 2D band involves two phonons with opposite momentum. This second-order Raman process is displayed in fig. 2.8 (c). As for the D band, an electron-hole pair is resonantly excited by an incident photon and the electron is then scattered to the K'-point by the iTO phonon. For the 2D band the electron is then back-scattered by a second iTO phonon with a momentum in the opposite direction before recombining. As two scattering processes at iTO phonons occur, the energy shift of the photon is twice as high as for the D band. Based on the similarity of the scattering process to that of the D band, this band is called 2D band. However, no defects are involved, which is why this band is often also called G' band, as it always occurs in high-quality graphene, too.

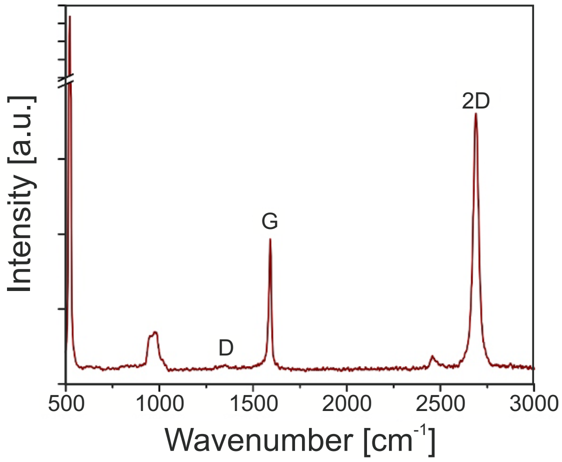

Figure 2.9: Raman spectrum of graphene transferred to a oxidized Si substrate; taken from [28].

The result of a Raman measurement performed on a graphene sample, which was transferred onto an oxidized Si substrate, is exemplarily displayed fig. 2.9. The G as well as the 2D band can clearly be observed. The D band, which only occurs in the presence of a sufficient amount of defects, for example, at the edges of a graphene sheet is hardly recognizable. Other bands originating from the Si substrate appear at 522 cm^{-1} and 960 cm^{-1}. Additional higher-order scattering events can occur in graphene and generate peaks in the Raman spectrum. As these exhibit low intensities for perfect graphene, though, they do not need to be considered in this case. Changes in the crystal structure of the graphene, however, lead to significant variations of the vibrational modes and can therefore be detected by Raman spectroscopy [29]. Some examples for this will be given

in the following:
Uniaxial stretching of graphene lifts the degeneration of the iTO and iLO mode at the Γ-point. The G band splits into a G^- and a G^+ band.
Doping induces a change of the Fermi level near the K-point and therefore results in a shift of the G band as well as in a shift of the 2D peak. Additionally, the intensity of the 2D peak decreases with increasing doping level.
A single 2D peak can only be observed for single layer graphene. The changes in the electronic structure of graphene with an increasing number of graphene layers strongly influences this band. The number of possible scattering processes increases and numerous peaks appear, which are close in frequency. At the same time the intensity of this peaks decreases with an increasing number of layers. The 2D peak shape and the ratio of intensities of the G peak to the 2D peak is therefore an indication of the number of graphene layers.

While the G and 2D band always occur in high-quality graphene, the G and D band are always observed for any sp^2-bonded C_6-ring structures. Also for amorphous C films without a widespread graphitic ordering [23], [30]. This is due to the resonance between the incident photons and the π-states of the sp^2-bonds, which therefore strongly contribute to the visible Raman spectrum. Although the occurrence of the G and D peak in a Raman spectrum reveals the presence of sp^2-bonded C_6-rings, a widespread graphitic ordering in the investigated sample can only be assumed when the G as well as the 2D band appear. This is at least true for undoped material, as any doping reduces the intensity of the 2D peak.

2.1.3 Chemical vapor deposition of graphene

The first theoretical study on graphene was already published in 1947, where this two-dimensional material was used to approximate the electronic structure of graphite [21]. Theoretical investigations on graphene proceeded from thereon, as it is the starting point for calculations on graphite, C nanotubes or fullerenes. Long it was thought, though, that a strictly two-dimensional structure was thermodynamically unstable and could not exist [31], [32]. Only in 2004 graphene was isolated experimentally for the first time [1]. In this study flakes of graphene were produced by mechanical exfoliation from highly oriented pyrolytic graphite (HOPG). Meanwhile, this method is known as “Scotch tape method”. High-quality graphene flakes can be produced quickly and easily by this technique and can then be applied to any suitable substrate. By now, graphene flakes can be obtained in the kilogram scale by the so-called liquid-exfoliation method, which involves the dispersion of graphite in a liquid. However, preparing large or well defined layers is not possible by exfoliation. Nowadays several other ways are known to produce graphene. Large and homogeneous graphene films can be obtained by a high-temperature annealing of silicon carbid (SiC), which leads to a sublimation of Si [33]. Graphene can subsequently form on the surface. However, this technique is bond to SiC substrates and high annealing temperatures. Another promising approach is the CVD of graphene on transition metal substrates such as copper (Cu) ([34], [35], [36]), nickel (Ni) ([37], [38], [39]), ruthenium (Ru) ([40], [41]), platinum (Pt) ([42], [43]) or cobalt (Co) ([44], [45]). An overview of the CVD growth of graphene on transition metals will be given here. More detailed information can be found in [13].

Graphene deposition on metal substrates is performed in a ultra-high vacuum (UHV) set-up with in situ characterization in some studies (e.g. [46], [40]), for a profound insight into the growth process. For larger scale graphene growth mostly tube furnace style growth chambers are utilized. These are typically build by a quartz glass tube, which can be equipped with the metal substrate and is enclosed by a clamshell style heater. A hydrocarbon gas, such as methane (CH_4), ethylene (C_2H_4) or acetylene (C_2H_2), is used as C precursor. This C source is diluted in a carrier gas, often times a mixture of molecular hydrogen (H_2) and argon (Ar). Two different graphene growth processes can occur for this deposition, depending on the solubility of C in the particular substrate, i.e., the amount of C that can diffuse into the substrate material [47]. These two growth processes are illustrated schematically in fig. 2.10.

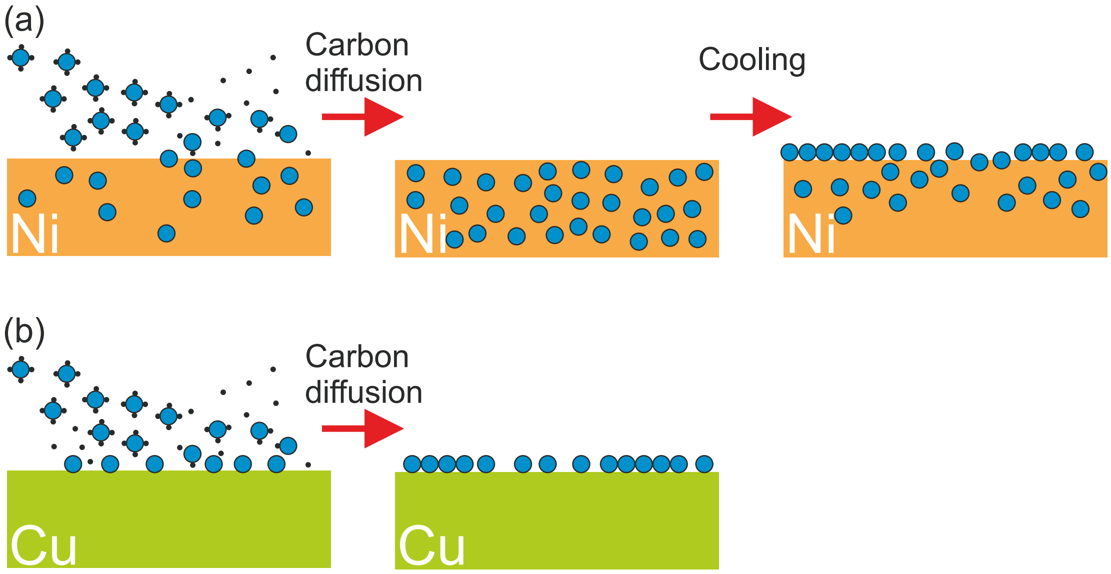

Figure 2.10: Scheme of the graphene growth process on Ni (a) (adapted from [38]) and on Cu (b).

A catalytic decomposition of the C precursor at the hot metal surface occurs for both deposition processes. For the usage of a substrate with a high solubility of C (depicted in fig. 2.10 (a)), such as Ni [48], Ru [49] or Pt [50], the C diffuses into the bulk material at the deposition temperature. For a sufficient C dose, a cool-down results in a supersaturation of the substrate with C, since the C solubility of the substrate declines with decreasing temperature. C precipitates out upon cooling and forms a graphene film on the surface at suitable conditions, such as an appropriate cooling rate and reactor pressure during the cooling.

When a metal substrate with a low solubility of C is used (illustrated in fig. 2.10 (b)), such as Cu [51] or iridium (Ir) [49], only small amounts of C can be dissolved in the bulk. Graphene formation starts at nucleation sites, such as surface roughness, impurities, and metal grain boundaries [52]. The growth proceeds via surface diffusion and attachment of C to the edges of the graphene film.

The latter process bears the important advantage of being self limiting, as no catalytic decomposition can proceed once the substrate is fully covered with graphene. The formation of a uniform graphene monolayer (ML) on substrates with a high C solubility requires a careful adjustment of the growth parameters, since more C can be dissolved in the bulk than required for a single graphene layer. A high cooling rate or a metal film with a controlled low thickness can be used to suppress the precipitation of too much C and the formation of multiple graphene layers. Besides the difference in the graphene growth process, based on the differing C solubility in various metals, the substrates also effect the structural quality of the graphene layer. A weak or a strong interaction between the substrate and the forming graphene layer will exist for different metals [53]. Strong interaction primarily occurs between the out-of-plane π-orbitals of the graphene and the metal d bands and is observed, for example, for Ni [54] or Ru [40]. The first graphene layer is chemisorbed on these substrates. On Cu or Pt only physisorption occurs for graphene. Interaction might, for example, lead to a distortion of the graphene layer. Additionally, some metals, such as iron (Fe), have a significant tendency for carbide formation which might conflict with the formation of high-quality graphene layers [55]. Ni and Cu are currently the most prominently used metal substrates for the different growth processes, thus, C deposition has been studied extensively for these. Graphene formation will therefore be discussed in more detail for these two metals in the following.

Formation of graphene on nickel:

As mentioned before, Ni exhibits a high solubility of C, absorbing approximately 0.9 atomic percent C at 900 °C [47]. Also, Ni (111), which has a lattice constant of 2.49 Å, provides one of the smallest lattice mismatches of any transition metals to graphene, which has a lattice constant of 2.46 Å for HOPG [56]. For these reasons Ni (111) substrates have been used for the growth of multilayer graphitic films for decades [57], [58]. Graphene growth is nowadays performed primarily on Ni (111) to achieve homogeneous large-area graphene layers, but growth of graphene on other surfaces, such as Ni (011) or polycrystalline Ni, is also possible [59]. The deposition temperature plays an important roll for the growth of high-quality graphene layers, since varying C modifications will form. Three temperature ranges can be differentiated, since the carbide phase of Ni is stable only for temperatures below 460 °C, while graphene is stable up to 650 °C [55]. At temperatures above 650 °C, any C will dissolve in the Ni until saturation is achieved and no material growth proceeds at the surface. For growth temperatures between 460 °C and 650 °C only carbide dissolves in Ni and graphene can nucleate on the surface. As the graphene phase is energetically favourable above the carbide phase, graphene, which is once formed, is stable for all temperature below 650 °C. For graphene growth on Ni a C precursor is supplied at a temperature above 650 °C in most cases. After a sufficient concentration of C is reached in the Ni substrate, a controlled cool-down is performed. Graphene precipitates out in the temperature range between 460 °C and 650 °C. For temperature below 460 °C, though, carbide formation appears more rapidly than graphene growth, indicating a significant kinetic barrier for the latter. For this reason, a carbide rather than a graphene phase will form at temperatures below 460 °C. This C phase, however, can slowly be transformed into graphene by annealing at a temperature below 460 °C and continuously supplying the C precursor. At these conditions the C atoms offered can slowly exchange with the Ni atoms in the carbide phase [60].

Formation of graphene on copper:
Cu is currently the most widely used metal substrate for CVD growth of graphene. As previously mentioned, this is mostly due to the fact that the low solubility of C in Cu allows for a comparatively simple deposition of single rather than multiple layers of graphene on large-area Cu foils. Since such Cu foils of sufficient quality are readily purchasable and inexpensive, significant successes were reached in this field in the recent years [34], [35]. Growth on Cu foils, however, leads to a formation of polycrystalline graphene, which results in a reduced quality for electronic applications as grain boundaries induce scattering of electrons and holes and therefore result in lower charge carrier mobilities. For high-quality graphene layers a low density of nucleation sites is required, since this leads to an increased grain size. Growth of homogeneous graphene can be realized on single-crystal Cu substrates. However, this suffers from the disadvantage of the considerably higher costs of the growth substrates in comparison to Cu foils.

The largest drawback, though, which concerns the CVD deposition of graphene on all metal substrates, is the need of transferring the layers to a different, suitable substrate for further investigation or applications, once they are formed. Isolating samples, for example, are required for electronic measurements. This transfer is performed by dissolving the metal substrate after graphene growth in most cases. Exemplarily, one possible transfer method is depicted in fig. 2.11. For this method, a graphene layer, which was deposited on a metal substrate, is initially spin coated with a polymer, such as poly(methyl methacrylate) (PMMA). A polymer layer, known as polymer stamp, forms on the graphene. The metal substrate is selectively dissolved subsequently in a wet chemical bath. The graphene layer along with the polymer support remains floating in the solvent and can be transferred to the target substrate from there. Once the graphene layer is applied to the target substrate, the polymer can also be dissolved by another wet chemical etchant.

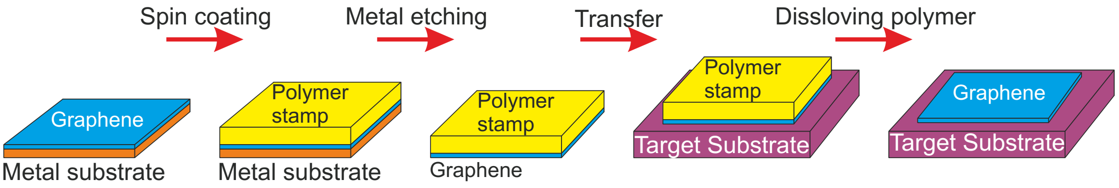

Figure 2.11: Illustration of the graphene transfer from a metal to the target substrate; adapted from [61].

While the graphene transfer is a rather straightforward process and can be utilized for various metal substrates, it might still impair the quality of the final graphene layer. A contamination of the graphene due to the wet chemical etching can occur. Additionally, wrinkles always appear on the transferred graphene, which might also influence the graphene performance negatively, depending on the chosen application.

A direct growth of graphene on the substrate required for applications or investigation would therefore be beneficial for the material quality. Additionally, as no transfer would be required, the utilization of graphene would be easier and more cost efficient, since one production stage could be saved. Therefore, presently much research is carried out on the deposition of graphene on other substrates such as semiconductor materials.

Besides the choice of substrate, numerous growth parameters influence the formation of graphene considerably, like for all CVD processes. In the following, a closer look will be taken at the influence of the growth temperature and growth time as well as of the precursor partial pressure and H_2 partial pressure.

The growth temperature determines, among other things, the proportional amount of precursor molecules which are thermally cracked. However, for the growth temperatures generally used for graphene growth no thermal, but rather catalytic decomposition of the C precursors at the hot substrate surfaces is expected. This decomposition, however, is also influenced by the given temperature. Additionally, the desorption of material from the sample and the diffusion on the surface is governed by the substrate's temperature. For rising growth temperatures an increasing decomposition rate but also a growing desorption rate will occur.

The deposition time as well as the cooling rate, if a precipitation process is applied, will influence the amount of C or graphene in the substrate and on the surface. This factor might not be quite as critical for the self limiting graphene growth on substrates with a low C solubility, but will tremendously affect the structures forming, when a substrate with high C solubility is used.

The partial pressure employed, on the other hand, will not influence the structure of the graphene for precipitation, as long as a sufficient growth time is chosen to reach a C supersaturation of the substrate during cool-down. For substrates with a low C solubility, though, using a high partial pressure for the C precursor might lead to a formation of graphene at numerous nucleation sites and therefore to polycrystalline graphene with small grain sizes [62].

Additionally, the hydrogen (H) partial pressure was found to be a crucial parameter in the graphene growth process. H has two roles in the C deposition, working in opposite directions [63]. Firstly, H enhances the catalytic decomposition of the C precursors. When no H is present during the growth process, the C precursor, e.g. methane, chemisorbs on the substrate's surface forming an active C species, such as CH_3, there. High energy barriers, though, have been found for this process making the dehydrogenation reactions thermodynamically unfavourable, for example, for graphene growth on Cu surfaces [64]. Molecular H, however, can form active H atoms on the substrate surface, which then promote the dehydrogenation of the C precursor. This reduces the formation of amorphous carbohydrate structures and enhances the growth of high-quality graphene layers. On the other hand H is also known to etch carbonic material, since also the reverse reaction of the dehydrogenation process takes place. C atoms from the edges of graphene domains are selectively etched off the surface and a fast growth of graphene is hindered. A careful adjustment of the H partial pressure is therefore necessary to enable a decomposition of the C precursor molecules and a growth of graphene.

2.2 The silicon surface

To put it simple, a semiconductor surface results from cleavage of a bulk crystal. Often this so-called ideal surface is energetically unfavourable due to reasons of charge neutrality and chemical bonding. As charge neutrality does not have to be taken into account for elementary semiconductors such as Si, chemical bonding is the fundamental reason for changes in the crystal structure at the surface of these.

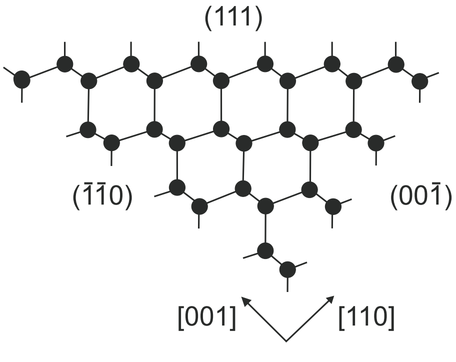

Figure 2.12: Simplified illustration of a diamond structure in [111] plane view direction, demonstrating the chemical bonds at different low index surfaces; adapted from [65].

Three possible low index surfaces for a diamond structure, showing the number of broken bonds for each surface, are displayed in fig. 2.12. Since elementary semiconductors like Si are built up by directional covalent bonds, containing two spin-paired electrons each, broken bonds lead to unstable free chemical valances containing only one unpaired electron known as a dangling bonds. To reduce the surface free energy the surface atoms relax from their bulk position to form new bonds, which is often associated with a significant distortion of the original crystal structure in the surface region. When compared to the bulk structure of semiconductors, this rearrangement of the surface atoms usually leads to a reduction in symmetry parallel to the surface. This rearrangement is called reconstruction. The Wood-notation describes the reconstructed surface mesh in terms of the ideal surface mesh:

$$\left(\frac{b_1}{a_1} \times \frac{b_2}{a_2}\right) R\alpha \tag{2.1}$$

with a_1 and a_2 being the basis vectors of the ideal surface mesh, b_1 and b_2 being the basis vectors of the reconstructed unit mesh and Rα describing the possible rotation. Centred or primitive unit cells are prefixed by a c and p respectively.

In the Si (001) surface each surface atom exhibits two dangling bonds, as shown in fig. 2.12.

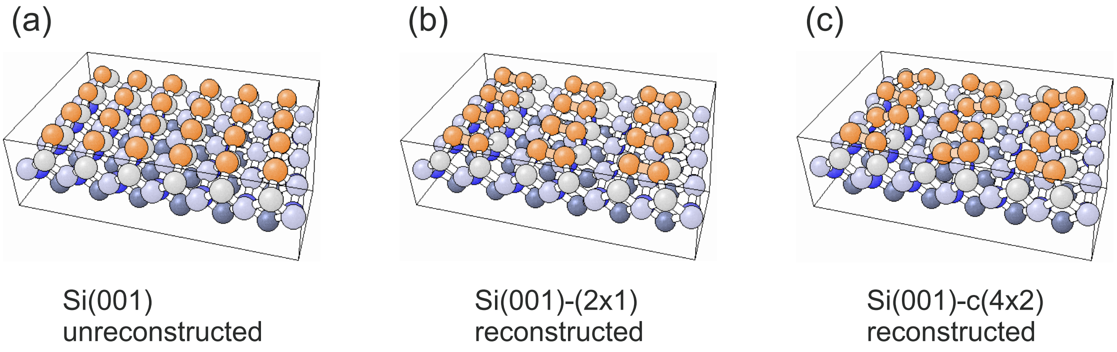

Figure 2.13: Visual representation of the reconstruction of a Si (001) surface; taken from [66].

The number of dangling bonds can be reduced by a factor of 2 when two neighboring Si atoms approach each other and form of a σ-like bond. These newly formed units, consisting of 2 Si atoms, are referred to as dimers. Long chains of dimers, known as dimer rows, form on the surface. Their orientation depends on their location in the Si crystal structure. This leads to the reconstructed Si (001)-(2x1) surface, which is schematically shown in fig. 2.13 (b).

After reconstruction, one dangling bond remains per surface atom in the Si (001)-(2x1) reconstruction. A π-type interaction occurs between the two residual dangling bonds of a dimer, leading to the formation of a binding π- and an antibinding π^*-band. Due to the small energy gap between π- and π^*-orbital, both bands overlap, creating a metallic surface for this symmetric dimer configuration. A reconstructed surface is energetically favourable since an asymmetric tilting or buckling of the dimers leads to an opening in the energy gap, as depicted in fig. 2.14.

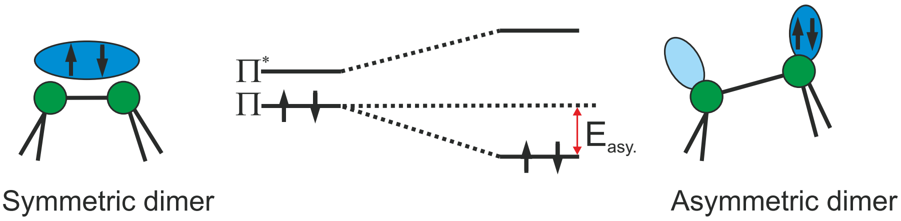

Figure 2.14: Schematic illustration of the orbital filling and energy structure of symmetric and asymmetric dimers at the Si (001) surface.

The electronic states D_{up}, originating from the upper atom, are lower in energy compared to the electronic states D_{down}, originating from the lower atom, and hence are filled preferentially. This buckling leads to the Si (001)-c(4x2) superstructure shown in fig. 2.13 (c), because the dimers are tilted in alternating directions along the dimer rows and a weak interaction occurs between neighboring dimer rows. The opening of the energy gap gives the Si surface its semiconducting character.

While the c(4x2) reconstructions exhibits the lowest surface free energy, its occurrence was heavily debated for a long time, since scanning tunnelling microscopy (STM) images taken at room temperature revealed only a symmetric dimer structure. Then it was discovered that the asymmetric dimer structure can be observed in experiments only at low temperatures (i.e., temperatures below 200 K) as a fast, thermally activated flipping between the two possible asymmetric dimer configurations occurs for higher temperatures, resulting in a seemingly symmetric dimer structure [67], [68], [69], [70].

So far, this study has only discussed the clean Si (001) surface. Due to their treatment in a H_2 atmosphere in the CVD reactor, it is reasonable to assume at least a partial H coverage of the Si surface for the samples in this study. However, it must be noted that the Si surface is inert towards molecular H_2 and can only react with atomic H. A H coverage of the Si surface in the CVD process can therefore only occur at high temperatures, at which at least a small part of the H_2 carrier gas is available as atomic H. Depending on the amount of H absorbed on the Si surface, different structures are possible, as depicted in fig. 2.15.

For high H doses the dimer structure of the Si surface can be broken. Each Si atom can then be saturated by two H atoms. This is the so-called dihydride phase, which is displayed in fig. 2.15 (a). A Si (001) surface can only exhibits a (1x1) reconstruction if solely the dihydride phase is present. For low H doses the dimer structure of Si remains preserved. H adsorbs in the so-called monohydride phase (fig. 2.15 (b)), i.e., each surface atom is saturated by one H atom. While the σ-like bonds stay intact for this phase, the interaction of the second dangling bond at each dimer is disrupted, preventing any buckling from

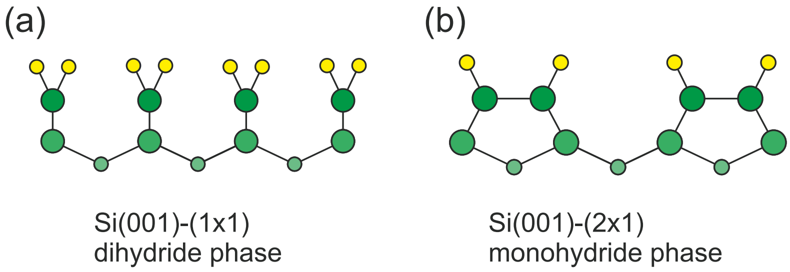

Figure 2.15: Illustration of two possible phases for H adsorption on Si (001) surface; adapted from [71].

occurring. Since the Si dimers remain, a purely monohydrided Si(001) surface possesses a (2x1) reconstruction. Also, a (3x1) reconstruction is possible as a result of a mixed phase, i.e., a mixture of dihydride and monohydride structures [72], [73].

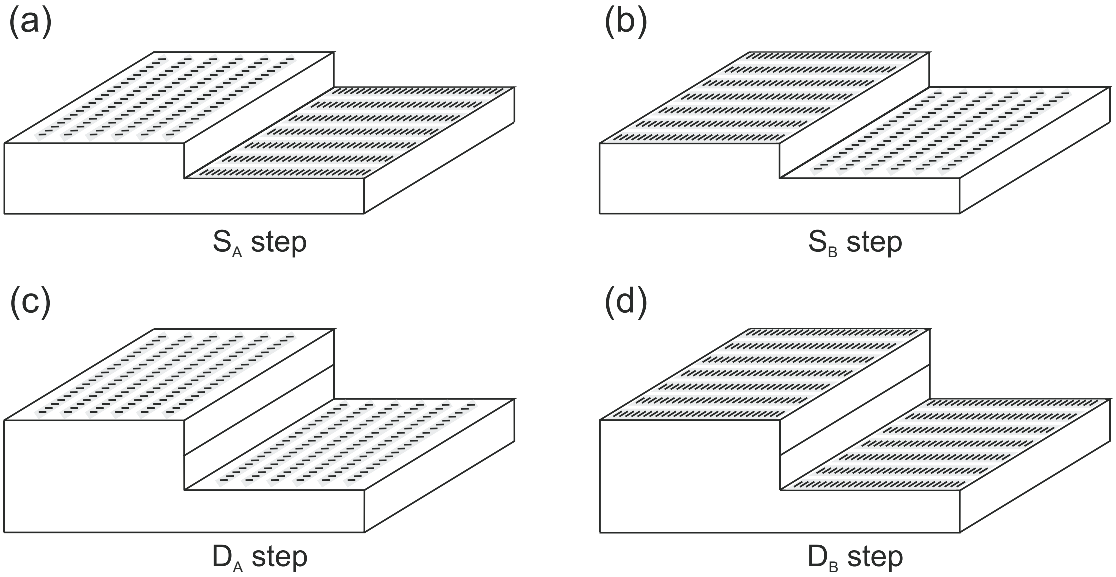

Figure 2.16: Illustration of possible step structures of a Si (001) surface.

Additionally, crystal surfaces are not smooth; rather the surface exhibits different domains separated by atomic steps. These steps are induced by the substrate's off-cut, which is the angle of the surface's misorientation from the specified lattice plane towards a different lattice plane. The spacing between successive steps, and thereby the size of the different domains, decreases with increasing off-cut. Due to the underlying diamond structure of Si, the dimer rows of domains separated from each other by any odd number of monoatomic steps are rotated by 90° towards each other. Two different domains arise on the Si surface with dimer rows either parallel to the step edges, which is then called type A, or perpendicular to the step edges, type B. Hence two types of monoatomic steps exist, as shown in fig. 2.16 (a) and (b), labelled S_A step where the upper-terrace dimer rows are parallel to the step edge or S_B step where the upper-terrace dimer rows are orientated perpendicular to the step edge. Depending on the off-cut as well as on the treatment of the surface, not only single-layer but also double-layer steps can occur. In the latter case, the direction of the dimer rows does not change at the step edge. Again two types of steps can be distinguished and are also shown in fig. 2.16 (c) and (d), labelled D_A step where the dimer rows on both terraces are parallel to the step edge or D_B step where the dimer rows are oriented perpendicular to the step edge on both terraces. Calculations for the clean Si (001) surface demonstrate, that the surface energy is lowest for S_A steps. But as these can only appear in combination with S_B steps, which hold considerably more energy, the overall surface energy is lowest for D_B steps. For a clean Si (001) surface D_A steps posses the highest surface free energy [74]. Double-layer type B steps were discovered in several studies of clean Si (001) surface. However, it was found that the step structure strongly depends on the substrate's misorientation. A clear structure exhibiting primarily double layer steps was mostly found at a misorientation of larger than 2° in [110]-direction. Otherwise, mostly single-layer steps will form [75]. It was found that for H covered surfaces, the formation energy for the different surface steps further depends on the hydrogen phase. It was calculated for a hydrogenated (2×1) phase, i.e., the monohydride phase, that for some structures the surface energy for the combined S_A and S_B steps is lower than that for D_B steps. The energy for D_A steps was again calculated to be the highest [76].

CHAPTER 3

Experimental methods

The experimental methods applied in this study will be introduced briefly in this chapter. All investigated samples were grown by chemical vapor deposition (CVD). The structure and functionality of a CVD system will be explained in section 3.1. The surface conditions of the grown samples were investigated with atomic force microscopy (AFM) (section 3.2) for all and with scanning electron microscopy (SEM) (section 3.4) and scanning tunnelling microscopy (STM) (section 3.6) for selected samples. Achieving atomic column resolution, scanning transmission electron microscopy (STEM) (section 3.3) was applied for chosen samples to gain a deeper insight into the atomic structure of the interfaces and, in combination with energy dispersive X-ray spectroscopy (EDX) (section 3.5), into the composition of the grown structures. For a further limited set of samples secondary ion mass spectrometry (SIMS) (section 3.8) was utilized to analyze the samples' composition. Finally, to detect ordered carbonic structures on the samples' surfaces, Raman spectroscopy (section 3.7) was applied.

3.1 Chemical vapor deposition

As mentioned, all samples shown in the following study were prepared by CVD. This method, a particular type of epitaxy, bears several advantages compared to other epitaxial methods such as liquid phase epitaxy (LPE) or molecular beam epitaxy (MBE). LPE exhibits the major drawback that no growth of abrupt interfaces or thin layers is feasible. While this is possible by MBE, this method requires UHV conditions making it expensive and susceptible to malfunctioning. Additionally, MBE is not practical for device production as the growth of homogeneous large-area structures is challenging.

3.1.1 Functionality of a chemical vapor deposition system

The sample growth in this work was performed using a commercial, horizontal CVD reactor system (*AIX 200-GFR*). A schematic drawing of this system is depicted in fig. 3.1. The

CVD setup can be divided into three parts: the gas-mixing cabinet, the growth reactor and the exhaust preparation.

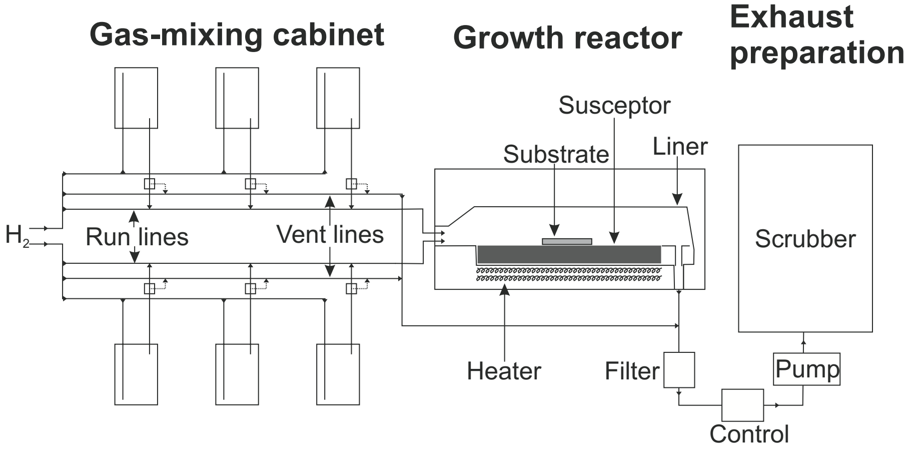

Figure 3.1: Sketch of the CVD machine.

Gas-mixing cabinet:

The gas-mixing cabinet combines the specific precursors necessary for the different source materials.

Apart from few exceptions, such as the gaseous Si precursor monosilane (SiH_4), the precursors are mostly liquids. They are stored in airtight stainless steel containers, the so-called bubblers; one of these is illustrated in fig. 3.2. The bubblers are kept in a water bath with accurate temperature adjustment to ensure a constant temperature of the precursor. A carrier gas, here palladium (Pd)-purified H_2, is injected into the bubbler through the source tube. The gas flow through the bubbler is precisely set by a source mass flow controller (MFC). After being saturated by the precursor, the carrier gas exits the bubbler and can be diluted by additional H_2 through the push tube. The gas is then transported to the reactor through a stainless steel pipe system. Group III- and group V-precursors are transported via separated pipes to avoid possible pre-reactions of these in the gas phase outside the reactor. The amount of each precursor in the reactor is given in terms of the partial pressure (P_P), which is calculated by the following equation:

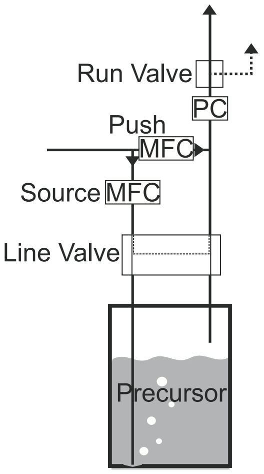

Figure 3.2: Schematic presentation of a bubbler.

$$P_P = \frac{Q_S}{Q_{\text{total}}} \cdot \frac{P_S}{P_C - P_S} \cdot P_R \tag{3.1}$$

Here Q_S is the flow through the bubbler, Q_{total} the total flow through the reactor, P_S the temperature dependent saturation vapor pressure of the precursor, P_C the pressure inside the bubbler, which can be adjusted by the downstream pressure controller (PC), and P_R the pressure inside the reactor, which is precisely controlled by a pumping system. To achieve a homogeneous gas supply throughout the entire growth process and to allow fast switching of the source materials, a run valve is attached to each bubbler. Thereby the precursor molecules can be transported into the reactor via the run line for deposition or into the exhaust via the vent line during growth interruptions. Apart from the precursor temperature all settings are computer controlled.

Growth reactor:

The CVD machine used here is equipped with a horizontal reactor, containing a specifically formed quartz cylinder, the so-called liner. The carrier gas, along with the precursor molecules, passes through the reactor in a laminar flow, which results from the form of the liner. For the deposition, the substrate is placed on a graphite block, the so-called susceptor inside the liner. A graphite plate is embedded in the susceptor and is rotated during the growth process by gas-foil-rotation (GFR) to obtain a homogeneous deposition. The susceptor's temperature, and, thus, the temperature of the substrate, can be adjusted by infrared halogen lamps outside the reactor. The temperature measurement is calibrated to the substrate's surface temperature by means of a Si/aluminium (Al) eutectic, which exhibits a phase transition at 577 °C. A linear correction factor is assumed.

Exhaust preparation:

After leaving the reactor, the carrier gas, including the undecomposed precursor molecules as well as any residuals, passes through a particle filter before reaching an exhaust gas cleaning equipment, the so-call scrubber. The partly toxic residual substances are bound here before the cleaned exhaust gas is released into the ambient air.

For some samples, GaP/Si (001) templates were used. These were prepared in a *12" Cruis cluster* equipped with a close coupled showerhead reactor. For this system mostly the reactor design differs from the introduced *AIX 200-GFR* system. However, as the template deposition was not investigated in this work, this design will not be discussed in detail. Further information on this particular growth process can be found in [77].

3.1.2 Chemical vapor deposition processes

As already mentioned, precursor molecules are used as source material for CVD. In this study SiH_4 was used as Si precursor, triethylgallium (TEGa) as well as trimethylgallium (TMGa) as gallium (Ga) precursor and tert-butylphosphine (TBP) as phosphorous (P) precursor. For C deposition tert-butylethylene (TBEthylene), tert-butylethyne (TBEthyne), benzene and ethylene were used. These precursors are sketched in fig. 3.3.

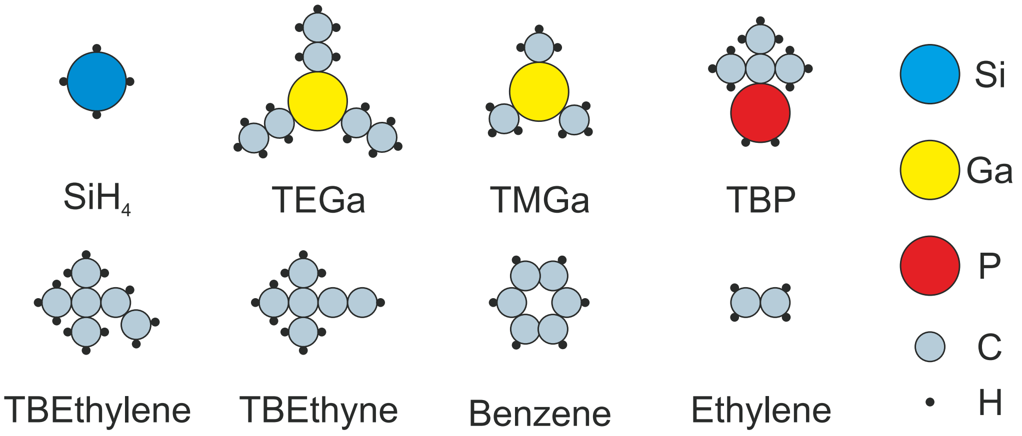

Figure 3.3: Schematic illustration of the precursors used for deposition in this study.

A simplified schematic description of the CVD process in the reactor is given in fig. 3.4. The precursor molecules are transported into the reactor by the carrier gas. Based on a concentration gradient in the reactor, a diffusion of the precursors towards the substrates occurs. A first cracking of the molecules can already happen in the gas phase due to molecules colliding. In an ideal case, the molecules completely decompose above the heated substrate's surface and the target atoms adsorb on the surface, while the hydrogen and organic residuals build stable molecules and are transported out of the reactor into the exhaust system by the carrier gas flow.

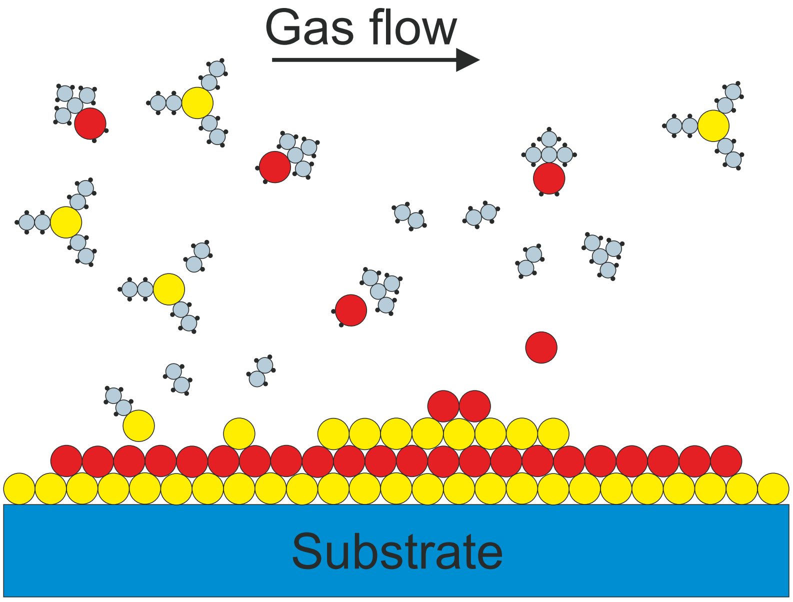

Figure 3.4: Simplified drawing of the processes occurring during CVD.

But, in reality the organic residuals are incorporated in the crystal to some extent, depending on the chosen growth conditions. For a sufficiently high temperature, atoms reaching the substrate diffuse on the surface until they are incorporated in the crystal or film or until they desorb from the surface and are transported into the exhaust system. As CVD is a non-equilibrium process, the partial pressure of the supplied atoms in the gas phase must be considerably higher than the equilibrium vapor pressure. Otherwise the desorption rate is higher than the adsorption rate, resulting in an etching rather than a growth process.

Most III-V-alloys, such as GaP, exhibit a so-called zinc blend crystal structure. Like the diamond cubic crystal structure, this structure consists of two face-centered cubic lattices, which are shifted by $\frac{1}{4}$ of the body diagonal of the unit cell. For III-V-crystals, however, each of these cubic lattices is build either by group III-atoms or by group V-atoms. The atoms are, thus, tetrahedrally coordinated and nearest neighbour atoms always belong to different groups. An equal amount of group III-atoms and of group V-atoms must therefore be available for the formation of a high-quality crystal structure. Based on the equilibrium vapor pressure of the group V-elements being significantly higher than that of the group III-elements, at high temperatures a so-called incongruent evaporation occurs. Unless a sufficient amount of group V-atoms is supplied, a metallic, group III-rich phase will eventually appear on the surface.

3.1.3 Sample pretreatment

Prior to the growth process, all substrates were treated by a wet-chemical etching procedure to remove any contamination, such as oxides or organic residues.

For Si substrates a procedure similar to the Shiraki process [78] is performed. Therefore, the Si substrates are first cleaned in concentrated sulphuric acid (96% H_2SO_4) to remove any organic residues from the surface. In the next step a heated etching solution of ammonium hydroxide (NH_4OH), ultra pure water (H_2O) and hydrogen peroxide (H_2O_2) is used to generate an oxide layer on the Si surface, binding remaining contaminations. The resulting Si dioxide along with the included contaminations is then removed by etching in dilute hydrofluoric acid (3% HF). Finally a protective, amorphous Si dioxide layer is applied using a heated solution of dilute hydrochloric acid (30% HCl), H_2O and H_2O_2. This defined layer can be removed by a high-temperature bake out in H_2 atmosphere in the reactor directly before the growth.

The pretreatment of the GaP substrates is also started by removing the organic residues using 96% H_2SO_4. This is followed by removing the topmost GaP layers along with the included impurities in dilute aqua regia, a mixture of 30% HCl, nitric acid (HNO_3) and H_2O.

For both etching procedures the substrates are thoroughly rinsed with ultra pure water between the individual etching steps and at the end of the procedure. After spin-drying the substrates under molecular nitrogen (N_2) flow, they are immediately introduced into the N_2 atmosphere of the CVD system.

3.2 Atomic force microscopy

AFM is a fast, non-destructive and comparatively simple method for the characterization of surfaces. No sample preparation is necessary for this method and it can be applied in ambient air. While due to the finite size of the probes used, the lateral resolution achieved is only in the region of several nanometers (nms), an atomic resolution can be reached in vertical direction. AFM utilizes the short distance van-der-Waals and electrostatic forces between a sample surface and a tip. Therefore, conductivity of the sample is not required for this method. All measurements in this study were carried out with a *Digital Instruments Nanoscope IIIa Scanning Probe Microscope*.

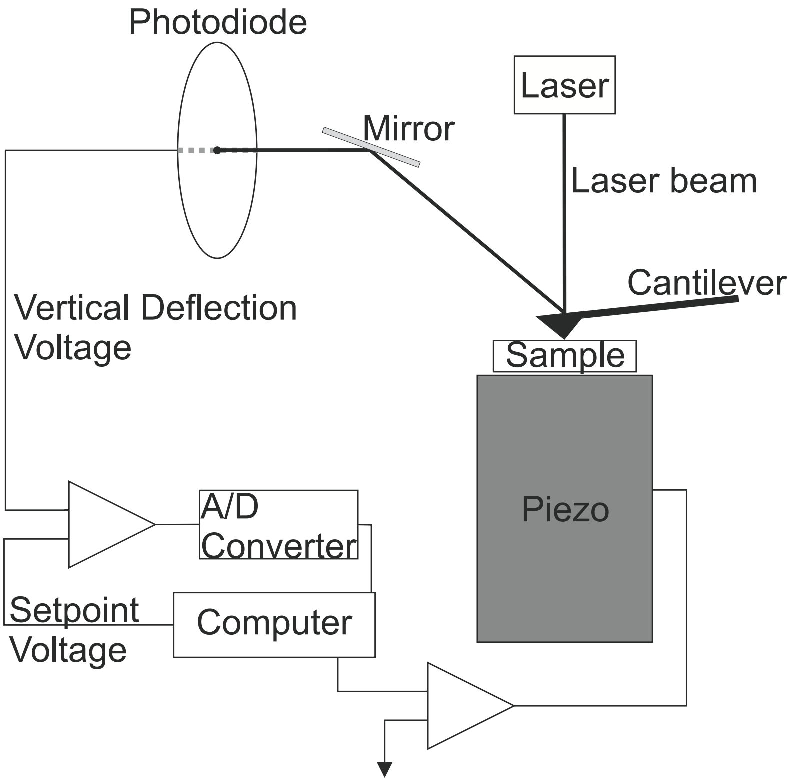

Figure 3.5: Principle of an atomic force microscope.

The set-up of an AFM is depicted in figure 3.5. The thin tip is fixed to a flexible and reflecting cantilever. Thereby it is deflected even by the small short distance forces, which depend strongly on the distance of the tip to the sample surface. To record the deflection of the tip, a laser beam is reflected at the back of the cantilever and then channelled onto a photo-diode array. The sample is mounted on a cylindrical arrangement of piezoelectric crystals. By this the sample can be moved in the three spatial directions allowing a linear scanning of the sample and an adjustment of the height to maintain a constant distance between sample and tip.

For the measurements in this study, the AFM was driven in tapping mode, a so-called non-contact mode. For this the AFM probe is stimulated to resonant oscillations by an additional piezoelectric crystal. A change in distance between tip and sample leads to a change in the amplitude of the oscillations. This is used as response for the distance, which can then be kept constant throughout the measurement by a feedback circuit through adjustment of the sample height. On the basis of this height modification of the sample, performed by the piezoelectric crystal, the surface morphology is mapped.

For some samples selective etching with 30% HCl was applied in combination with AFM measurements. HCl was chosen for this, as it removes metallic Ga with an etching rate of several nms per second, while it leaves a Si surface unaffected and exhibits a significantly lower etching rate on Ga containing crystalline material such as GaP. Therefore, selective etching with HCl primarily gives an indication whether a deposited structure consists of metallic Ga. Also, it provides a possibility of analysing the surface structure underneath the Ga structures following the deposition.

Statistical evaluations were performed for several sets of selected samples comparing values such as the size and number of deposited structures relative to the chosen growth conditions. The data used for these evaluations were determined by means of the AFM measurements using the software *Gwyddion*, a standard software for scanning probe microscopy data visualization and analysis. To analyze the deposited structures and differentiate these from the sample's surface a percentage threshold value was set. Areas exhibiting a height above this threshold value were defined as mounds and included in the statistical evaluation. As the structures occurring differ drastically for different growth conditions, the usage of a consistent threshold was not possible for all evaluations throughout this work. To achieve comparability a unified threshold was used for all data presented in an individual diagram. However, the thresholds chosen might differ for different diagrams. This might lead to minor differences in the absolute numbers given, even for identical samples, in different diagrams.

3.3 Scanning transmission electron microscopy

STEM is a special type of transmission electron microscopy (TEM) used to investigate materials with regard to such characteristics as composition or crystal quality, achieving an atomic column resolution. The technique relies on the interaction between an electron beam and an electron transparent specimen. In this study, high angle annular dark field (HAADF) STEM measurements were performed. A schematic presentation of the HAADF STEM set-up is displayed in fig. 3.6.

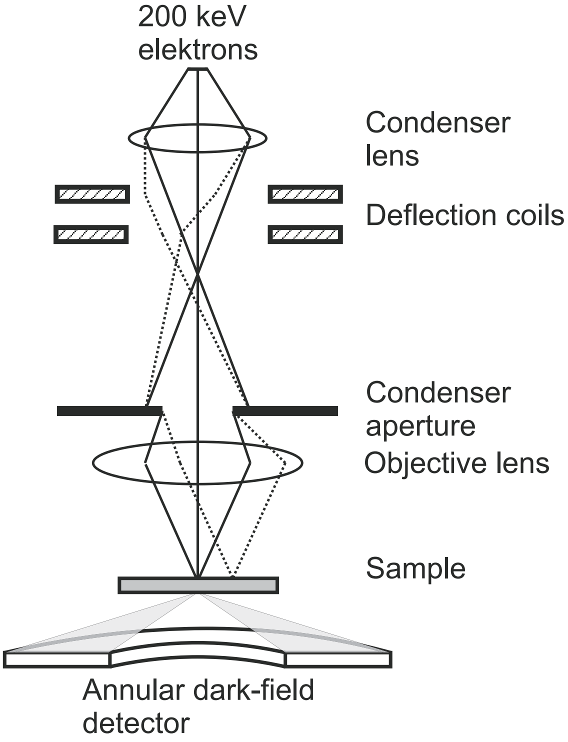

Figure 3.6: Illustration of the HAADF STEM principle.

A by various lenses highly focused electron beam is scanned across the sample by means of deflection coils. At each atomic column scattering occurs. An annular dark-field detector is used to collect scattered electrons after the transmission through the sample. The measured signal is then plotted against the beam position. The detector's distance to the sample is adjusted in such a way that only electrons with a high scattering angle are detected. While there are different types of scattering processes between the electrons and the atoms of the sample, HAADF STEM primarily detects electrons scattered by thermal diffuse scattering, an elastic incoherent scattering process. For high scattering angles the shielding effect of the electron shell of the atoms can be neglected, and electrons interact primarily with the unshielded atomic nucleus. As a result, the intensity of the detected signal is directly proportional to the sample thickness as well as to the atomic number Z of the atoms present in the respective atomic column. Hence, elements exhibiting a higher atomic number result in a brighter contrast in the HAADF STEM measurement. This technique therefore allows different elements to be distinguished directly.

For all measurements shown in the following a *JEOL JEM 2200FS*, equipped with a probe aberration-corrector and operating at an acceleration voltage of 200 kV, was used. To achieve electron transparency, samples have to be specially prepared prior to

the STEM investigation, making this method rather time consuming. All samples in this study were prepared in cross-sectional geometry, choosing the viewing direction along the $\langle 110 \rangle$ direction of Si, by conventional mechanical thinning and argon ion milling, using a *Gatan (model 691)* precision ion polishing system (PIPS). For exemplary samples, images recorded in [110] and in [$\bar{1}$10] viewing direction were compared and no anisotropy of the different directions was detected. For this reason the different viewing directions will not be distinguished in the following.
The TEM sample preparation in this study was performed by C. Becker; the STEM measurements were carried out by A. Beyer, K. I. Gries, A. Ott and R. Straubinger.

3.4 Scanning electron microscopy

Similar to STEM, the principle of the SEM is based on scanning a sample surface by means of a focussed electron beam in vacuum conditions. For SEM, though, the acceleration voltage used is in the range of 5-20 kV resulting in a comparably low penetration depth. After the interaction of the primary electrons (PEs) with the sample's atoms, various types of differently scattered electrons, as secondary electrons (SEs) or back scattered electrons, can be detected. SEs occur when the PEs deliver energy to the sample's atoms and consequently electrons of the outer shell of these atoms are released. While this scattering process occurs to some certain depth in the material, depending on the material's composition as well as on the acceleration voltage, only SEs, which were generated near the surface exhibit sufficient energy to leave the crystal. These electrons, in combination with the beam position, are used to generate SEM images displaying a sample's surface topography, as the amount of SEs being capable of leaving the sample depends on the angle at with the electron beam encounters the sample surface. A *JEOL JIB 4601F* was used for the measurements shown in this study, achieving a resolution in the nano meter range. No sample preparation is necessary for this technique.

3.5 Energy dispersive X-ray spectroscopy

EDX was performed for selected samples in combination with STEM or SEM, as this method also relies on the interaction of a (focussed) electron beam with the specimen being analyzed. For this technique the characteristic X-rays are detected, which occur as the electron beam is inelastically scattered at the sample. EDX allows an analysis of a sample's composition, as the energy of the characteristic X-rays emitted by atoms of different elements can be distinguished. As for STEM and SEM, the resolution achieved by EDX is dependent on the expansion of the electron beam. Additionally, the penetration depth of the PEs is determined by the acceleration voltage, which, as mentioned, can be chosen in a range between 5-20 kV for SEM. A low acceleration voltage results in a small penetration depth. The EDX measurement is then more surface sensitive than for a higher acceleration voltage. However, if the acceleration voltage is chosen too low, no characteristic X-rays can be generated. The surface sensitivity of this method is therefore limited.

3.6 Scanning tunnelling microscopy

3.6.1 Measurement principle

Similar to AFM, STM is a method for the characterization of solid-state surfaces.

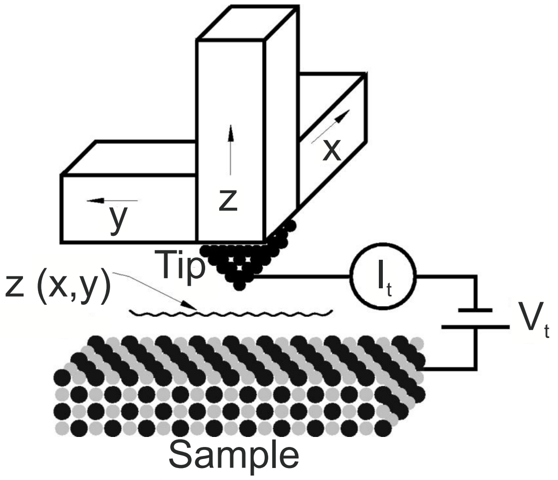

Figure 3.7: Schematic drawing of the STM set-up, adapted from [79].

Atomic resolution in the vertical as well as the lateral plane can be achieved for a sufficient quality of sample and tip. This technique, which is shown schematically in image 3.7, utilizes the tunnelling current occurring between an ideally monoatomic metallic tip, e.g. consisting of wolfram (W), and a conducting sample surface for an adequate small distance of a few angstrom when a voltage difference, a so-called bias, is applied; therefore, a conducting sample is required. The STM tip is mounted on a tripod arrangement of piezoelectric crystals; for the measurement the tip scans over the sample surface in xy-direction. At the same time the z-position of the tip, and by this the distance between sample surface and tip, is adjusted by the third piezoelectric crystal, called z-piezo. In the constant current mode, as used for the measurements in this study, this distance is continually adjusted throughout the scanning by a feedback circuit, obtaining a constant tunnelling current between tip and sample. In this mode, the voltage applied to the z-piezo is recorded as it is proportional to the distance between tip and surface.

The tunnelling current occurring between tip and sample depends exponentially on their distance, on the bias applied, as well as on the density of states of the surface. For a positive sample bias the lowest unoccupied surface states of the sample contribute mostly to the tunnelling current while for a negative sample bias this holds true for the highest occupied surface states. Therefore, not a pure height profile is obtained by plotting the tip's

distance to the surface against its xy-position, but a mixture of geometric and electronic information. This means that a careful interpretation is necessary.
An *OMICRON type VT SPM* was used for all measurements in this study.

3.6.2 Sample transfer

Achieving atomic resolution by STM is only possible for high quality sample surfaces. Any contamination, even oxygen (O) or H_2O, will be displayed in the measurement, concealing the surface structure to be investigated and might accumulate at the STM tip. Therefore, the STM measurement is performed in a UHV chamber with a base pressure in the region of 10^{-10} mbar. To avoid contamination of the UHV chamber, samples are introduced via a fast entry lock, which can be separated from the analysis chamber and pumped individually.
For the sample transfer from the CVD system to the STM chamber, a special vacuum transfer case and optimized working practices were developed as part of this research. A cylindrical case, containing a magnetic transfer rod, was equipped with two manual valves. These enable a connection to a pump system as well as to the STM UHV chamber or the glove-box of the CVD system. Also, a hermetic or vacuum sealing of the case is possible. A STM sample holder can be mounted on the transfer rod and thus be delivered between STM chamber and CVD system without contact to air. To reduce possible contaminations of the transfer system, the case is attached to the CVD system and pumped at least 12 hours in advance; a bake out is also performed during this pumping. In order to fit the STM sample holder, the substrate is cleaved into bars of roughly 2 x 10 mm^2 before growth. After the CVD process one of these bars is fixed onto the STM sample holder by leaf springs. This is done inside the N_2 filled glove-box and the sample inside the holder is then delivered into the transfer case, which is sealed off from the glove-box and pumped again directly after the transfer. By this procedure samples are transported from the growth reactor into a vacuum in the low 10^{-6} mbar region within approximately 3 minutes. After reaching the minimum pressure of about 2×10^{-7} mbar the case is removed from the pump system. After the transport and attachment of the transfer system to the STM chamber, this system is pumped again via the STM's entry lock before the final delivery of the sample into the STM UHV chamber.
STM measurement, as well as the development of the transfer chamber and the sample transfer process was performed in close collaboration with M. Reutzel and G. Mette in the work group of U. Höfer.

3.7 Raman spectroscopy

Raman spectroscopy is a comparatively fast and non-destructive technique to observe vibrational modes in a system. As described in section 2.1.2, it utilizes the inelastic scattering of monochromatic light due to the interaction of the light with the molecular vibrations in the irradiated sample. As these vibrational modes are characteristic and differ for different atomic bonds, it is used to identify the contained molecules, or rather chemical bonds. Stokes and anti-Stokes Raman scattering occur for all systems, i.e., a loss of energy for the scattered photons by exciting a lattice or molecule to a higher vibrational mode or a gain of energy for the photon as an initially excited molecule returns to the ground state. But as anti-Stokes Raman scattering requires an initial occupation of higher vibrational modes, it occurs less often than Stokes Raman scattering. For this reason, the energy spectrum is usually recorded in the region of an energy loss of the scattered photons, regarding only photons after Stokes Raman scattering.

An argon-ion laser was used as a source for monochromatic light for the measurements in this study, emitting light at a wavelength of 514 nm. Light emitted at other wavelengths, the so-call plasma lines, are removed from the laser beam by a set-up of filters and polarizers. Additionally, circular polarized light is generated by this, before the light is focussed on the sample, using an objective lens. After interaction with the sample, the scattered light is collected by the object lens again and passes a notch filter. This is necessary, as most photons are scattered elastically (Rayleigh scattering) without a change in energy. This component of the scattered photons, featuring a wavelength corresponding to the laser line, is suppressed as it might cause a damage of the detector but exhibits no information of the sample. The remaining light is focussed on a spectrometer, where it is spectrally separated before it is detected by a CCD camera.

All Raman measurements presented in this study were performed at the set-up of the work group of W. Heimbrodt.

3.8 Secondary ion mass spectrometry

The composition of a solid material system can be analyzed by SIMS. For this technique a sample is sputtered by a focused primary ion beam, e.g. O_2^+, cesium$^+$ (Cs^+) or Ga^+. The choice of the primary ion beam used depends on the elements sought to be detected. Atoms from the sample get ejected and ionized due to the ion bombardment. These so-called secondary ions are then collected and analyzed by means of a mass spectrometer. The sputtering leads to a slow local ablation of the sample, which allows to produce a depth profile of the composition.

All measurements shown in this study were performed by the RTG Mikroanalyse GmbH. As a significant SIMS analysis of a sample's surface is not possible, due to unavoidable contaminations, samples were grown in a special manner for this technique, utilizing a cap of well-defined composition to cover the layer sought to be investigated.

CHAPTER 4

Results and discussion

The following chapter presents an overview of the most important results obtained during this study. The ultimate aim of this investigation was the direct growth of graphene on Si (001) by CVD. A thorough analysis and understanding of the growth surfaces employed is necessary in order to achieve this goal. Therefore, the results gained by these investigations are introduced at the beginning of this chapter. The first part, section 4.1, discusses the characterization of the Si (001) surface after CVD preparation, as seen with STM. As mentioned before, the catalytic effect of metallic Ga should be utilized for the growth of ordered C structures, initially requiring the controlled deposition of metallic Ga droplets. Hence this deposition was studied for two Ga precursors, TEGa and TMGa, and will be presented in section 4.2. Since it was not found possible to establish metallic Ga on Si (001) by CVD and a GaP layer on Si (001) might therefore be considered a suitable growth surface for Ga and graphene deposition, the surface preparation of GaP (001) (section 4.3), the deposition of GaP on Si (001) (section 4.4), and the deposition of Ga on GaP (section 4.5) were also investigated and will be discussed in the following. The last section of this chapter, section 4.6, will then review the results obtained for C deposition using the different C precursors (benzene, TBEthylene, TBEthyne and ethylene), various growth parameters and differently pretreated substrates.

4.1 Silicon (001) surface preparation

As the Si (001) surface serves as substrate for the deposition in the following, first a thorough investigation of this surface was performed. In previous works the surface preparation of Si (001) was already investigated and optimized for growth of GaP on Si [80],[81],[82]. The growth conditions developed in these references were also applied here, but the actual atomic structure of the surface after the high-temperature treatment in H_2 and subsequent cooling in H_2 ambient, which is considered as crucial step in this preparation, has not been explicitly shown yet.

For the samples shown in this section 4” Si (001) substrates with an intentional 0.1°

misorientation in [110]-direction were used. After a wet chemical etching, as described in section 3.1.3, a high-temperature bake out at 975 °C in H_2 atmosphere was performed for 15 min to remove remaining O from the surface. To further improve the surface, SiH_4 was then supplied at 925 °C for 10 min prior to growth at a low partial pressure of the Si precursor, which is assumed to lead to an etching of the surface rather than to the growth of a Si layer. Finally an approximately 1 µm thick Si buffer was deposited again at 925 °C by supplying SiH_4 at a higher partial pressure. The buffer growth was followed by a high-temperature annealing for 10 min at 975 °C. This annealing was performed in a H_2 atmosphere at a reactor pressure of 950 mbar. It was shown in [80],[81],[82] that this annealing at a high reactor pressure is especially important for the formation of double steps on the Si surface, which are essential for the growth of high-quality GaP on Si (001) as otherwise anti-phase boundaries (APBs) form in the GaP at monoatomic steps.

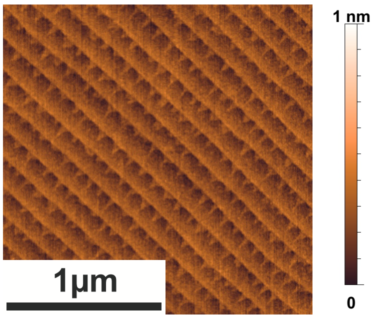

Figure 4.1: AFM image of a Si buffer grown on a Si (001) substrate with an intentional 0.1° off-cut in [110]-direction after a high-temperature annealing.

An AFM image of a Si sample after the described treatment is shown in fig. 4.1. The scanning was performed under a scanning angle of 45° with respect to <110> direction. The measurement reveals primarily large terraces on the surface with step edges perpendicular to the direction of the off-cut, i.e., with step edges in $[1\bar{1}0]$ direction. Additionally, small triangular terraces protrude along these step edges.

Different surface reconstructions are possible for the Si surface, depending on the sample treatment, as described in section 2.2. Due to the limited resolution of this technique, the atomic structure of the surface can not be detected by AFM. Therefore, STM measurements were performed for this sample. The Si sample was transferred from the CVD system to the STM set-up as described in section 3.6. A lower magnification STM image is presented in fig. 4.2 (a). It exhibits the surface structure already found by AFM measurement additionally showing that the majority of the small terraces stretches across almost the whole length of the larger terraces. Utilizing a higher magnification, Si dimer rows are resolved in image 4.2 (b). As sketched in image (c), these run parallel to the step edges on the larger terraces in the upper and lower part of the image, indicating these extended steps in $[1\bar{1}0]$ direction as D_A steps. On the small terraces the dimer rows run perpendicular to the step edges revealing these steps as remains of S_B steps.

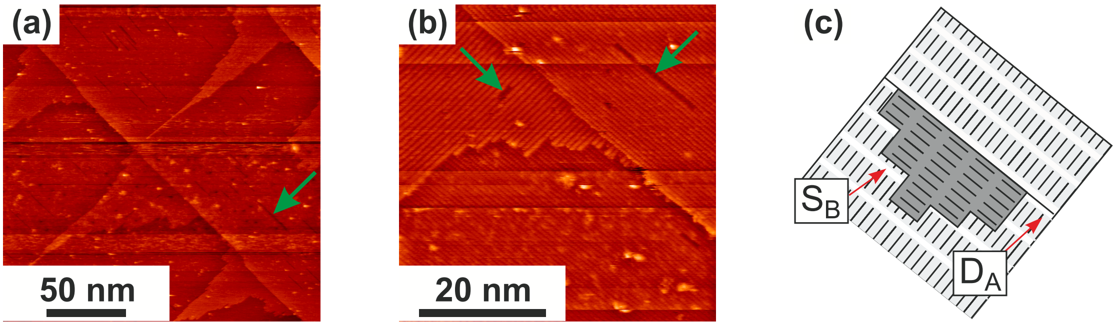

Figure 4.2: STM images of a Si buffer as shown in fig. 4.1, measured with two different magnifications (a) (bias voltage: -2.25 V; tunnelling current: 0.5 nA) and (b) (bias voltage: -2.18 V; tunnelling current: 0.5 nA). A scheme of the surface structure is displayed in (c).

Similar structures were observed by others [83], [84] for Si surfaces prepared in a similar way. However, this result is clearly different from most previous findings. As described in section 2.2, for a clean Si (001) surface D_A as well as S_B steps hold a considerably increased surface free energy in comparison to D_B or S_A steps. Resulting from this, D_A steps do not appear on a clean Si (001) surface without an elaborate treatment as ion bombardment [85]. For this sample no clean Si surface, but rather at least a partial H coverage is assumed, since the sample treatment was performed at high temperatures in a H atmosphere; the intact dimer structure indicates that mostly the monohydride phase is present. As mentioned before, the calculations for the clean Si (001) surface are not applicable for a H coverage. But here again D_A steps exhibit the highest surface free energy and no stable D_A steps were found for experiments in UHV. Their appearance must result from the specific sample preparation used here and in [83], [84]. As mentioned previously, the high-temperature treatment of the buffer in H_2 performed at a high rector pressure is essential for the formation of the double steps, which were not detected without an annealing or for an annealing at a considerably lower reactor pressure [81]. Presumably, the specific structure found here results from an etching process taking place during or after the annealing. An occurrence of vacancies and a tendency for these vacancies not to appear statistically distributed, but to accumulate and form rows along the dimer rows is clearly revealed in both measurements in image 4.2. Some vacancy rows are highlighted exemplarily by green arrows. Whether these form due to a preferential generation of vacancies in the surrounding of already existing vacancies or by diffusion of vacancies can not be determined by this measurement. A model explaining the specific structure dominated by D_A steps by generation, diffusion, and annihilation of vacancies on the initially existing S_B steps is proposed in [83]. The characteristics of the vacancy formation become especially obvious in fig. 4.3 displaying a Si (001) surface prepared as described before, which reveals another noteworthy feature, shortly mentioned in connection with fig. 4.2 (a).

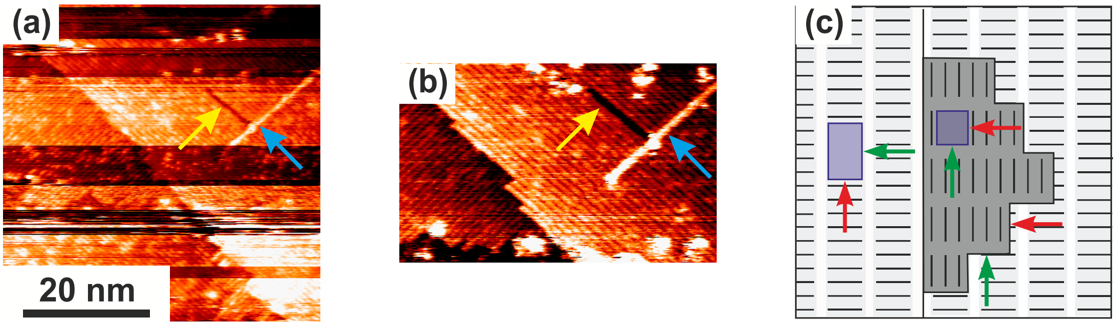

Figure 4.3: STM images of a Si surface showing a Si needle structure (marked by a cyan arrow) and a vacancy row (highlighted by a yellow arrow) with two different magnifications (a) and (b) (bias voltage: -1.93 V; tunnelling current: 0.3 nA; for both). Illustration of the surface structure, showing a D_A and S_B step with vacancy rows (displayed in blue) (c). The A and B type of step edges are exemplarily highlighted by green or red arrows.

Images (a) and (b) reveal a single dimer row wide needle structure, which is nearly extended across the whole terrace, emphasized by a cyan arrow. This needle is particularly obvious in fig. 4.3 (b), which displays a better resolved section of an image recorded successively after figure (a), using the same settings. Like the dominance of D_A steps, this particular structure is probably generated by the etching process occurring due to the high-temperature treatment at a high reactor pressure. The elongated gaps in the dimer rows found in all images, for example, also in fig. 4.3 next to the needle structure (highlighted by the yellow arrow), indicate that a successive generation of vacancies or a diffusion and coalesce of these along the dimer rows is favored compared to a statistical distribution or a coalescence perpendicular to these rows. Image 4.3 (c) presents a scheme of the Si (001) surface as observed by STM, showing a D_A and S_B step as well as vacancy rows (highlighted in blue) on both type of terraces. An anisotropy for the annihilation of surface vacancies becomes obvious, i.e., a preferential vacancy annihilation at the S_B step edges (red arrows) compared to the S_A step edges (green arrows). This results in a selective depletion of the type B steps and a remaining of primarily D_A steps, as well as in the generation of the vacancy rows along the dimer rows. Certain coincidental dimer rows are not etched off during the annealing while the surrounding Si desorbs, as only dimer rows, but not neighbouring dimers, are preferentially etched. This leads to the needle structures observed.

This anisotropy between S_B and S_A steps might be explainable by the difference in their bond coordination [74], [86]. Since S_A step edges occur between two neighbouring dimer rows and no nearest-neighbour bonds are broken, atoms at the edge still have a fourfold coordination. S_B step edges, though, run between two dimers, which means that one nearest-neighbour bond per edge atom is broken, and dangling bonds occur. To gain a fourfold coordination, edge atoms can form dimers with neighbouring atoms resulting in a so-called rebonded step edge. However, the dimer structure, and with this also the electronic structure at S_B steps significantly differs from the bond structure of the reconstructed Si (001) surface. This might lead to the less stable configuration observed at the S_B step edges.

It has to be assumed that the pure D_A step structure is thermodynamically unstable. However, cooling down presumably leads to a formation of a stable phase, possibly a monohydride phase, and a reduction of the Si adatome diffusion rate. This leads to a passivation of the Si surface [83].

4.2 Gallium deposition on silicon

As mentioned previously, it is assumed that due to the high solubility of C in Si, a direct growth of graphene on Si is not possible [87], [88]. It was shown before that Ga is usable as a catalyst for the growth of low-dimensional C structures such as graphene or C nanotubes [9], [89]. This catalytic growth might be applicable on Si as well, but the controllability of the Ga deposition is an important factor in making use of this effect. The deposition of the standard Ga precursors TEGa and TMGa was investigated as well as the behaviour of the deposited structures after a treatment with temperatures between 500 °C and 800 °C following the deposition, which might be necessary for further growth. The results presented in this section were published in part in [90].

4.2.1 Triethylgallium deposition

The growth parameters for the deposition of Ga on Si (001) using TEGa as a Ga precursor molecule were initially adapted from the GaP nucleation on Si (001) [81].

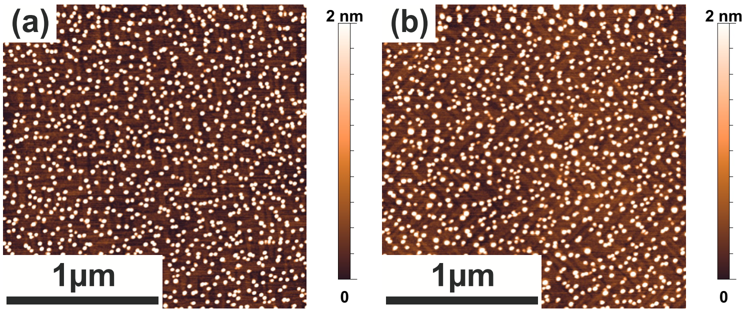

Figure 4.4: AFM images of a Si (001) surface after 15 s of TEGa deposition at 450 °C as-grown (a) and after etching in 30% HCl (b).

An AFM measurement of a Si (001) surface after the deposition of Ga on Si for 15 s at a temperature of 450 °C and a TEGa partial pressure of 7.6×10^{-4} mbar is displayed in fig. 4.4 (a). The amount of TEGa supplied corresponds to approximately 2.1 MLs of

Ga, judging from the results on the growth of GaP on Si (001) under equivalent growth conditions. The AFM micrograph reveals that mounds form on the Si surface due to the deposition of TEGa. For a further investigation of the surface, the sample was etched in 30% HCl, since metallic Ga can be removed by 30% HCl with an etching rate of several nms per second, as described in section 3.2. The same sample after etching for 30 s in 30% HCl is presented in fig. 4.4 (b). The structures observed in (a), though, can only be affected marginally in size and height by etching in HCl. This behaviour provides evidence that the structures forming can not only consist of metallic Ga. To get a better knowledge of the structure of the aggregates found by AFM, HAADF STEM measurements were performed.

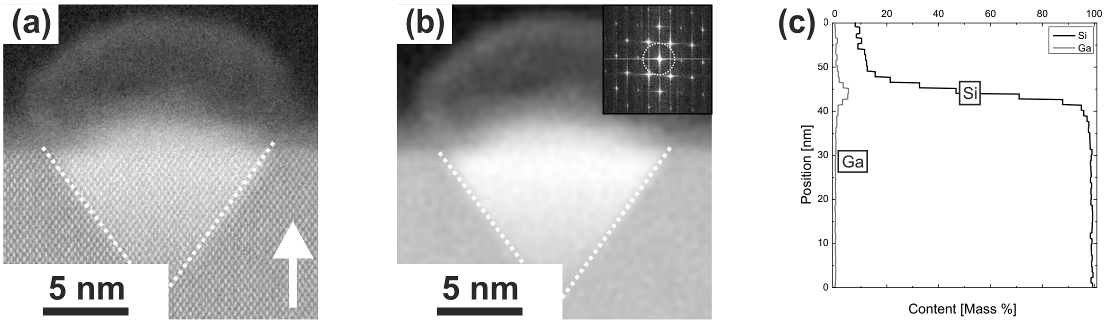

Figure 4.5: Cross-sectional HAADF STEM image (a) and low pass filtered image (b) in $\langle 110 \rangle$ viewing direction of a Si sample after TEGa deposition, using the same growth conditions as for the sample already shown in the AFM measurement in fig. 4.4. EDX line profiles of Si and Ga acquired along the growth direction (c) at a structure as shown in (a).

The STEM image 4.5 (a) reveals a bright pyramidal structure in the Si with an amorphous cap. The white arrow represents the growth direction. The boundaries of this structure within the Si, which are marked by the dashed white lines for better visibility, are on the Si $\{111\}$ lattice planes. This can be explained by the greater stability of the Si $\{111\}$ planes in comparison with other Si planes [91]. The position of the dashed white line was determined using the low pass filtered image 4.5 (b), as here the contrast of the pyramid against Si becomes more pronounced. The inset shows the corresponding Fourier transformation and the size of the mask used for filtering. The EDX line profiles for Si and Ga, which were acquired along the growth direction at a similar structure, are shown in 4.5 (c). These indicate that the pyramid contains Ga and, thus, results from Ga diffusing into Si during the deposition. While a crystalline structure is clearly visible in the bright pyramidal structure (fig. 4.5 (a)), it is not assumed that a mixed crystalline lattice of Si and Ga forms. Rather, the crystal structure arises from the fraction of intact Si lattice positioned behind and in front of the Ga, which forms a pyramidal structure, with respect to the electron beam direction. This Si is observed, since the TEM sample has a finite thickness considerably larger than that of the structure containing Ga. This assumption is also supported by the better visibility in the low pass filtered image (fig. 4.5 (b)), since the bright contrast in the pyramidal structure primarily originates from the regions between, rather than on, the atom columns.

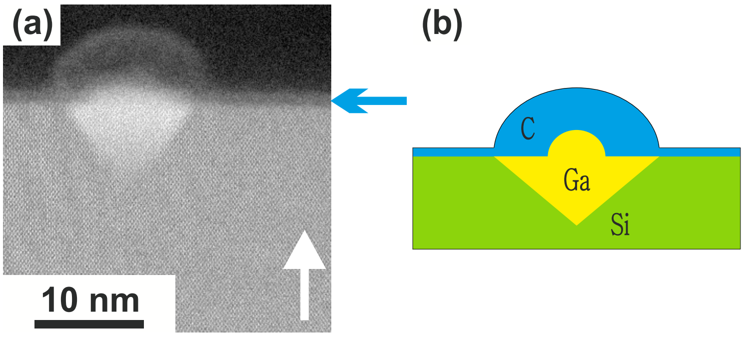

Figure 4.6: Cross-sectional HAADF STEM image of a Si (001) sample after TEGa deposition as shown in 4.4, but utilizing a smaller magnification (a), and a schematic illustration of the arisen aggregate (b).

A larger section of a HAADF STEM image of the same sample, which is displayed in fig. 4.6, reveals that an amorphous layer (highlighted by a cyan arrow) stretches across the whole sample surface. The layer is clearly pronounced above the Ga-containing structure. Since the mounds on the surface are removable by organic solvents, like isopropanol, one can assume that this layer contains C, which results from the formation and deposition of polyethylene chains by the residual organic groups in the TEGa precursor molecule. This is consistent with the assumption of Ga having a catalytic effect on the deposition on C, as the thickness of the layer containing C is considerably enhanced above the structure containing Ga. But no indication of ordered C structures was found, for example, by means of Raman spectroscopy.

Influence of triethylgallium deposition time and partial pressure

In order to better comprehend and control the deposition, the influence of different growth parameters on the structures containing Ga was also investigated.
Firstly, the growth time is one parameter which might be used to adjust the deposited structures to the desired profile. Therefore, samples were prepared with different growth times while all other parameters were kept constant. AFM measurements of these samples are displayed in fig. 4.7.

As for all samples shown previously in this section, the growth temperature for the Ga deposition was set to 450 °C and the TEGa partial pressure to 7.6×10^{-4} mbar. With this setting, the amount of Ga deposited corresponds to approximately 0.14 MLs for a deposition time of 1 s and to 2.1 MLs for a deposition time of 15 s. The measurements reveal that for all growth times used, even for a deposition of only 0.14 MLs of Ga, mounds form on the Si surface. An evaluation of the influence of the growth time on the deposited structures, i.e., of the time's influence on the size and number of structures formed, is given

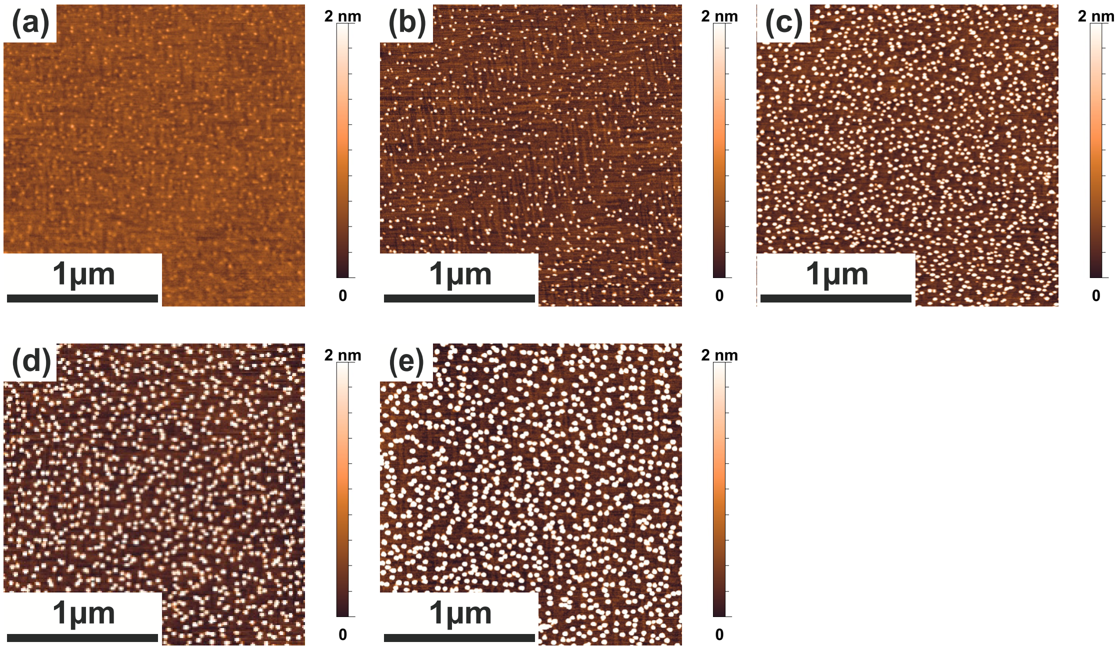

Figure 4.7: AFM micrograph of Si (001) substrates after TEGa deposition at 450 °C for different times. For all samples a TEGa partial pressure of 7.6×10^{-4} mbar was used. The TEGa deposition time was increased from 1 s (a) to 3 s (b), 5 s (c), 10 s (d) and 15 s (e).

in fig. 4.8. This evaluation was performed utilizing the software *Gwyddion* as described in section 3.2, using AFM images with a dimension of $2 \times 2\ \mu m^2$. This is the dimension of all AFM images displayed in this study.

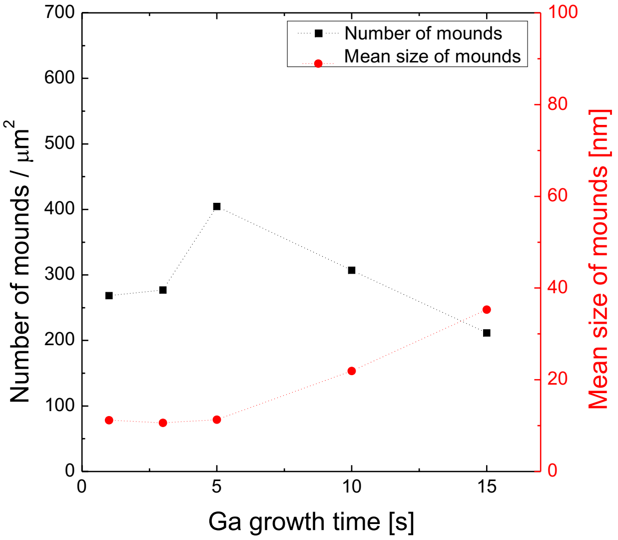

Figure 4.8: Correlation between deposition time and the size and number of deposited structures respectively in the samples shown in fig. 4.7.

As in all diagrams presented in this research, the lines displayed are merely guides to illustrate a rough trend rather than a function fitted to the data points. The mean size of the mounds, displayed as red data points, remains constant for the first three samples and then increases with rising deposition times. The number of mounds, presented by the black data points, grows at the beginning and then drastically decreases again with increasing deposition time. The formation of Ga islands is energetically favorable compared to the formation of a Ga film covering the surface [92]. But the material deposited on the surface for TEGa growth on Si (001) is significantly hindered in its mobility, as will become clear later. Due to the short growth time at which a sufficient temperature for diffusion on the surface is maintained, only small structures can form. As the structures do not merge when given short growth times, a rise in deposition time initially results in an increase in the number of structures arising, but does not significantly change their size. A further increase in growth time eventually results in a merging of the structures. This leads to a continuous decrease in the number of structures and a concurrent growth of their size with increasing growth time.
The change in the deposited structures due to a variation in time with a constant Ga partial pressure of 7.6×10^{-4} mbar, was compared to the difference in deposition due to a change in the Ga partial pressure using a constant deposition time of 1 s. AFM images of samples prepared with varying growth times and with different Ga partial pressures are presented in fig. 4.9. An evaluation of the number as well as mean size of aggregates forming for the different parameters is given in fig. 4.10.

For all samples shown in fig. 4.9 the TEGa growth temperature was set to 450 °C. Image (a) presents a sample after a Ga deposition of 1 s with a partial pressure of 7.6×10^{-4} mbar, corresponding to a deposition of approximately 0.14 MLs of Ga. This sample was chosen as a starting point for the variation of the growth time in (b) and (c) as well as the Ga partial pressure in (d) and (e). For the samples displayed in (b) and (c) the Ga growth time was increased to 5 s and 10 s respectively, as already shown in fig. 4.7 (c) and (d). Images (d) and (e) present samples for which the Ga partial pressure was increased to 3.8×10^{-3} mbar and 7.6×10^{-3} mbar respectively, corresponding to a deposition of approximately 0.7 MLs or 1.4 MLs of Ga per second, judging by the GaP deposition under these conditions. For all conditions applied here, aggregates containing Ga formed on the Si (001) surface. However, the measurements reveal a clear difference in the dependency of the structure's properties on the growth time and on the partial pressure, which becomes especially obvious in the evaluation depicted in fig. 4.10.

It was already found in fig. 4.8 that for an increasing growth time the size of the structures increases only slightly for short times and then increases considerably for longer times. Concurrently, the number of aggregates initially increases and then drastically decreases for longer growth times. As already mentioned, this is presumably due to

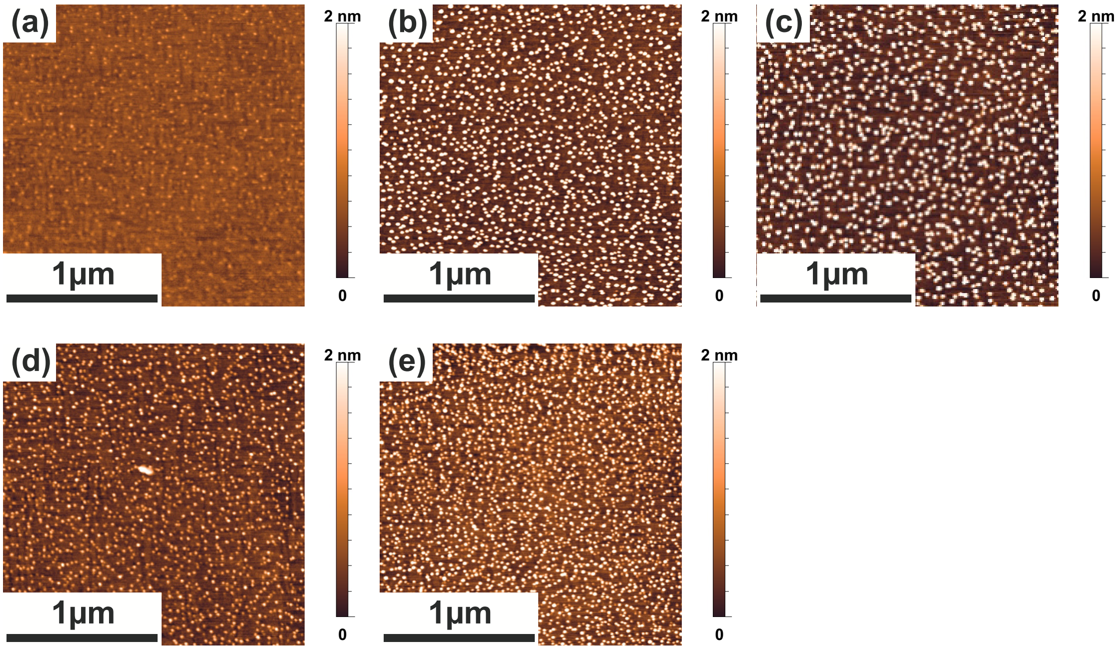

Figure 4.9: AFM images of Si (001) samples after TEGa deposition at 450 °C; starting from a growth time of 1 s in a (a) the deposition time was increased to 5 s in (b) and 10 s in (c) while the TEGa partial pressure was kept constant at $7.6{\times}10^{-4}$ mbar. For the lower samples the TEGa partial pressure was increased to $3.8{\times}10^{-3}$ mbar (d) and 7.6×10^{-3} mbar (e) respectively while keeping the deposition time constant at 1 s. A detailed evaluation of the presented samples is depicted fig 4.10.

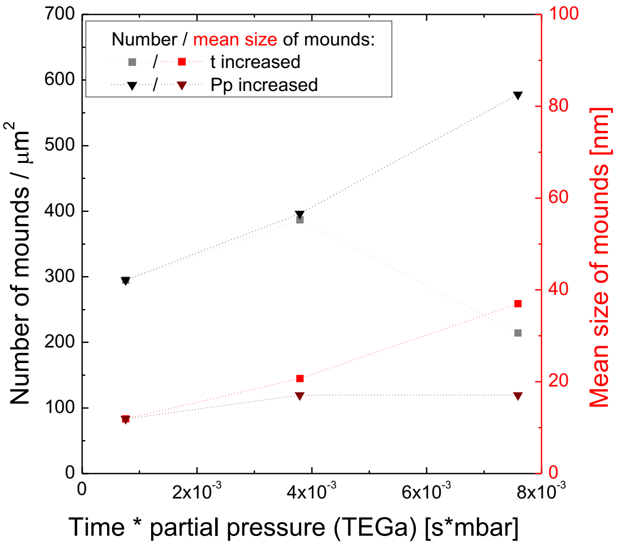

Figure 4.10: Evaluation of the correlations between growth time and partial pressure respectively with the number of mounds and their size using the samples shown in fig. 4.9.

a merging of the Ga structures which can only occur at a high temperature, such as the growth temperature of 450 °C, and during longer growth times. With an increase in the Ga partial pressure, the size of the structures forming increases slightly at first and then remains constant while the amount of aggregates rises continuously. This is in accordance with the hypothesis stated that the merging of the aggregates does not start immediately, but only for a sufficiently long growth time. A further increase in the Ga growth time will therefore lead to an enhanced merging of the structures and with this an increase in the structures' size while an additional increase in Ga partial pressure will presumably lead to an increase in the number of structures forming. This is assumed at least until the surface coverage reaches such an extent that merging becomes inevitable. Based on these two contrary growth processes it can be expected that an accurate tailoring of the structures is possible by meticulously adjusting partial pressure and growth time.

In addition to the feasibility of modifying the structures' properties, an adjustment in the Ga partial pressure, rather than the Ga growth time, might lead to a reduced diffusion of Ga into the Si surface. This might improve the quality of the eventually grown interfaces as a diffusion of the Ga presumably leads to a roughening of the Si (001) surface. Also, it might have a positive effect on the intended catalytic growth of the C structures, as the diffusion could reduce the amount of metallic Ga at the surface. Assuming a decreased Ga diffusion for a shorter growth time is based on the requirement of a sufficient temperature for the diffusion. To verify this assumption, HAADF STEM measurements of two samples exhibiting a similar amount of material on the surface but deposited with different growth times and partial pressures are shown in fig. 4.11.

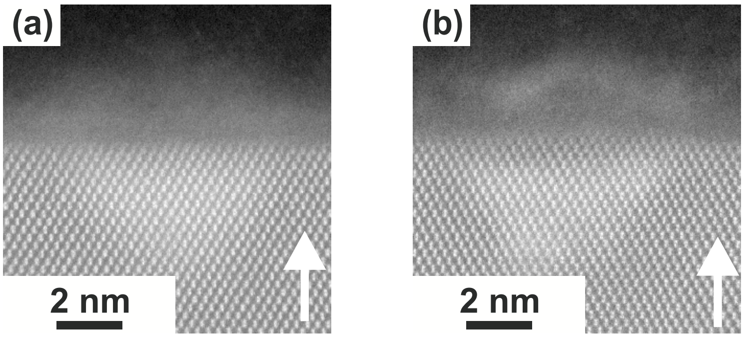

Figure 4.11: Cross-sectional HAADF STEM images of Si (001) after TEGa deposition at 450 °C applying a long growth time of 15 s, but a low Ga partial pressure of 7.6×10^{-4} mbar (a) or a growth time of only 1 s, but a Ga partial pressure that was increased by a factor of 10 to 7.6×10^{-3} mbar (b).

A Si sample after 15 s of TEGa deposition at 450 °C using a Ga partial pressure of 7.6×10^{-4} mbar is displayed in fig. 4.11 (a) . For the sample shown in (b) the Ga growth time was decreased to 1 s while the Ga partial pressure was increased by a factor of 10 to 7.6×10^{-3} mbar, resulting in a similar amount of aggregates containing Ga on the surface. The measurement reveals bright pyramidal structures in the Si in both samples, which originate from Ga diffused into Si, as already seen in fig. 4.5. The surface of each sample is also covered by an amorphous layer, which is clearly pronounced above the Ga-containing structure. No clear difference in the properties of the structures was caused by the change in deposition parameters. This result indicates that the diffusion of the Ga into the Si proceeds considerably fast. Only the integral amount of Ga deposited is decisive for this diffusion, changes in the growth time have no influence on it.

No reduction of the diffusion is expected by a modification of the Ga growth time or partial pressure. Another approach to reducing the Ga diffusion is by decreasing the Ga growth temperature. This approach was also investigated. A reduced growth temperature, however, involves the problem of a decreasing decomposition rate of the Ga precursor with decreasing temperature in this range.

Temperature dependency

AFM measurements for samples grown at different temperatures using otherwise equal growth conditions are shown in fig. 4.12 (a) and (b) as well as (c) and (d).

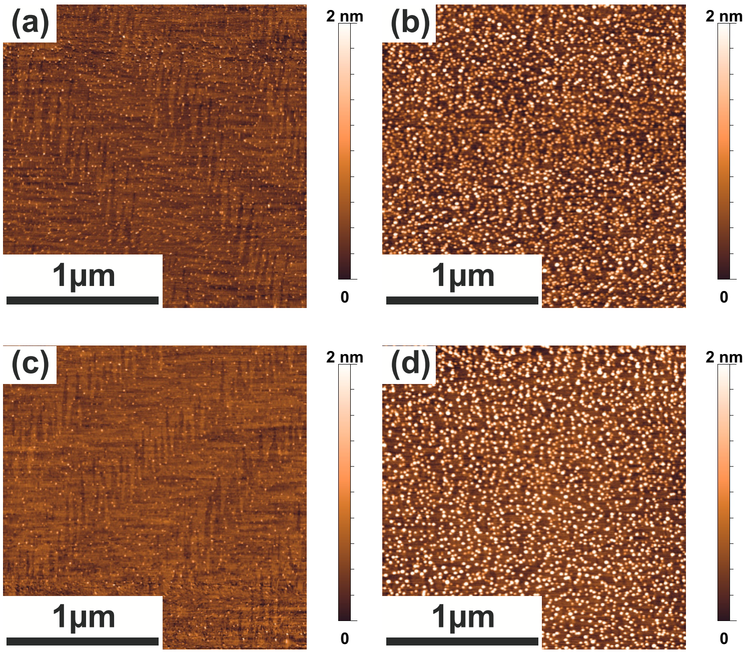

Figure 4.12: AFM micrographs of samples after TEGa deposition at different temperatures. For all samples a growth time of 1 s was used. A growth temperature of 375 °C and a TEGa partial pressure of 1.5×10^{-2} mbar was chosen for (a). The same TEGa partial pressure, but an increased growth temperature of 400 °C was applied for (b). Again a low growth temperature of 375 °C but a decreased TEGa partial pressure of 7.6×10^{-3} mbar was used for (c). An increased temperature but the same TEGa partial pressure was used to prepare (d).

The Ga growth time was set to 1 s for all samples. Samples (a) and (b) were deposited at 375 °C and 400 °C respectively with a Ga partial pressure of 1.5×10^{-2} mbar. For the samples displayed in (c) and (d) a Ga partial pressure of 7.6×10^{-3} mbar was applied, while

a growth temperature of 375 °C or 450 °C was chosen. Due to the limited decomposition of the Ga precursor the amount of material deposited on the samples prepared with lower growth temperature (a) and (c) is clearly decreased compared to that on the samples with higher growth temperature (b) and accordingly (d). For both samples grown at 375 °C only small aggregates form. Additionally, the density of structures forming on the surface is low. The underlying Si (001) surface structure is still clearly visible here. In comparison, for both related samples deposited at a higher Ga growth temperature, the size as well as the density of the Ga-containing structures is significantly increased. A more detailed correlation between the size or number of structures forming and the growth temperature, utilizing also additional samples not shown here, is illustrated in fig. 4.15.
To investigate the temperature dependency of the Ga diffusion into the Si in this temperature range, two samples grown with a Ga deposition temperature of 400 °C and 450 °C respectively were analyzed by HAADF STEM. Representative images of these measurements are shown in fig. 4.13 (a) for the sample grown at 400 °C and (b) for the sample grown at 450 °C.

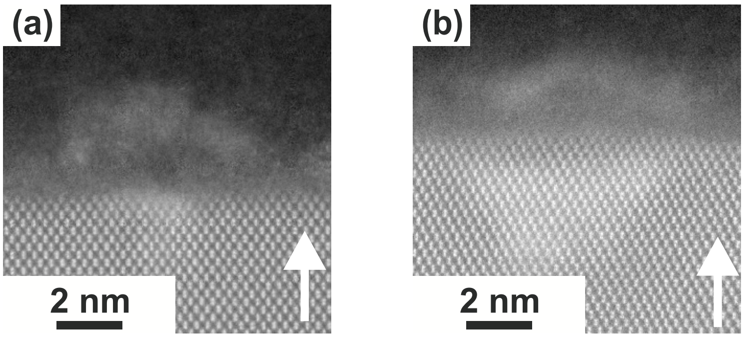

Figure 4.13: Cross-sectional HAADF STEM micrographs of structures formed after 1 s of TEGa deposition at 400 °C (a) and 450 °C (b) respectively, as already shown in the AFM images in fig. 4.12 (b) and (d).

The growth time was set to 1 s for both samples. But, for the sample using a Ga growth temperature of 400 °C (a) the TEGa partial pressure was increased by a factor of 2 to 1.5×10^{-2} mbar in comparison to the sample grown at 450 °C (b), using a TEGa partial pressure of 7.6×10^{-3} mbar. This was done to compensate for the lower decomposition rate at the lower growth temperature. While for both deposition temperatures seemingly a comparable amount of material aggregates on the Si surface, for the structure formed at 400 °C the amount of Ga diffused into the Si seems decreased in comparison with the structure formed at 450 °C. These findings confirm the assumption that the Ga diffusion into the Si substrate strongly depends on the deposition temperature and is hindered by low temperatures. This behaviour can be explained by reduced solubility of Si in Ga with decreasing temperature [93]. Less Si is solved in the same amount of Ga at lower growth temperatures, resulting in smaller structures in the Si. Adjusting the growth temperatures to lower values would therefore lead to a decreased intermixing of Ga and Si and a reduced roughening of the Si surface. However, in this temperature regime a significant increase of the Ga partial pressure with decreasing deposition temperature is necessary to compensate the dropping decomposition rate.

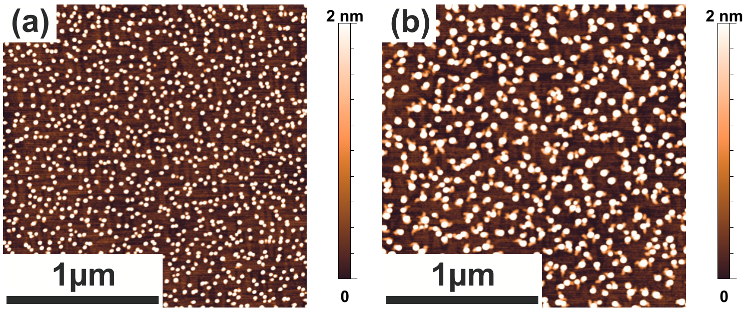

Figure 4.14: AFM images of samples after 15 s of TEGa deposition at different growth temperatures, namely 450 °C (a) and 550 °C (b), with otherwise identical growth parameters.

To clarify, whether the temperature depended changes in the structures forming after TEGa deposition seen in fig 4.12 are merely due to the drastically reduced decomposition rate at relatively low temperatures, the deposition temperature was also increased from 450 °C. AFM images of two samples after TEGa was deposited for 15 s using a Ga partial pressure of 7.6×10^{-4} mbar are displayed in fig. 4.14. For the sample shown in (a) the Ga growth temperature was set to 450 °C while for (b) a significantly higher Ga growth temperature of 550 °C was chosen. While the proportional surface coverage is similar for both samples, for the deposition at a higher temperature less but bigger structures form. This behaviour is in agreement with the finding for lower deposition temperatures and is also illustrated in fig. 4.15, which displays the changes in the number and size of the structures forming after TEGa deposition at different growth temperatures. As mentioned before, an increasing amount of TEGa precursor was offered, corresponding to an increasing value for the TEGa partial pressure multiplied by the growth time chosen, for samples grown at decreasing growth temperatures in the low temperature regime, to compensate for the decreasing decomposition rate. At higher temperatures the amount of Ga offered was increased again for other reasons. But, as can be seen in the diagram, apparently this has no influence on the temperature dependency. To help with the interpretation of the results, samples grown with equal conditions, except for the growth temperature, are connected by dashed lines.

For low temperatures the number as well as the size of the mounds increases with increasing growth temperature. The size of the structures rises further for higher temperatures. The number of structures, though, starts decreasing again at the same time. A rise in the structure's size as well as the decrease in their number, observed for deposition temperatures above 400 °C, can be explained by the rising mobility of the Ga atoms on the Si surface for increasing temperature, as this leads to an enhanced converging

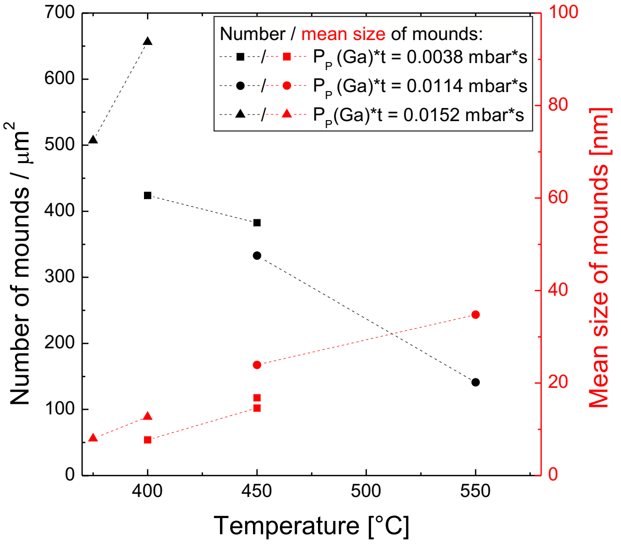

Figure 4.15: Correlation between growth temperature and the number or the mean size of structures formed after TEGa deposition for samples grown under different conditions.

of the Ga-containing aggregates. A contradictory behaviour is observed only in the low temperature regime below 400 °C, where an increase in the deposition temperature results in a significant gain of the number of structures occurring on the surface. This is probably due to the markedly limited decomposition of the Ga precursor at 375 °C leading to a hindered Ga deposition at this temperature. Presumably, an increase in the growth temperature initially induces a deposition of a significantly larger amount of Ga and therefore an increased number of structures. This effect can not be compensated by an enhanced merging of the structures, as the mobility on the surface is not sufficiently large at this temperature.

Significant differences appear between the individual data points, for samples grown at the same growth temperature but with different growth times or Ga partial pressures. This is particularly striking for the number of mounds at 400 °C. For the two samples grown at this temperature, the Ga deposition time was kept constant at 1 s while the partial pressure was reduced for the sample represented by the rectangle in comparison with the sample represented by the triangular symbol. As shown in fig. 4.9, a decrease in the Ga partial pressure results in a clear reduction of the number of structures forming and concurrently to a slight decrease in their size. This is in full agreement with the results presented here, as both dependencies are observed here, too. At 450 °C the amount of Ga was raised by a factor of 3 from the deposition of the sample represented by the rectangle symbol to that of the sample displayed by the circle. This led to a gain in the mean size of the structures and a simultaneous decrease in their number. The increase in the Ga amount was achieved by raising the Ga deposition time from 1 s to 15 s, while the Ga partial pressure was decreased at the same time from 3.8×10^{-3} mbar to 7.6×10^{-4} mbar. An increase in the deposition time leads to a significant gain in the mean size of the forming structures, as seen here, while a decrease in the Ga partial pressure has a considerably smaller effect on this parameter. This can be observed in fig. 4.9. At the same time it was shown, that the number of structures occurring on the surface strongly decreases with a reduction of the Ga partial pressure. The number additionally decreases with an increase in the growth time for sufficiently long deposition times. Both, the reduction of the number of aggregates forming as well as the raise in their size are therefore in good agreement with the findings in fig. 4.9.

Influence of the silicon (001) surface properties

To analyse the influence of the substrate's surface properties, such as, for examples, the nature of the step edges, on the growth, the TEGa deposition was performed on different Si (001) substrates and with varying Si pretreatments. Fig. 4.16 displays samples after TEGa deposition each for 1 s at 450 °C using a TEGa partial pressure of 3.8×10^{-3} mbar for the samples presented in (a), (b) and (c), corresponding to a deposition of 0.7 MLs of Ga, judging from the results on the GaP deposition on Si. For the preparation of the samples displayed in (d) and (e) comparable growth conditions were applied, but the TEGa partial pressure was decreased by a factor of 5 to 7.6×10^{-4} mbar.

Samples (a), (b) and (c) differ in the Si substrate used as well as in the treatment of the Si buffer after its growth. For the samples shown in fig. 4.16 (a) and (b) the Si buffer was annealed for 10 min at 975 °C in H_2 atmosphere, applying a high reactor pressure, as described in section 4.1. This high-temperature treatment was not performed for the samples shown in fig. 4.16 (c). Here the Si buffer was cooled down directly after growth. Samples (a) and (b) were prepared equally, but they differ in the Si substrate used. A nominally exact Si (001) substrate with an off-cut of up to 1° in an arbitrary direction was used for the samples shown in (a) and (c). The Si (001) substrate used for (b) holds an intentional 0.1° misorientation in the [110]-direction. These modifications in the pretreatment and substrates' off-cut lead to a difference in the structure of the surface step edges. Due to the high-temperature annealing only applied for samples (a) and (b), smooth step edges develop, possessing less length than the disordered step edges observed without an annealing in (c). Additionally, larger terraces and therefore less step edges form for sample (a) than for (b), due to the difference in off-cut. Caused by the appropriate off-cut in [110]-direction of sample (b), nicely ordered D_A steps with protruding triangular S_B steps occur, as discussed in section 4.1 and shown by means of STM. No STM investigation was performed on the Si (001) buffer used for the sample (a). But elongated gaps, which represent rows of Si surface vacancies, can be observed in the AFM image on every second terrace. It was found by STM that these rows form

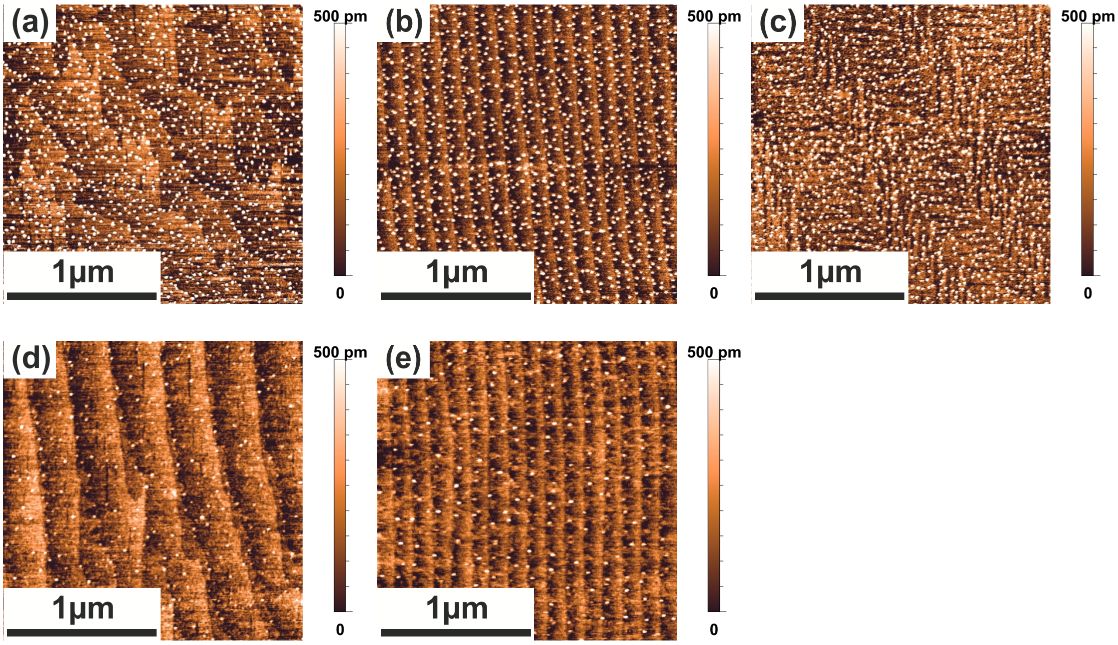

Figure 4.16: AFM images of different Si (001) substrates after 1 s of TEGa deposition at 450 °C, with different pretreatments of the Si buffer. For sample (a) and (b) an annealing at 975 °C at a high H_2 reactor pressure was performed, while this annealing was omitted for (c). Samples (d) and (e) were prepared similar to (a) and (b) respectively, both with an high-temperature annealing of the Si buffer. For (a) and (b), as well as for (d) and (e) different Si (001) substrates were used. A TEGa partial pressure of 3.8×10^{-3} mbar was used for (a), (b), and (c). This partial pressure was decreased to 7.6×10^{-4} mbar for (d) and (e).

along the Si dimer rows (fig. 4.2). Therefore, they reveal the direction of the dimer rows to be parallel to the step edges of the terraces they appear on. This indicates the lower step edges of these terraces to be type A edges. As gaps only appear on alternating steps, the surface is presumably build by S_A and S_B steps. An evaluation of the changes in the aggregates, that formed on the different surfaces after TEGa deposition, is summarized in the following table:

	Surface coverage [%]	**Number of mounds / 1µm^2**	**Mean size of mounds [nm]**
Sample (a)	7.15	354	13.7
Sample (b)	6.16	368	12.3
Sample (c)	7.73	472	12.2

Independent from the annealing, the proportional surface coverage after the TEGa deposition is similar for all samples. However, on the substrate without high-temperature annealing (c) mounds with a considerably higher density form compared with the ones on the substrates with a previous high-temperature annealing of the buffer (a) and (b). The size of the mounds is slightly larger for sample (a) and similar for both other samples. However, due to the small height of the structures, i.e., the low variance in height between the mounds and the surface, errors arise for the statistical evaluation, as the mounds might not have been detected precisely. Small changes in their size or their number, like between (a) and (b), might therefore be caused by statistical errors. The significant difference between the number of mounds found on (a) or (b) and on (c), though, can be explained by the modification in the Si buffer treatment. Measurement (a) and (b) reveal that Ga mounds preferably form along the S_B step edges, but not along the S_A edges in (a), and frame the protruding small terraces of the Si (001) surface, which possess S_B steps edges, in (b). This particularity is even more in evidence for the samples presented in the images (d) and (e), which were prepared similarly to the samples shown in (a) and (b) respectively, however, with a 5 times lower TEGa partial pressure. Since therefore less structures formed on the surface, it can clearly be seen, that these are ordered along the protruding S_B but neither along the S_A steps edges in (d) nor along the D_A step edges in (e). In (e) some aggregates containing Ga also form on the S_A terraces, probably due to the large size of these. A favored formation of mounds at the Si surface vacancies, which also exhibit type B step edges, can be observed, though. The formation at S_B but not S_A steps can be explained by the difference in their bond coordination as already described in 4.1. The dimer and electronic structure at S_B but not S_A steps differs considerably from the bond structure of the reconstructed Si (001) surface. Besides the preferential formation of the structures, which contain Ga, along the S_B bonds, this can also account for the higher density of aggregates appearing on sample (c) in comparison to sample (a) and (b) in fig. 4.16. Since rougher Si step edges form without a high-temperature annealing of the buffer, the length of the step edges is increased for this pretreatment and therefore more possibilities for the formation of aggregates exist.

On silicon (111)

As mentioned before, it is assumed that diffusion of Ga in Si (001) leads to the formation of Si {111} limited Ga-containing pyramids due to the Si (111) planes being more stable than the Si (001) planes. This assumption is based on first principles density functional theory (DFT) computations. Experimental results on GaN growth on Si (111) revealed that Ga also etches into the Si (111) surface [10], [94]. However, the structures formed in Si (111) have not been studied extensively yet. Additionally, GaN growth is usually performed at considerably higher growth temperatures making those results only partly comparable to the deposition in this research. To analyze this and experimentally verify the assumption described, Ga deposition was also performed on Si (111).

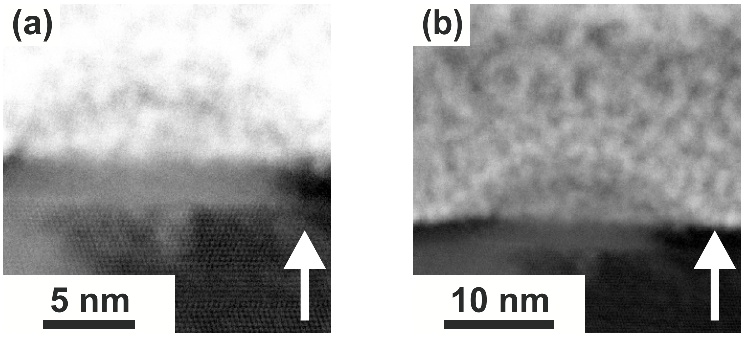

Figure 4.17: Cross-sectional HAADF STEM images of a sample after 2 s of TEGa deposition on Si (111) at 450 °C with two different magnifications.

The HAADF STEM measurement for this sample (fig. 4.17) reveals a semicircular structure with a contrast brighter than Si, originating from the deposited Ga. Although the structure appears blurred, partially due to contamination by the electron beam, the structure's lower boundary on the Si (111) plane is clearly observable. Confirming the assumption that the particular structures observed for Ga deposition on Si (001) form due to the greater stability of the Si {111} planes [91], no pyramidal structure formed here, but the Ga-containing aggregate also exhibits a boundary on the Si (111) plane.
However, these results have to be treated with some caution, since the TEM specimen was not prepared as described in section 3.3 and done for all other samples in this study, but by cutting the samples with a focussed ion beam. The surface is therefore covered by tungsten showing a contrast brighter than Ga, rather than a glue containing C, which was used for all other specimens. It is not known how this different preparation might influence the Ga-containing structure.

4.2.2 Trimethylgallium deposition

For the deposition of TEGa on Si an amorphous C-containing layer appears across the whole Si surface, as can be seen in fig. 4.6. This may be caused by the deposition of ethylene residual groups or of decomposition products thereof, as TEGa presumably decomposes primarily via β-hydride elimination at high temperatures yielding Ga, ethylene and H. While the ultimate aim of this work is the growth of graphene, i.e., the growth of a C structure, and this deposition might appear as a beneficial origin for this, it was found that the amorphous layer bears several difficulties. Firstly, the deposition occurs solely with the Ga deposition and it is not possible to control both processes individually. More importantly, while an amorphous layer was identified by STEM, no C originated signal was detected by Raman spectroscopy for any sample after TEGa deposition on Si. This implies that no carbonic material of any noticeable order was deposited, but rather a hydrocarbon-containing, purely amorphous layer. However, this layer entirely covers the metallic Ga and it has to be assumed that it might therefore hinder the catalytic effect on the subsequent growth of any carbonic structure via the deposition of a C precursor. Consequently, the deposition of a different Ga precursor, namely TMGa, was investigated and the results will be presented in the following section. Based on the different reaction pathways for the decomposition, differing residual organic groups occur for the deposition of TMGa instead of TEGa. It is assumed that TMGa decomposes via H-transfer processes generating Ga, methane, H and C [95]. While the C incorporation for the growth of, for example, GaAs can be drastically decreased by the usage of the Ga precursor TEGa rather than TMGa [96], the growth processes leading to the formation of the C-containing layer may be entirely different due to the catalytic effect of the metallic Ga. As no formation of polyethylene chains is expected from the methane resulting from the TMGa decomposition, no deposition of an amorphous carbonic layer is anticipated.

For the deposition of TMGa, different growth parameters need to be applied with respect to the deposition of TEGa. This is due to the 50% decomposition temperatures of TMGa in H_2 being significantly higher than that of TEGa [12], [97]. TMGa only decomposes completely at higher reactor temperatures than TEGa. Hence, for the deposition of TMGa, both the Ga partial pressure as well as partially also the temperature were increased compared to when TEGa was used.

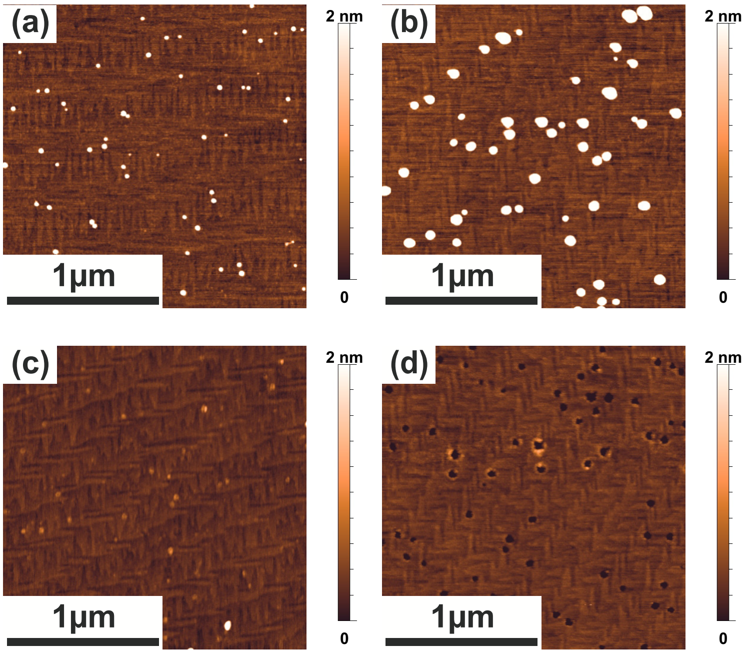

Figure 4.18: AFM images of Si (001) surfaces after 10 s of TMGa deposition at 450 °C (a) and 500 °C (b) and of the same samples after etching in 30% HCl for 30 s ((c) and (d) respectively).

AFM images of two samples after TMGa deposition on Si (001) at different temperatures are depicted in fig. 4.18 (a) and (b). For both samples the Ga deposition proceeded for 10 s using a TMGa partial pressure of 0.1 mbar. This means that the Ga partial pressure was increased by a factor of up to 130 for TMGa with respect to the partial pressure used for TEGa. For the sample shown in fig. 4.18 (a) a Ga growth temperature of 450 °C was chosen, adapted from the TEGa deposition. This growth temperature was increased to 500 °C for the sample presented in 4.18 (b). For the deposition at the lower temperature (a) considerably smaller mounds form than for the higher growth temperature (b), while the number of structures is comparable for both samples. The structure of the Si (001) surface is still clearly visible after the TMGa deposition and does not seem affected by it. Comparing these structures with samples grown with TEGa using otherwise similar growth parameters, as shown for example in fig. 4.4, one sees that for the usage of TMGa the number of mounds formed is considerably decreased, while their size is largely increased. These observations indicate that the growth process of the TMGa structures differs markedly from that of the TEGa structures. This behaviour might be explained by the decomposition of TMGa not being induced by the H covered Si surface but only occurring in the presence of multiple precursor molecules. As the H_2 carrier gas pressure is by far larger than the TMGa pressure in the reactor, the probability of TMGa molecules clustering is low. Hence, most TMGa molecules provided pass the growth reactor undecomposed. Firstly, this would account for the necessity of a largely increased TMGa partial pressure and secondly, for the formation of a smaller quantity of considerably larger structures in comparison to the deposition of TEGa. Additionally, for TMGa usage the deposited material might be more mobile at growth temperature than for the TEGa deposition where the amorphous layer might hinder a merging of the Ga-containing structures.

Both samples shown in fig. 4.18 (a) and (b) were etched in 30% HCl for 30 s each. AFM images of these samples after etching are displayed in fig. 4.18 (c) and (d). For either sample the structures formed can be etched off with 30% HCl. In contrast to the findings on TEGa, the structures deposited using TMGa do not appear to be covered by a passivating layer. While remains stay on the Si surface for the sample grown at 450 °C (c), holes are found in the surface of the sample grown at 500 °C (d). The holes emerge due to Ga diffusing into the Si, forming structures and replacing Si atoms from their lattice sites there; as seen for TEGa. The Si atoms displaced from their lattice sites are either dissolved in the liquid Ga or build new structures if the Ga is saturated with Si. These forming Si structures can partly be observed in image (d) exhibiting small elevations surrounding the holes in the Si surface. Some Si remains, possibly positioned atop the Ga aggregates, might be removed jointly with the Ga. The influence of the growth temperature on this diffusion has already been described for TEGa, as shown in fig. 4.13, demonstrating that the amount of Ga diffusing into the Si and the size of the structures forming in the substrate increases with increasing deposition temperature. A corresponding temperature dependency for the TMGa deposition is indicated in fig. 4.18. For the structures deposited at 450 °C the small holes occurring in the surface might not be detectable by AFM, due to its limited resolution, and only the Si remnants forming on the surface can be observed.

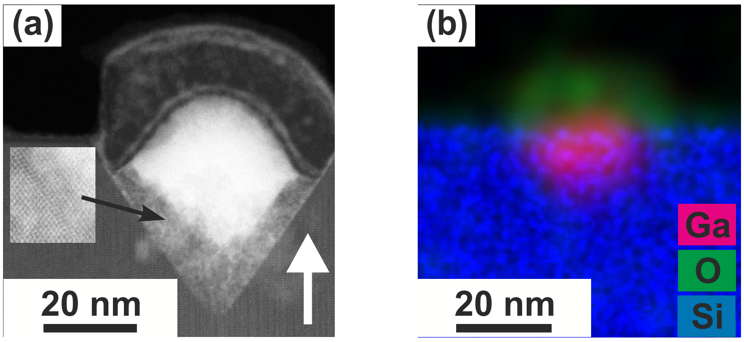

Figure 4.19: Cross-sectional HAADF STEM image (a) and EDX map (b) of a sample after TMGa deposition under the same growth conditions as used for the sample shown in fig. 4.18 (b). The EDX map only displays the EDX signals detected for Ga (red), Si (blue) and O (green).

For a thorough insight into the growth process, STEM was performed on a sample prepared using growth conditions equivalent to those employed for the sample presented in fig. 4.18 (b). A cross-sectional HAADF STEM image and a corresponding EDX measurement are displayed in fig. 4.19. The STEM image (a) exhibits bright pyramidal structures forming, limited by the more stable Si {111} lattice planes, as already seen for TEGa. The EDX map generated at a similar pyramidal structure (b), showing the EDX signals detected for Ga, Si and O, provides evidence that the bright contrast is generated by Ga diffused into Si. As already detected by AFM, the structures formed by this precursor are considerably larger than those observed for the TEGa deposition. Unlike for the STEM measurements at structures deposited with TEGa, here the Si crystal lattice is not detectable in the center of the pyramidal structure. Presumably, this is based on the considerably increased size of the Ga-containing structure relative to the surrounding intact Si lattice in the direction of the electron beam, as the sample thickness at the position investigated is approximately in the range of the structure's size for this sample. A region with a reduced contrast to the Si is apparent between the bright center of the Ga-containing structures and the pure Si lattice. Additionally, in this boundary area staking faults occur in the Si lattice, as shown in the inset in fig. 4.19 (a). These might result from the displaced Si being dissolved in the liquid Ga at the deposition temperature, as depicted schematically in fig. 4.20 (a). During the cool-down of the sample, after the Ga deposition, an oversaturated compound develops, as the solubility of Si in Ga decreases with decreasing temperature. Hence, as in liquid phase epitaxy, some Si recrystallizes at the interface to the original Si crystal lattice, as illustrated in fig. 4.20 (b), resulting in an area with a reduced Ga content. Since this growth process occurs at reasonably low temperatures, lattice defects emerge.

A well resolved EDX measurements of an equivalent pyramidal structure performed on a sample deposited using corresponding growth conditions is displayed in fig. 4.21. It

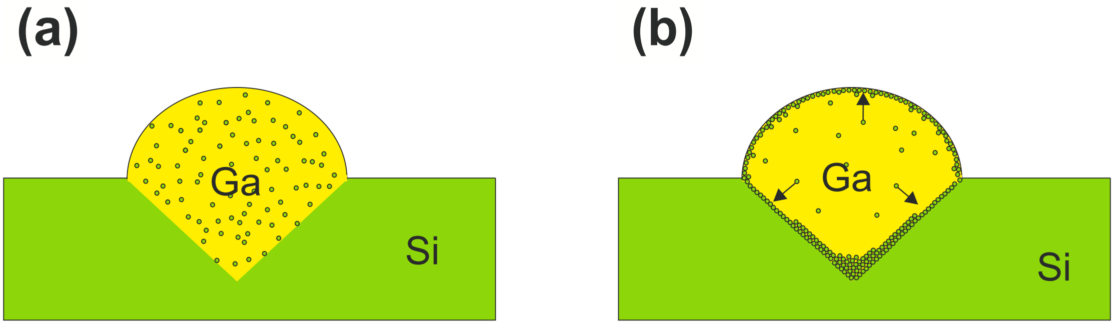

Figure 4.20: Schematic of the intermixing of Ga and Si at growth temperature (a) and during the sample cool-down (b), as assumed for fig. 4.19.

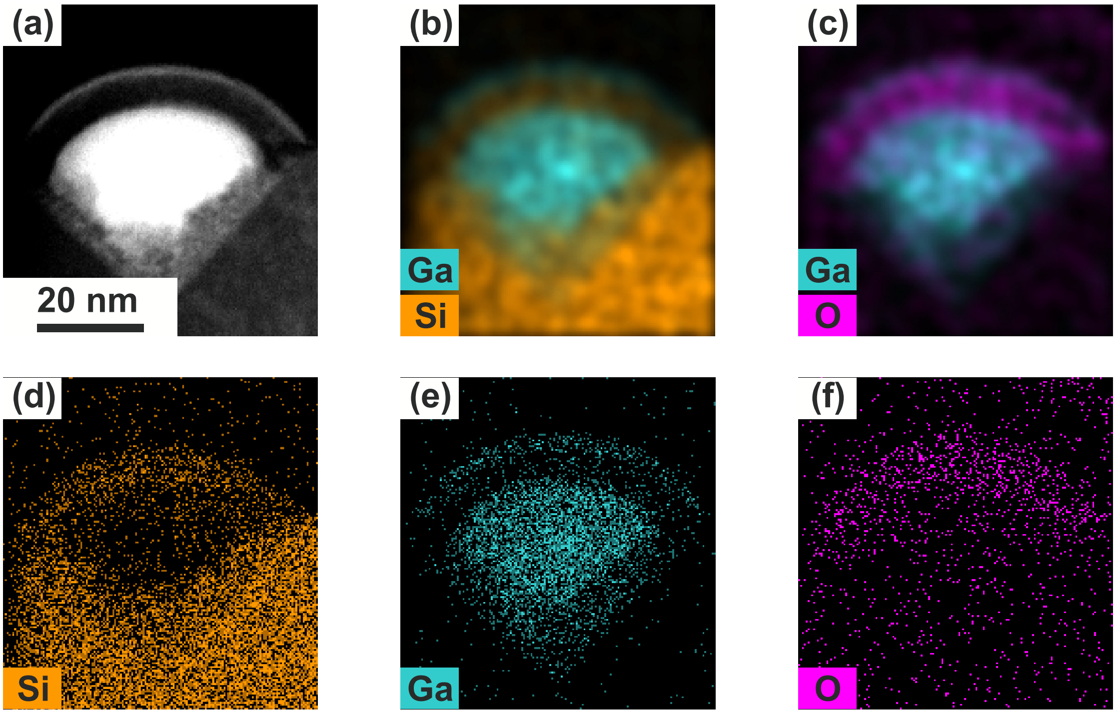

Figure 4.21: Cross-sectional HAADF STEM image (a) and EDX maps (b)-(f) of a sample after TMGa deposition under the same growth conditions as used for the samples shown in fig. 4.18 (b) and 4.19, exhibiting the Si (orange), Ga (turquoise) and O (pink) distribution in and around a pyramidal structure.

clarifies the composition of the pyramidal structures and the amorphous caps. Image (a) shows a STEM image of the structure investigated, while images (b) and (c) show filtered combined EDX maps of the Ga and Si or the Ga and O distribution. Images (d), (e) and (f) display unfiltered EDX maps of the Si, Ga or O signals. The measurements clearly reveal that, while the bright center of the pyramidal structure contains a high amount of Ga, a significant amount of Si can be found in all outer regions of it. This was already reasoned in the previous paragraph. However, fig. 4.21 (b) and (d) verify that a formation of a Si-containing layer at the edge of the Ga-containing structure is also true for the coverage of it. A thin Ga layer, appearing bright in the HAADF STEM measurement, again tops the Si cap as can be seen in image (b) and (e). A considerable amount of O in the Si-containing layer covering the pyramidal Ga structure was observed, as shown in fig. 4.21 (c) and (f). As no O is present in the reactor during the deposition, this alloy presumably developed following the growth, when the sample was handled in air with no further precaution, resulting in a fast oxidization of the Si. For crystalline Si, only a thin, self-limiting silicon oxide layer forms when it is exposed to air. It is, however, assumed that the Si-containing cap is rather built up by amorphous than crystalline Si; the oxidation process might therefore differ from that occurring at the Si surface. A possible C deposition during the growth process can not be verified by this EDX measurement, as C was deposited as a protective layer during the preparation of this STEM samples.

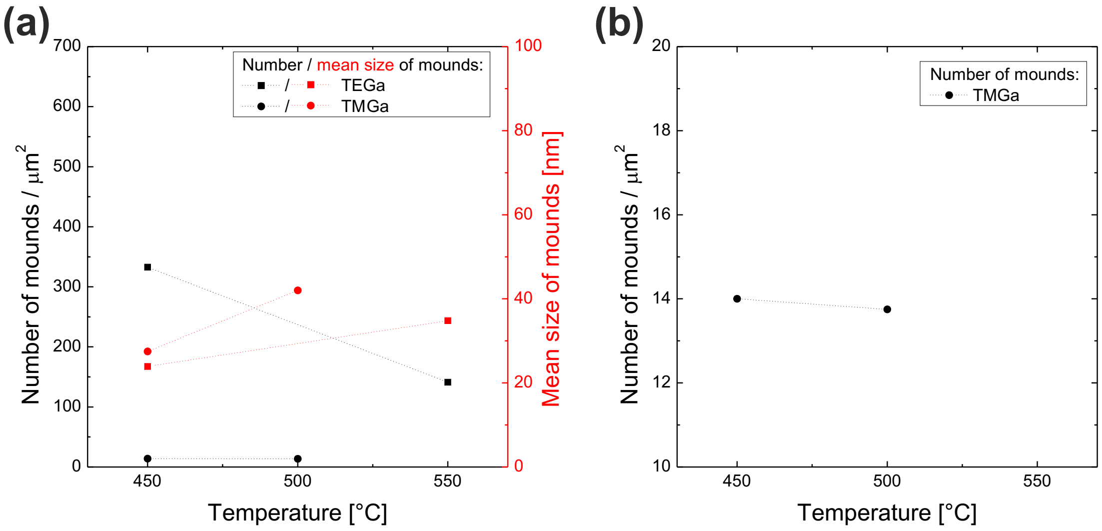

Figure 4.22: Comparison of aggregates forming and their temperature dependency for the deposition of TEGa and TMGa on Si (a). For better visibility a section of (a), showing the number of mounds forming for TMGa deposition, is presented in (b).

Some differences and similarities between the deposition of TEGa and TMGa have already been stated in the preceding paragraph. For a deeper comprehension of the temperature dependency of the deposition fig. 4.22 (a) depicts the number and mean size of structures forming at different temperatures for the two Ga precursors. For both precursors used, the number of mounds decreases with increasing growth temperature while their size increases. For TEGa, though, a drastic decrease in the number of structures forming is observed, whereas for TMGa only a marginal change was found, which is displayed more pronounced in an enlarged section of the diagram shown in fig. 4.22 (b). This change observed for TMGa might also be caused merely by statistical effects. The size of mounds changes much more with temperature for the usage of TMGa than for that of TEGa. This comparison suggests distinct differences in the temperature dependent behaviour of both precursors. For TMGa the amount of precursor decomposed and consequently the amount of material deposited increases considerably for an increase in growth temperature in this temperature regime. Therefore, the size of structures forming increases. As the material is reasonably mobile on the surface already at 450 °C, no change in the density, i.e., the number of aggregates, occurs. For TEGa the precursor is already decomposed to a great extent at 450 °C. Hence, the amount of material deposited does not change as drastically due to the increase in growth temperature. Apparently though, the mobility of the deposited material on the surface increases with increasing temperature leading to a decrease in the number of mounds with an interrelated increase in their size. Especially remarkable is the great difference in the number of structures forming for each precursor. While the mean size of the mounds is similar for both precursors for a deposition at 450 °C, their number is increased by a factor of 20 for TEGa in comparison to TMGa, implying that for the chosen growth conditions considerably less Ga was deposited for TMGa than for TEGa at 450 °C. Two possible explanation can be found for the difference in the number of aggregates. Firstly, the greater mobility of the material deposited using TMGa compared to that for TEGa deposition leads to a smaller density of the structures as the mounds merge more commonly. Secondly, as already stated previously, the TMGa presumably only decomposes if multiple precursor molecules are present. Therefore, mounds develop only if multiple Ga atoms already aggregate during the deposition, leading to a smaller density of structures forming.

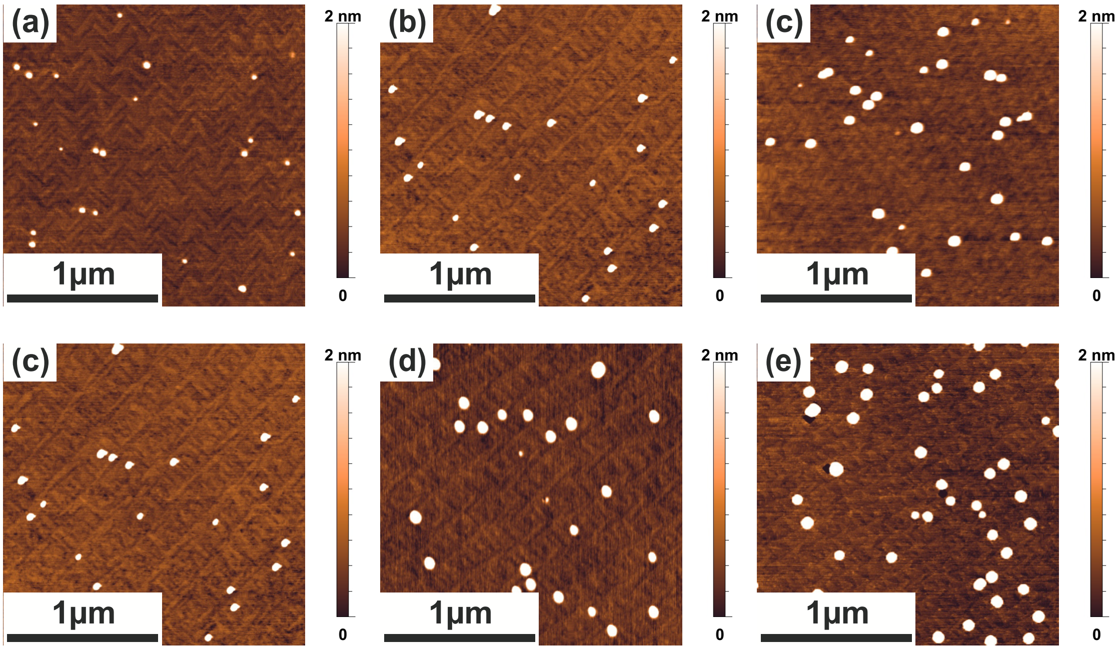

Figure 4.23: AFM images of Si (001) surfaces after a deposition of TMGa at 450 °C with varying Ga partial pressure (a)-(c) and deposition time (d)-(f) respectively and otherwise equal growth conditions.

As before for the TEGa deposition, also for the growth using TMGa as Ga precursor, the structures' dependency on a variation of the growth time or the partial pressure was analysed. This knowledge, combined with the knowledge of the temperature dependency, is important for the controllability of the deposition of the structures. Therefore, AFM micrographs of samples after a TMGa deposition on Si (001) at a Ga growth temperature of 450 °C are shown in fig. 4.23. For the samples displayed in the images (a), (b) and (c) TMGa was deposited for 10 s each. The TMGa partial pressure was increased from 0.2 mbar in (a) to 0.4 mbar in (b) and finally to 1 mbar in (c). For the growth of the samples shown in (d), (e) and (f) the TMGa partial pressure was set to 0.4 mbar while the growth time was increased from 10 s in (d) to 20 s in (e) and finally to 40 s in (f). Mounds form on the surface for all samples , while the Si surface structure is still visible. A comprehensive evaluation of the changes in structures' size and number is depicted in fig. 4.24. Special attention should be given to the samples where the highest Ga partial pressure (c) and accordingly the longest deposition time (f) was applied. After the TMGa deposition using a partial pressure of 1 mbar (c), the Si surface structure is still observable, as for the other samples, but appears diffuse, implying that this high Ga supply might lead to a change of the whole surface and not only to a formation of aggregates. After a deposition time of 40 s (f) holes appear in the Si neighbouring mounds in some cases. This is presumably due to Ga moving on the surface, even after etching into the Si, during the extented deposition time.

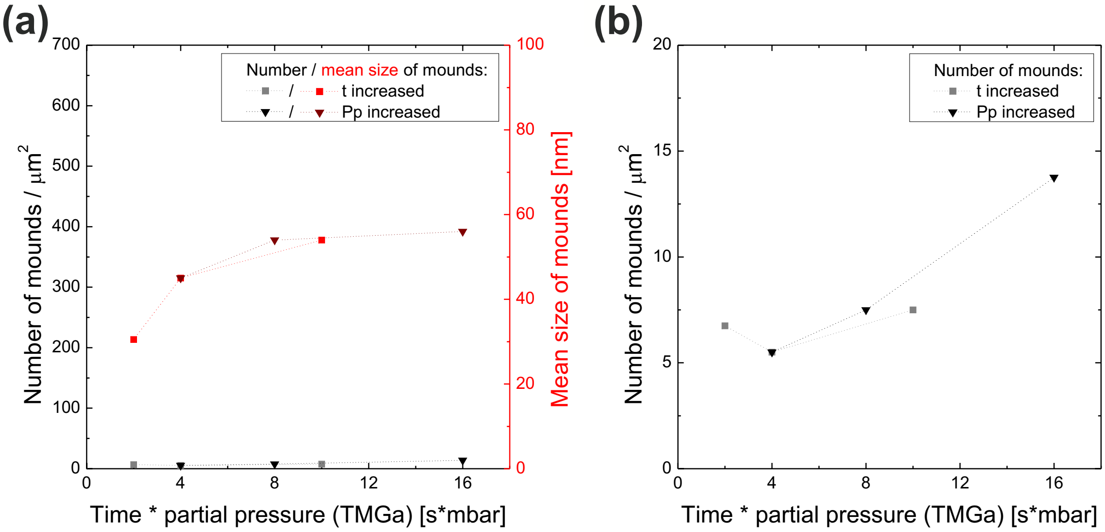

Figure 4.24: Evaluation of the samples shown in fig. 4.23, displaying the dependency of the number and the mean size of the structures on the deposition time and the Ga partial pressure for TMGa deposition at 450 °C (a). The dependency of the number of mounds is pictured more explicitly in an enlarged section of (a) in (b)

An increase in the mean size of mounds forming is observed both for an increase in the Ga partial pressure and an increase in the deposition time used. For the former also an increase in the number of structures is found. For an increase in deposition time, though, first a slight decrease in the number of mounds is observed followed by an increase again. The increase in the size of the structures is observed clearly for the shorter growth times and the lower partial pressures respectively, but then seemingly reaches a saturation. The significant increase in the number of structures forming for a rising TMGa partial pressure in combination with the only minor growth of their mean size is in accordance with the TMGa decomposition model suggested earlier. It is assumed that at 450 °C TMGa only decomposes in the presence of multiple precursor molecules. The probability of a clustering of TMGa molecules rises with increasing TMGa partial pressure resulting in an increased formation of Ga aggregates, however this only marginally influences their size. A raise in the growth time leads to an increased merging of the Ga structures, but also new mounds can form on the surface. As both processes run simultaneously leading to competing results, no clear tendency was found here. Apparently, for shorter deposition times the increasing merging of the Ga-containing structures dominates the process, while for longer growth times the formation of new structures plays an important role. However, one has to keep in mind that only a small sample section is used for the evaluation and statistical deviations might also account for the rather small variations found here.

4.2.3 Annealing of gallium-pretreated silicon

Results on the deposition of Ga with TEGa and TMGa were presented in the previous section. Following the deposition, the metallic Ga should be used as a catalyst for further growth of C structures. Therefore, the Ga-pretreated surfaces presumably need to be exposed to a high temperature, i.e., above 400 °C, for some amount of time. The alteration of the Ga aggregates due to this treatment was investigated. The results will be presented in this section, first for a high annealing temperature, i.e., 800 °C, then for lower temperatures. All annealings were performed in the growth reactor in H_2 atmosphere.

Two samples with different Ga pretreatments after an annealing at 800 °C are shown in fig. 4.25. The AFM image shown in fig. 4.25 (a) was measured at a sample, which was initially prepared with TMGa at 500 °C, using a growth time of 10 s and a TMGa partial pressure of 0.1 mbar. It can be compared to the corresponding AFM image of an as-grown sample presented in fig. 4.18 (b). An AFM measurement after an annealing of a sample where TEGa was deposited for 15 s at 450 °C using a TEGa partial pressure of 7.6×10^{-4} mbar is displayed in fig. 4.25 (b). The as-grown sample corresponding to this sample is shown in fig. 4.7 (e). Most Ga structures have disappeared after the annealing for the sample grown with TMGa, leaving voids in the Si surface and few large structures probably originating from remaining Ga, that merged during the high-temperature annealing. Less changes can be observed due to the annealing for the sample where TEGa was deposited. Here only the size of the structures on the surface as well as their density was influenced

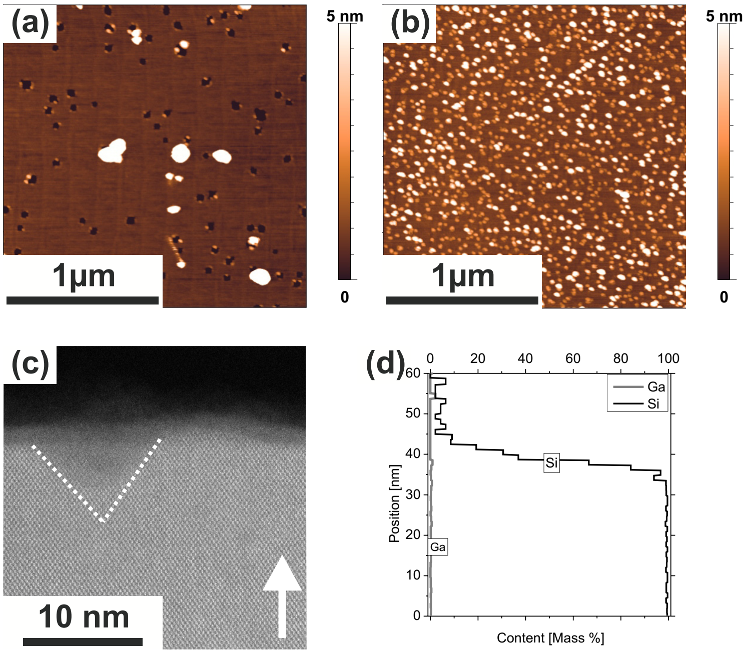

Figure 4.25: AFM ((a) and (b)), cross-sectional HAADF STEM (c) and EDX (d) measurement taken after an annealing at 800°C of samples grown with TMGa (a) and TEGa (b), (c) and (d).

by the annealing. The STEM image, though, presented in fig. 4.25 (c), which was recorded on the same sample, does not reveal any bright pyramidal structure any more like in the as-grown samples (compare fig. 4.5). Rather, structures with a darker contrast occur in the Si, replacing those Ga-containing structures. An EDX line profile (fig. 4.25 (d)) measured along the growth direction at one of these structures clarifies that virtually no Ga is left at the Si surface. Instead voids remained in the Si. Judging from the AFM (b) as well as the STEM (c) image, the amorphous C-containing layer was affected only little by the annealing. As it remains on the surface, covering the voids, no holes were found by AFM for the sample grown using TEGa.

Two hypotheses are possible to explain the disappearance of the Ga from the Si surface. Firstly, it was shown by [95] that at temperatures above 900 K considerable amounts of Ga desorb from a Si (001) surface. An annealing at 800 °C might, thus, be sufficient to desorb any Ga deposited previously. Therefore, though, it has to be assumed that for the TEGa pretreated sample the Ga desorbed from the surface through the amorphous carbonic layer, which still seems intact after the annealing. Secondly, it is presumable that, due to the high annealing temperature, the Ga diffuses further into the Si, distributing widely. Therefore it might not be detectable any more at the surface. In this case, however, defects in the Si crystal surrounding the original Ga-containing structure would be expected. No annealing at temperatures above 800 °C was performed, as presumably this would lead to a disappearance of Ga, too.

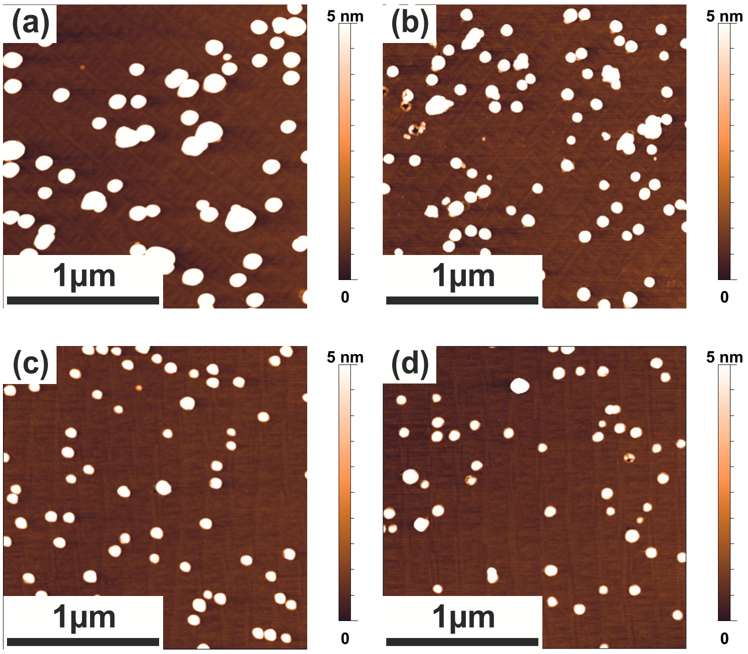

Figure 4.26: AFM image of samples after TMGa deposition followed by annealing at 500 °C (a) or 700 °C (c) for 5 min each and the same samples after 30 s of etching in 30% HCl (b) and (d) respectively.

AFM images of TMGa-pretreated samples after annealing at lower temperatures are displayed in fig. 4.26. The measurements show no major change in the sample structure caused by the annealing, both for the sample annealed at 500 °C, shown in fig. 4.26 (a), and for that annealed at 700 °C, shown in fig. 4.26 (c); a sample deposited under equivalent growth conditions without annealing is depicted in fig. 4.18 (b). But, AFM measurements of these samples after an additional etching in 30% HCL for 30 s, shown in fig. 4.26 (b) and (d) respectively, reveal that, in contrast to the Ga-containing structures on the as-grown samples, here selective etching of the structures is not possible any more for either sample. Although some voids emerged in the Si surface after etching, most structures remain unaffected by the HCL, indicating that some structural change has occurred due to the annealing.

This change can also be recognized when comparing a STEM measurement of a sample after 10 s of TMGa deposition at 500 °C before (fig. 4.27 (a)) and after (fig. 4.27 (b)) annealing. Unlike for the annealing at 800 °C, for this sample the bright Ga-containing structure can still be detected very clearly after the annealing. But, after the annealing a weaker contrast occurs between the Si lattice and the Ga-containing pyramidal structure than prior to the annealing. This suggests a stronger intermixing between the metallic Ga and the Si. As it is not assumed that a crystalline mixed Ga-Si lattice forms, supposedly at a suitable temperature further Si dissolves in the liquid Ga during the annealing. Due to this, an oversaturated Ga-Si alloy may form during the cooling down of the sample. Similar to the formation of a Si layer at the boundaries of the pyramidal Ga-containing structure

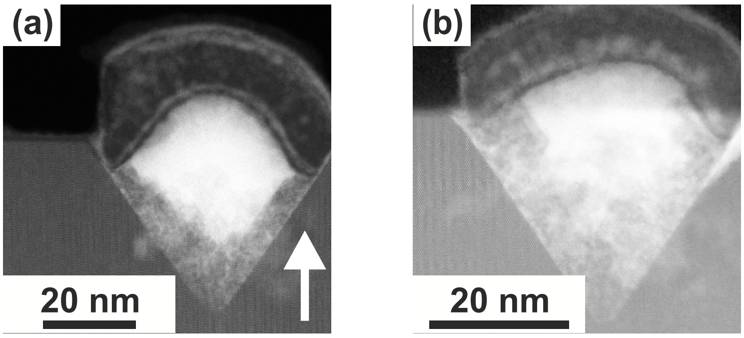

Figure 4.27: Cross-sectional HAADF STEM images of a sample after 10 s of TMGa deposition at 500 °C (a) (as already shown in fig. 4.19) and after an additional annealing for 5 min at 500 °C (b)

seen in fig. 4.19 (a) and 4.21 (b) and (d), additional Si might also reach the surface of the Ga aggregate here, building a thicker passivating layer covering the Ga-containing structures. Due to this passivating layer the selective etching of the Ga aggregates might not be possible any more. While this can be assumed from the results on annealing of the samples after TMGa depositing, no clear statement can be given on the samples using TEGa as Ga precursor. As described in section 4.2.1, for these samples an etching of the Ga-containing structures was not possible even without annealing. As no change due to the annealing was detected for these structures, no influence of an annealing at temperatures below 800 °C can be distinguished.

As a conclusion, it can be said, that a deposition of Ga with TEGa as well as with TMGa results in a formation of Ga-containing mounds on the surface. Additionally, Ga etched into Si for all conditions applied, forming pyramidal structures with boundaries on the Si {111} lattice planes. A organic layer, build by the residual groups, forms for TEGa deposition, passivating the Ga-containing mounds. This was not observed for TMGa deposition. However, here a strong intermixing of Ga and Si and a subsequent Si recrystallization at the edges of the Ga-containing structures was found. This intermixing is further enhanced by additional annealing at temperatures up to 700 °C. After annealing at higher temperatures, i.e., at 800 °C, no Ga was present any more at the surface. It was found that the properties of the deposited Ga-containing structures, such as their size and number, can be controlled by adjustment of the deposition temperature and the Ga partial pressure. However, due to the organic layer forming for TEGa deposition and the intermixing observed for TMGa deposition, the catalytic effect of Ga might not be applicable on Si (001).

4.3 Gallium phosphide surface preparation

The issue of intermixing of Si and Ga might be solved by applying a thin GaP layer to the Si substrate before Ga is deposited, to separate the liquid Ga from the Si. GaP was chosen as the interlayer due to its close similarity to Si in lattice constant. Before studying this layer on Si, some characteristics of GaP itself, e.g. its stability at high temperatures, were investigated utilizing GaP (001) substrates.

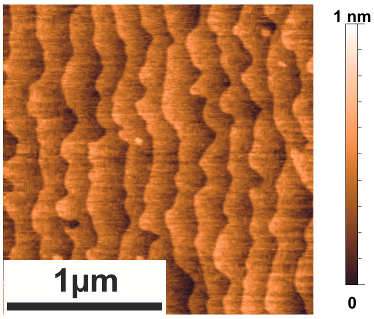

Figure 4.28: AFM image of a GaP buffer on GaP (001) after the preparation used throughout this study

The surface morphology of a GaP buffer, grown on a sulphur (S) doped GaP (001) substrate, is shown in fig. 4.28, by means of AFM. For the GaP buffer growth on GaP (001) substrates, applied here and throughout this research, first a TBP stabilized bake out of the substrate is performed at 750 °C to remove oxides from the surface, which originate from handling the substrate in air prior to growth. An approximately 300 nm thick GaP buffer is then deposited at a growth temperature of 675 °C and a TBP to TEGa ratio of 20. After the buffer growth the sample is cooled down and additional TBP is supplied until a temperature below 500 °C is reached to compensate for incongruent evaporation. For this treatment, a smooth sample surface emerges with clearly visible, regular, bilayer steps. This surface will serve as a reference for the following changes in the growth process.

First, the effect of a high-temperature annealing on the GaP surface will be discussed. For this investigation, initially a GaP buffer was grown on GaP (001) substrates using the procedure described above. Immediately following the GaP deposition, the samples were annealed for 15 min in H_2 atmosphere in the growth reactor. AFM images of samples after this preparation are displayed in fig. 4.29. The samples shown in (a) and (c) were annealed solely in H_2 atmosphere at 775 °C and 800 °C respectively. Images (b) and (d) display surfaces after an equivalent annealing again at 775 °C or 800 °C, here, however, TBP was supplied with a partial pressure of 0.15 mbar during the annealing to prevent incongruent evaporation of the group V-element P. For the unstabilized samples (a) and (c) the atomic surface steps can clearly be detected. Although no special care was taken to prevent incongruent evaporation at the rather high annealing temperatures applied, no metallic Ga appears to have formed on the GaP surface, as otherwise droplets would be present in the AFM image. Merely the size of the surface steps increases with rising annealing temperature in this temperature range. The TBP stabilized samples (b) and (d), though, exhibit a rough surface. For the sample annealed at the lower temperature

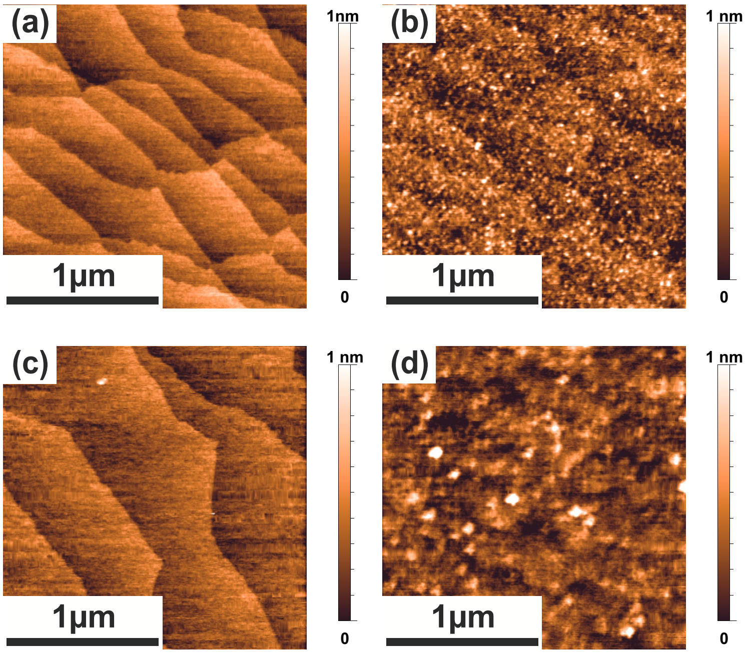

Figure 4.29: AFM images as comparison between different annealings; the samples were each annealed for 15 min without stabilization at 775 °C (a) or 800 °C (c) or TBP stabilized again at 775 °C (b) and 800 °C (d) respectively.

(b) the underlying GaP surface structure can still be recognized. A roughening of the surface during a high-temperature annealing could be caused by incongruent evaporation. However, this evaporation is not expected if TBP is supplied during the annealing but rather when no precursor is offered. It is assumed that the roughening of the surface is caused by a deposition of material rather than by evaporation. To investigate the origin of this deposition, a SIMS measurement was performed on a similarly prepared sample. For this, a sample was prepared as shown in fig. 4.29 (d), by growing a GaP buffer on GaP (001), followed by a 15 min annealing at 800 °C under TBP supply. Additionally, however, an approximately 500 nm thick GaP layer was deposited on the annealed surface as a protective layer. While an interaction of the deposited GaP with the material to be investigated on the surface can not be excluded, this layer is necessary to enable this surface to be investigated and to allow for a reliable SIMS measurement. A SIMS measurement taken on this sample is displayed in fig. 4.30.

The SIMS depth profile for the O signal reveals that the O content increases in the GaP substrate, due to handling in air, and at the surface of the GaP cap, which is partially due to measurement artifacts. The C profile also exhibits peaks at the sample surface and the surface of the GaP substrate. However, here a third, very pronounced peak appears at the surface of the GaP buffer. This result exposes that high-temperature annealing under TBP leads to the deposition of a significant amount of C on the GaP buffer. The deposited C originates from the organic residuals, i.e., from isobutane and isobutene

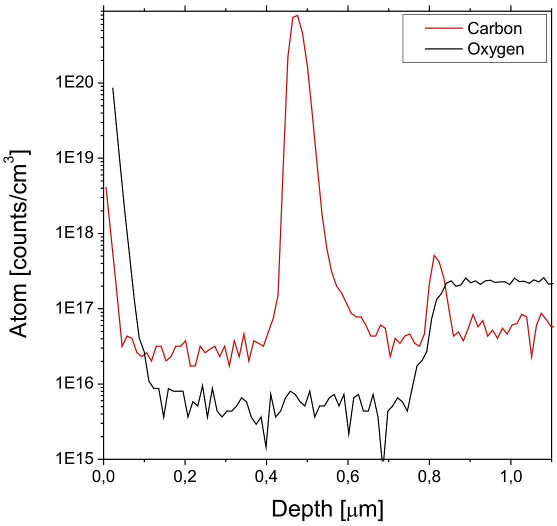

Figure 4.30: SIMS measurement of a 500 nm thick GaP cap layer grown on GaP after annealing at 800 °C under TBP, as shown in figure 4.29 (d).

molecules, that result from the TBP decomposition, which is dominated by β-hydride elimination. As the decomposition process is temperature dependent and various types of organic residual form at different temperatures, the deposition of P or C by supplying TBP is temperature dependent, too. For this reason, the C content after the bake out of the substrate at 750 °C is significantly lower than after the annealing, although a similar amount of TBP was delivered, using the same TBP partial pressure but an annealing duration of 5 min rather than 15 min. This is also in accordance with the increasing roughening of the surface with rising annealing temperature observed in fig. 4.29. Raman measurements were performed on a similar sample to clarify whether ordered C structures or purely amorphous hydrocarbon aggregates form during the annealing. However, the Raman signal of GaP exhibits a considerable background in the wavelength region critical for C analyses, i.e., at reciprocal wavenumbers above 1000 cm^{-1}, making it impossible to detect small signals in this region. Therefore, for the Raman measurement, a GaP layer on Si (001) was annealed for 15 min at 800 °C, offering the same amount of TBP as before, i.e., supplying a TBP partial pressure of 0.15 mbar. An AFM image as well as the Raman measurement for this sample are presented in fig. 4.31 (a) and (b) respectively.

The AFM image (a) displays a rough sample surface, where atomic steps can not be distinguished. Comparing this structure with the surface observed in fig. 4.29 (d) for an equivalent deposition of TBP on GaP substrate, shows a greater large scale roughness of the GaP surface here. This might be explained by the usage of heteroepitaxial GaP on Si here, as this might be more sensitive to a high-temperature treatment than GaP substrates due to the existing strain. Strain-induced step bunching might occur during the annealing. In addition, the small, three-dimensional aggregates found for both samples appear smaller

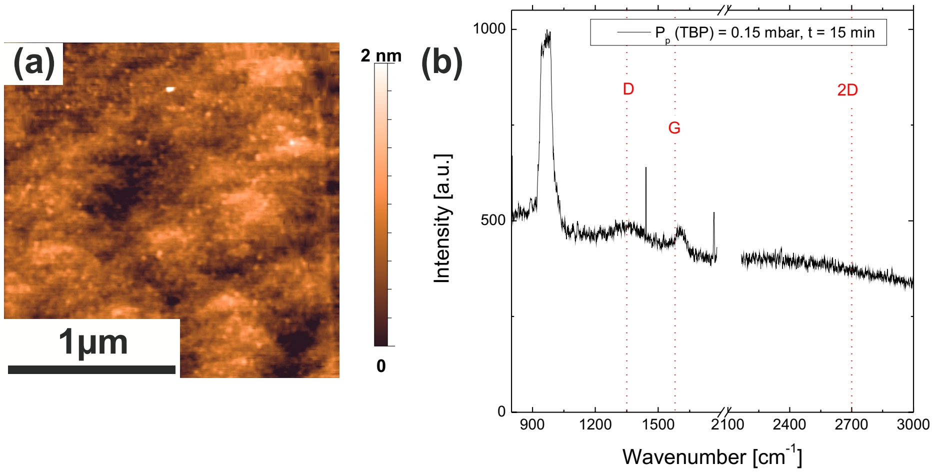

Figure 4.31: AFM (a) and Raman (b) measurements of an approximately 50 nm thick GaP layer which was grown on Si (001) and annealed at 800 °C supplying TBP.

here than in image 4.29 (d). This, however, might merely be an effect of the AFM tip, which might have a smaller dimension here than in fig 4.29 (d), leading to only seemingly smaller structures here, as the AFM measurement always displays a convolution of the sample surface and the structure of the AFM tip. Nevertheless, as no significant changes occur, this treatment is expected to have a similar effect on a GaP layer on Si (001) as on GaP (001). Under this assumption, the SIMS measurement presented in fig. 4.30 can be associated with the Raman spectrum shown here. Several assignable features appear in the Raman measurement. The first is the most prominent peak at around 960 cm^{-1}, originating from multi-phonon scattering processes in the Si substrate [98]. Additionally, the Raman spectrum exhibits two peaks at around 1350 cm^{-1} and 1600 cm^{-1}. The three red dotted lines in the diagram display the approximate wavenumber range where graphene-induced Raman bands are expected. The rather broad peak at approximately 1350 cm^{-1} is located in the region of the so-called D band, while the second peak at 1600 cm^{-1} is in the region of the so-called G band [23]. This clearly indicates that C_6-ring structures were deposited, as these bands origin from C_6-ring breathing and stretching respectively. However, no peak was detected in the region of the so-called 2D band, originating from the second order of zone-boundary phonons. This peak, though, is always the most prominent peak observed in pure graphene samples [23]. Two explanations for the absence of this peak can be given. Presumably, no long-range ordered graphene, but rather some small scale graphene units were deposited by the TBP treatment. Additionally, the observed red shift of the G peak from the expected position at 1585 cm^{-1} to 1600 cm^{-1} indicates a doping of the deposited C material [26]. This is not surprising, as the C deposition arose from supplying TBP at high temperatures. It has to be assumed that P atoms have been incorporated into the C structures, which leads to a n-type doping. Such doping would also result in a decreased intensity of the 2D band. In addition to the absence of a long-range ordering of the C_6-ring structures, this might also be a reason that the 2D band can not be detected. A further, very narrow peak is positioned at approximately $1765\,\mathrm{cm}^{-1}$. While the exact origin of this peak, probably referring to C-O bonds, is not yet known, it was found for all substrates and sample treatments studied. Hence, no information about the influence of the sample treatment on the composition of the sample is gained from this peak. Additionally, in the spectrum, as well as in other following spectra, a very sharp peak appears at around $1440\,\mathrm{cm}^{-1}$. This peak, though is a measurement artifact. Very pronounced, sharp peaks are generated in the Raman spectrum, if cosmic rays hit the detector, which occurs commonly for long measurements as performed here. To remove these artifacts from the spectrum, generally two Raman spectra are recorded successively in the same spectral region and the minimum of both measurements is chosen for the combined spectrum. Coincidentally, for both measurements combined in fig. 4.31 sharp peaks appear at approximately $1440\,\mathrm{cm}^{-1}$, resulting in the sharp peak observed here. Since C deposition on GaP is possible from a high-temperature treatment supplying TBP, further experiments were performed to analyze whether graphene growth is even achievable by this method. These experiments will be discussed in section 4.6.2 on the deposition of C on GaP.

It was found that high-temperature treatment in H_2 at a reactor pressure of 50 mbar does not influence the GaP surface to a great extent for temperatures up to 800 °C, as illustrated in image 4.29. For Si the reactor pressure applied during the annealing has a major influence on the surface structure generated [81]. Since this might also be true for GaP, a unstabilized annealing at a high reactor pressure of 950 mbar was performed. On the one hand, this was done to analyze the influence of an increased reactor pressure on the GaP substrate at high temperatures, as a variation of the reactor pressure might also be performed for C deposition. On the other hand, incongruent evaporation possibly occurring during this treatment could be utilized to generate pure metallic Ga droplets on the GaP surface.

AFM images for two samples annealed at 675 °C in H_2 atmosphere and at a reactor pressure of 950 mbar are shown in fig. 4.32. Image (a) illustrates a sample annealed for 15 min. The annealing time was increased to 30 min for the sample presented in images (b) and (c), showing the same sample recorded for two different scan areas. Atomic steps are still observable for both samples after this treatment, but a clear change in the structure of the surface is visible. Rather than large surface terraces with smooth step edges, as observed in the high-temperature treatment at a low reactor pressure, small terraces with frayed edges developed, especially for the sample shown in (a). For an annealing time of 30 min, large circular structures emerge on the GaP surface, as can be seen in image (c). The height profile of one of these structures (d), taken at the position of the red

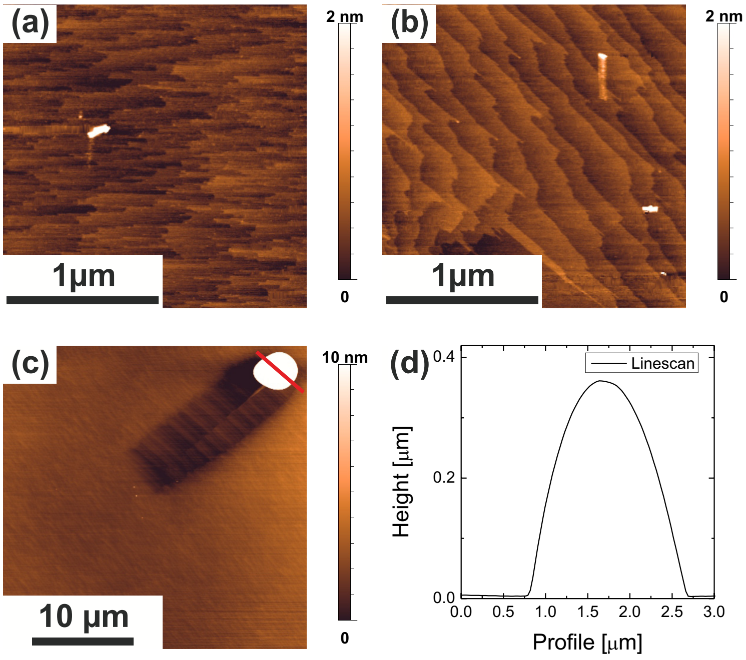

Figure 4.32: AFM images of GaP substrates after annealing at 675 °C in H_2 at a reactor pressure of 950 mbar for 15 min (a) and 30 min (b) and (c). A height profile taken in (c) at the position of the red line is displayed in (d).

line in image (c), reveals that this structure holds a considerable maximum height of approximately 360 nm and a diameter of almost 2 µm.

To analyze the composition of these structures, EDX was performed on the sample shown in fig. 4.32 (b) and (c) after annealing for 30 min at 675 °C applying a reactor pressure of 950 mbar. Due to the relatively large dimension of these structures, this was done in combination with SEM, providing a sufficient resolution here. A SEM image (a), two EDX point spectra (b) recorded at the two points marked in (a), and an EDX map showing a filtered image of the Ga and P signal as well as the secondary electrons detected are shown in fig. 4.33. The SEM image again reveals large circular structures, as already found by AFM in fig. 4.32 (c). Even structures appear with a considerably larger diameter than 2µm, which was determined in fig. 4.32 (d). As illustrated in (a), the EDX spectrum in (b) marked as 17794_1 and displayed in blue, was taken at one of these large structures, while the spectrum marked as 17794_2 and pictured in red was taken at some distance from it on the seemingly flat GaP surface. Besides the constantly present C signal originating for the C $K_{\alpha 1}$ line, the spectrum recorded at the circular structure only shows one additional peak which can be assigned to the Ga $L_{\alpha 1}$ line. The spectrum taken at the flat surface exhibits a lower count rate for the Ga signal but additionally shows a P peak at the P $K_{\alpha 1}$ line. It is therefore assumed that the flat surface consists of GaP, which is, judging from the AFM images in fig. 4.32 (b), rather intact, while the large circular structures are composed of metallic Ga. This assumption is also verified by the

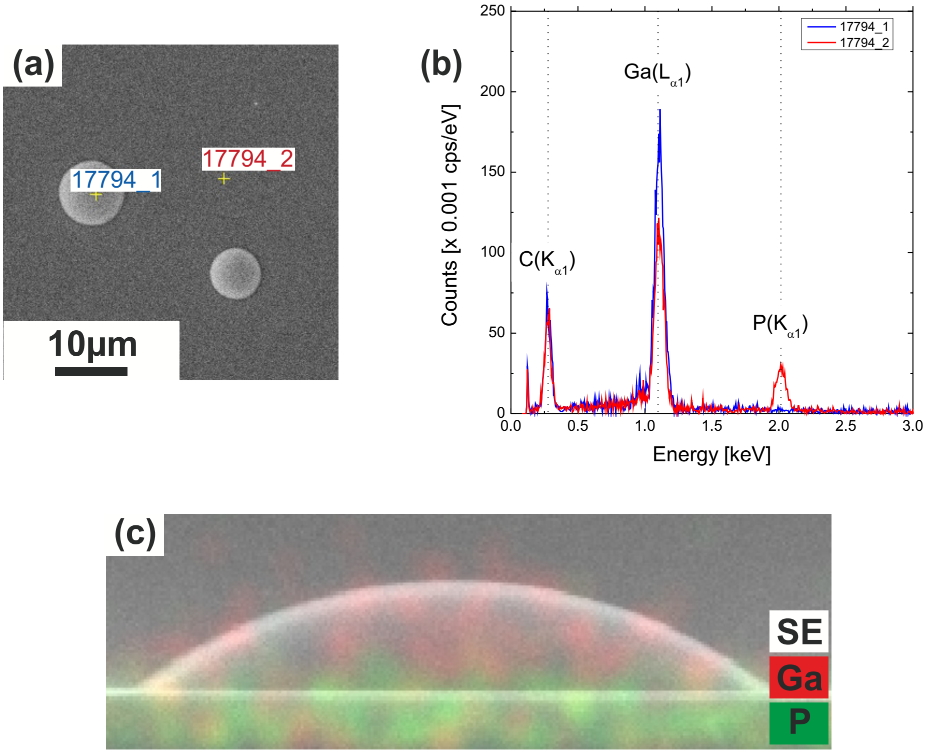

Figure 4.33: SEM (a) and EDX (b) and (c) measurements of the surface of a GaP (001) substrate after annealing for 30 min at 675 °C in H_2 at a reactor pressure of 950 mbar, as shown in figure 4.32. The two EDX point spectra presented in (b), were taken at the spots marked in (a). The EDX map (c) shows the Ga (red), P (green) and SE (white) signals.

EDX map presented in (c) displaying a filtered map of the signal detected for the Ga $L_{\alpha1}$ and the P $K_{\alpha1}$ lines. The SE signal, displayed in white, reveals that the map was recorded at one of these structures and visualizes that the structure is build up by pure Ga. These large droplets presumably form due to the incongruent evaporation of P during annealing, resulting in metallic Ga remaining on the surface. Since Ga is highly mobile on the surface at the applied annealing temperature, it converges, forming relatively large structures. This result indicates that the incongruent evaporation is actually enhanced by the usage of a high reactor pressure, as even at a temperature of 800 °C no formation of Ga droplets was observed for an annealing applying a reactor pressure of 50 mbar. This might be due to an enhanced formation of phosphine (PH_3) by P surface atoms with atomic H, as more atomic H is available for a high H_2 reactor pressure. The PH_3 can subsequently desorb from the GaP surface. As mentioned above, this might be used for the formation of Ga droplets on GaP, but for a high-temperature deposition of C on GaP this effect also has to be taken into consideration.

4.4 Gallium phosphide deposition on silicon

The growth of high-quality GaP on Si (001) substrate has been investigated in a number of studies [80],[99], [81],[82], [100]. It was found that for the GaP nucleation on Si, a rather low growth temperature and flow rate modulated epitaxy (FME), i.e., a successive deposition of TPB and TEGa for 1 s each separated by a growth interruption of 1 s, are crucial to achieve a good quality crystal and especially interface. Additionally, those investigations reveal the necessity of a TBP preflow for the growth of smooth GaP to Si interfaces [81]. However, the first steps of the nucleation process are not yet fully understood. Therefore, the deposition of the first layers of Ga and P were studied and will be discussed in the following section. Firstly, the influence of the TBP preflow is shown for the deposition of TEGa on Si.

Two samples deposited with similar growth conditions, but differing in the TBP preflow, are presented in fig. 4.34 by means of AFM and HAADF STEM measurement.

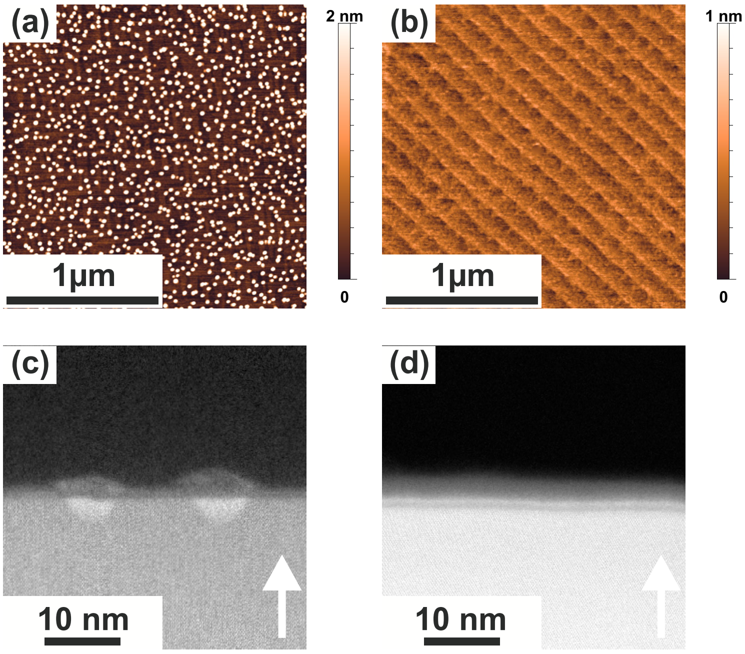

Figure 4.34: AFM and cross-sectional HAADF STEM measurements of a Si (001) surface after TEGa deposition at 450 °C without (a) and (c) respectively, and with a TBP preflow of 10 s (b) and (d), using otherwise equivalent growth conditions.

An AFM or a STEM measurement of a Si (001) sample treated with approximately 2.1 MLs of TEGa at 450 °C, as discussed before in section 4.2.1, are displayed in images (a) and (c). After a deposition of only TEGa, aggregates form on the surface (a) and pyramidal structures containing Ga occur in the Si (c), as already described in section 4.2.1. For the sample displayed on the right, initially TBP was deposited for 10 s at 450 °C followed by a 1 s growth interruption and the deposition of the same amount of TEGa as used for the sample (a). Adapted from the optimized GaP nucleation process on Si (001), the TBP partial pressure was set to 0.94 mbar, hence, a TBP to TEGa ratio of 177 was applied. This was done to compensate for the low decomposition rate of TBP at the chosen growth temperature and to ensure a full P or TBP coverage of the Si substrate prior to the TEGa deposition. The surface appears flat without three-dimensional aggregates and the Si surface structure is still clearly distinguishable after this treatment (b). The STEM micrograph reveals no structures formed in the Si crystal. Rather, a film covers the surface, exhibiting various layers with different contrasts (d). The measurement displays a surface coverage of several molecular layers on the Si. Also, no crystalline GaP layer was found to evolve after a first deposition of TBP and TEGa. Noticeably, the thickness of the layer is about 3.5 nm. Only approximately 2 MLs of TEGa were deposited, which would lead to a growth of only 2 MLs of GaP. However, a significantly larger amount of TBP was deposited during the preflow and it must be assumed that P or undecomposed TBP was adsorbed on the Si surface at that time. Ga, having a larger atomic number than P, shows a brighter contrasts in a STEM micrograph. The bright intermediate layer in the film might be explained by Ga diffusing into the TBP or P layer and forming a layer close to the Si surface. The fact that this layer structure is still visible after exposure to air as well as TEM sample preparation indicates that it is relatively stable. However caution is necessary for the interpretation of these results, as samples are handled in air during the TEM sample preparation. A native oxide layer therefore forms on all samples and can be seen by STEM. Among other things, the thickness of this layer strongly depends on the composition of the sample. Si, however, was found to have an oxide layer thickness of less than one nanometer after exposing the samples to air for several days [101]. Additionally, no amorphous layer was observed for other Si samples, which shows such an extended thickness or layers with various contrasts.

Despite this, after several further cycles of pulsed TBP and TEGa deposition using identical conditions, a high quality crystalline GaP layer and a smooth GaP to Si interface develops. Only the TBP deposition time was decreased from 10 s, as used for the preflow, to 1 s for this growth. The GaP growth is displayed in fig. 4.35, showing STEM micrographs of samples after 4 (a) or 8 cycles (b) of TBP and TEGa deposition by FME.

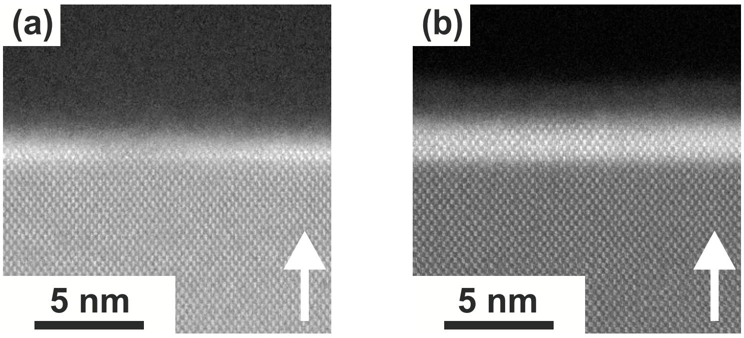

Figure 4.35: Cross-sectional HAADF STEM measurements of Si (001) after 4 (a) or 8 (b) cycles of GaP nucleation by FME

Both images clearly show a thin GaP layer on Si, that's thickness increases with rising number of deposition cycles. While an additional layer can be detected at the surface of the GaP layer, too, no such layer appears at the GaP to Si interface. Therefore, it is assumed that the GaP growth process occurring resembles an atomic layer epitaxy (ALE) type of growth. The Si surface might initially be covered by undecomposed TBP after the TBP preflow. This assumption is based on quantum chemical studies revealing significant energy barriers for the gas phase decomposition of TBP [102]. The precursor is not expected to decompose to a great extent in the gas phase without the presence of, for example, TEGa or a similar compound at the chosen growth temperature. After TEGa deposition some Ga or TEGa might also reach the growth surface and diffuse through the TBP layer reaching the Si surface. Decomposition of the TBP and crystal growth might only start for a sufficient amount of Ga or TEGa near the growth surface.

To gain a better understanding of the influence of a TBP preflow, this growth process was also studied for the deposition of TMGa. However, other than for TEGa, the presence of TMGa is not expected to enhance but rather suppress the pyrolysis of TBP at low temperatures [12]. This is due to the differences in the decomposition pathways of TEGa and TMGa and the differing residual alkyl-groups. No GaP crystal growth is therefore expected when TMGa is used. AFM images of Si (001) surfaces are presented in figure 4.36 after a deposition of TMGa for 10 s without (a) and with (b) TBP preflow, employing a Ga partial pressure of 0.4 mbar.

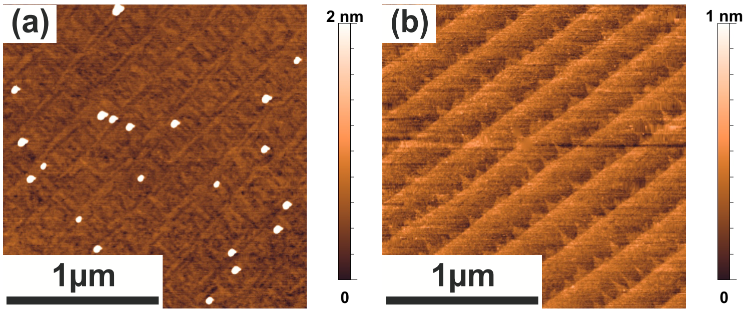

Figure 4.36: AFM images of a Si (001) surface after TMGa deposition at 450 °C without (a) or with a TBP preflow (b) of 10 s, and otherwise equivalent growth conditions.

Only TMGa was deposited for the sample shown in the micrograph (a). The same growth conditions but an additional supply of TBP for 10 s prior to the TMGa offer was applied for the preparation of the sample (b). A deposition of TMGa at the chosen growth conditions leads to a formation of mounds containing Ga on the Si surface (a), as already discussed in section 4.2.2. Although no considerable decomposition of TBP is expected, a TBP preflow results in a flat surface, which clearly exhibits the Si surface structure (b). This is consistent with the results observed in fig. 4.34 for TEGa deposition. When no significant amount of P is present at the chosen growth conditions, as presumably no pyrolysis of TBP proceeds, it has to be assumed that the Si (001) surface is covered by a molecular layer of TBP after the preflow rather than by P. This layer might then hinder the deposition of Ga from TMGa.

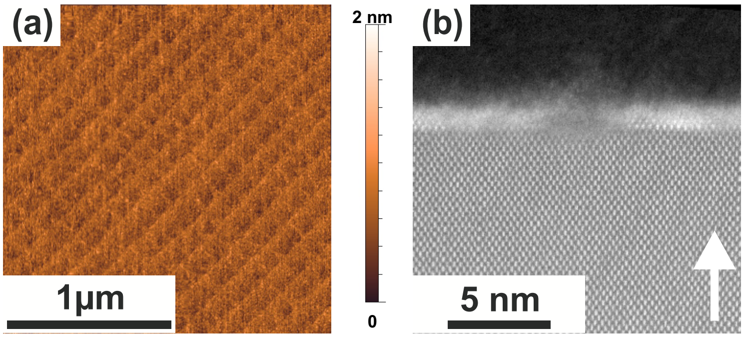

Figure 4.37: AFM (a) and cross-sectional HAADF STEM (b) measurements of a Si (001) surface after 9 cycles of a FME deposition of TBP ($P_P = 0.94$ mbar) and TMGa ($P_P = 1$ mbar) at 450 °C for 10 s each per cycle starting with TBP deposition.

To clarify whether this hindrance can only be observed for the first cycle of the GaP nucleation, similar to what was found for TEGa, or whether a growth of GaP with TMGa is possible at 450 °C, 9 FME cycles of GaP were deposited on Si (001). To compensate for the suppressed pyrolysis, an increased amount of TBP was supplied compared to the GaP growth using TEGa. Again a TBP partial pressure of 0.94 mbar, but an increased growth time of 10 s per cycle was used. It was observed that a significantly lower amount of TMGa is deposited in combination with a TBP offer in comparison with a deposition of merely TMGa. Therefore, the growth time for TMGa was also increased to 10 s per cycle, using a TMGa partial pressure of 1 mbar. An AFM (a) and a STEM (b) micrograph of a Si (001) surface after the described treatment are presented in fig. 4.37. The AFM measurement reveals a flat surface; the Si (001) surface structure is still recognizable but slightly blurred after the deposition. However, no Ga droplets appear. The STEM image reveals the surface to be covered with an approximately 2 nm thick layer with a brighter contrast than Si after the deposition of TBP and TMGa. It exhibits a crystalline structure only in some areas and is amorphous in others. While a huge amount of precursors was offered during this deposition, the measurement exhibits barely any crystalline GaP growth. This confirms the hypothesis of TBP not decomposing under the chosen growth conditions. However, also the supplied TMGa, which would form a vast amount of Ga-containing aggregates for a deposition without TBP, was not deposited on the Si (001) surface, as can be seen in the AFM as well as the STEM measurement. As stated before, the TBP surface coverage presumably hinders an adsorption of Ga from TMGa. As TMGa or it's residuals can not catalytically decompose TBP covering the surface, no significant GaP growth occurs and the excess Ga, TMGa and TBP desorbs. These results suggest that TBP molecules physically or chemically adsorbs on the Si (001) surface during the TBP preflow. In the presence of a sufficient amount of TEGa TBP catalytically decomposes, while this is not the case for TMGa. For the most part, the deposition of TMGa on the TBP covered Si might therefore be hindered. To investigate this deposition of TBP on Si (001) further, STM measurements were performed for similarly prepared samples, however, no Ga precursor was offered.

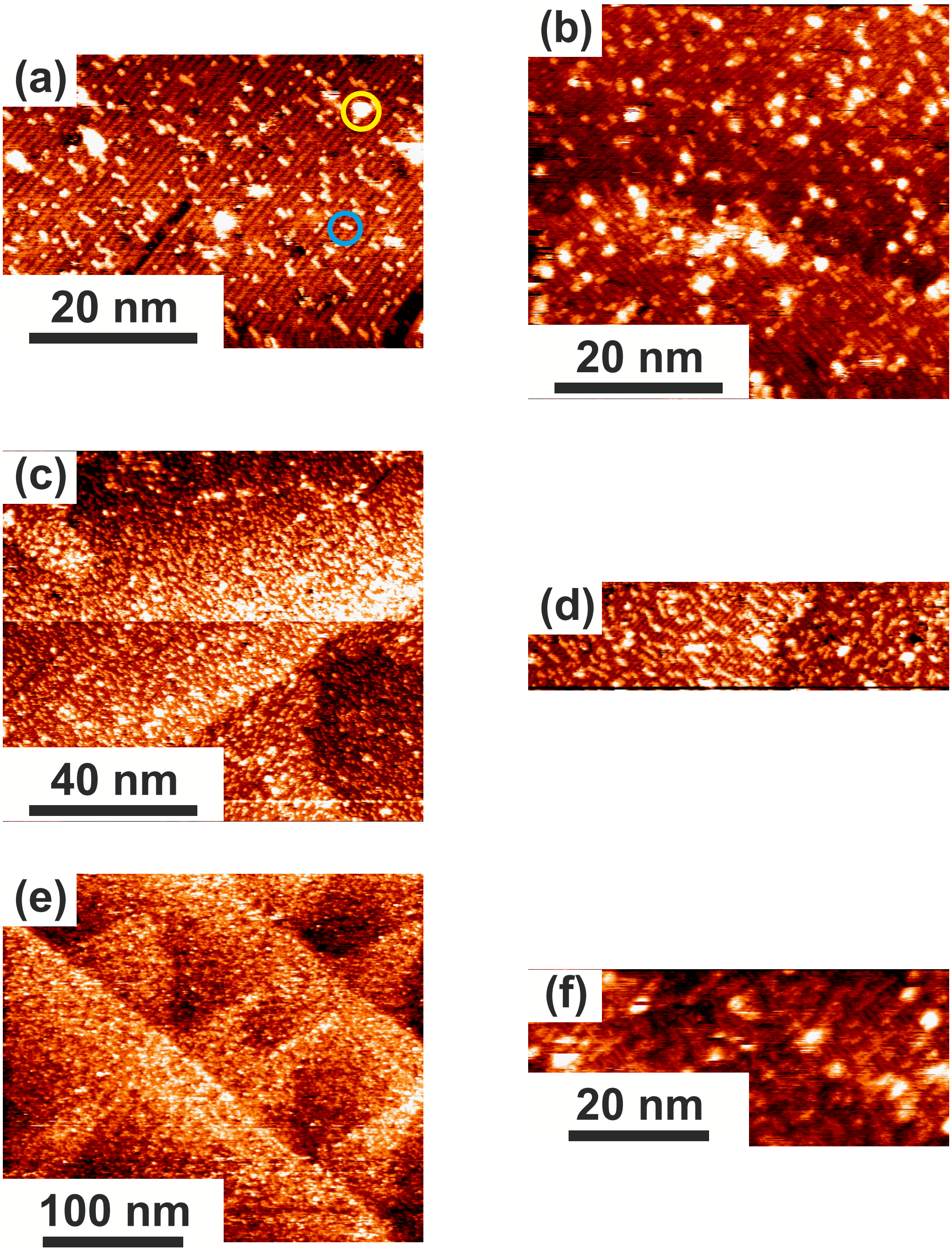

Figure 4.38: STM images of Si surfaces with different TPB coverages; for all samples TBP was deposited for 1 s at 450 °C on a Si buffer as shown in fig. 4.2. The partial pressure of the P precursor was tripled from 0.31 mbar (a) and (b) (bias voltage: -1.93 V; tunnelling current: 0.5 nA; for both) to 0.94 mbar (c) and (d) (bias voltage: -2.0 V; tunnelling current: 0.5 nA; for both) and increased again by a factor of 1.5 to 1.41 mbar (e) and (f) (bias voltage: -1.93 V; tunnelling current: 0.5 nA; for both).

Therefore, initially a Si buffer was prepared as described in section 4.1. TBP was supplied subsequently at 450 °C for 1 s, using different TBP partial pressures. STM micrographs of these samples are presented in fig. 4.38. A TBP partial pressure of 0.94 mbar, as previously used for the preflow, was applied for the images (c) and (d). Thus, the amount of TBP offered corresponds to 10 % of the amount offered as a preflow for the samples presented previously in this section, since a deposition time of 1 s rather then 10 s was used.
To analyze the influence of the TBP deposition extensively, the TPB partial pressure was decreased by a factor of 3 to 0.31 mbar for the sample shown in (a) and (b). It was also increased by a factor of 1.5 to 1.41 mbar for the preparation of the samples displayed in the micrographs (e) and (f). By this, the highest amount of TBP offered corresponds to only 15 % of the amount used as preflow earlier. Samples with a greater supply of TBP were prepared, however, no distinct STM measurements were achieved for these. This might be due to a growing amount of only loosely bound molecules on the Si surface with increasing TBP offer. These molecules might at least partly accumulate at the STM tip during the scanning process, which makes a well resolved measurement impossible.
The Si surface structure can clearly be observed for all samples presented, showing D_A and S_B Si-steps as discussed in section 4.1. In comparison to the pure Si buffer (fig. 4.2), additional molecular structures, which have about the width of a Si dimer rows, appear on the surface after TBP deposition. Exemplary, one of these structures is highlighted by a blue circle in fig. 4.38 (a). Furthermore, significantly larger formations, circled exemplary in yellow, were observed. Similar structures were already seen for the Si buffer without TBP supply. Also, no clear correlation was found between their quantity and the TBP partial pressure. H vacancies or impurity atom might lead to these structures, appearing considerably larger than the Si dimers, due to their electronic structure.
The surface coverage, however, grows with increasing TBP partial pressure for the smaller formations, with Si dimer row width (highlighted in blue in fig. 4.38 (a)). The proportional coverage of the Si surface with these structures was determined in dependency of the TBP partial pressure. For this evaluation two sufficiently well resolved image sections of the STM micrographs, such as shown in fig. 4.38, were used each for the sample prepared with a TBP partial pressure of 0.31 mbar and of 0.94 mbar. It was assumed, that the number of dimers which are occupied corresponds to the length of the features on the surface with respect to the Si dimer rows. A Si lattice constant of 5,43 Å and therefore a spacing of 7,68 Å between the centers of neighbouring dimers was assumed.

The proportional surface coverage plotted against the TBP partial pressure is presented in fig. 4.39 (a). A surface coverage of approximately 14% was found for a TBP partial pressure of 0.31 mbar and of approximately 25% for a TBP partial pressure of 0.94 mbar. This is in good agreement with results from the TEGa deposition on Si (001) utilizing different deposition times for the TBP preflow. AFM micrographs for these samples are presented in fig. 4.39 (b) and (c). For these samples, a Si buffer was grown as described

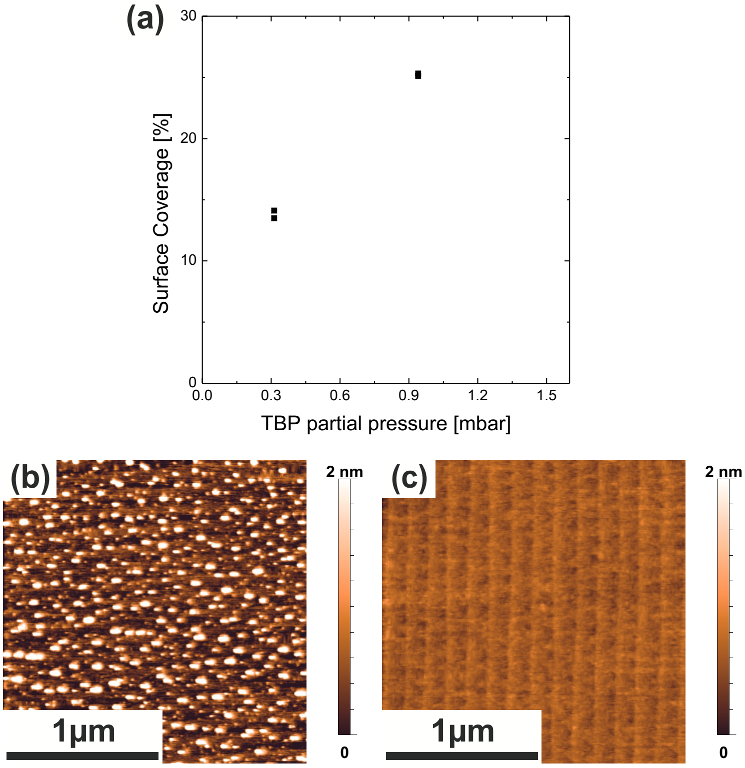

Figure 4.39: Evaluation of the surface coverage in dependency of the TBP partial pressure (a) for the samples presented in fig. 4.38. AFM micrographs of Si (001) after 1 s of TEGa deposition at 450 °C with a TBP preflow of 1 s (b) and 5 s (c) respectively using a TBP partial pressure of 0.94 mbar.

in section 4.1. TBP was supplied subsequently at 450 °C using a partial pressure of 0.94 mbar. A TBP deposition time of 1 s and of 5 s was tested. This corresponds to one or five times the amount of TBP supplied for the samples investigated by STM, using a TBP partial pressure of 0.94 mbar (fig. 4.38 (c) and (d)), as a deposition time of 1 s was utilized for these. Following, TEGa was deposited for 1 s at 450 °C using a partial pressure of 5.31×10^{-3} mbar, which corresponds to approximately 1 ML of Ga. Aggregates containing Ga appear on the sample after using only 1 s of TBP preflow. Since not the complete Si surface, but only 25% of it, were covered due to the TBP preflow no sufficient protective layer of TBP or P is present after 1 s of TBP preflow. If a linear increase of the proportional surface coverage with rising deposition time is assumed, a complete surface coverage would be reached after a TBP preflow of 4 s. This is in good agreement with the measurement shown in image 4.39 (c). No structures containing Ga form on the surface after a TBP preflow of 5 s, indicating that a complete TBP or P surface coverage was achieved.

Whether the small structures found by STM measurement (highlighted in blue in fig. 4.38 (a)) are formed by TBP or by P can not be clarified by this method. As mentioned previously, though, TBP is not expected to thermally decompose to a great extent at

450 °C for the chosen growth conditions [102]. The formations remained stable throughout the STM measurement and did not move due to the scanning of the surface with the STM tip. Based on this observation, it is assumed that these molecules are chemically and not just physically adsorbed on the Si. Other than for the TEGa deposition (fig. 4.16), no preferential ordering of the molecules along the S_B step edges is observed. Nevertheless, all samples indicate that the surface coverage is not arranged in a merely statistical order. Rather, the deposited molecules order in rows perpendicular to the Si dimer rows. This behaviour is observed on the A as well as B type terraces. The STM micrograph presented in fig. 4.40, which shows an enlarged section of image 4.38 (a), takes a closer look at these ordered formations.

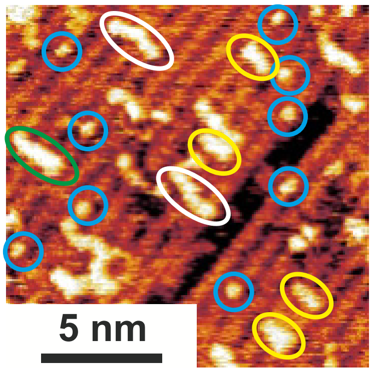

Figure 4.40: Enlarged section of the STM micrograph shown in fig. 4.38 (a), displaying a Si (001) surface after TBP deposition at 450 °C using a growth time of 1 s and a partial pressure of 0.31 mbar. Some particular features are highlighted. Single molecules covering one Si dimer row are circled in blue, formations adsorbed on two dimer rows in yellow and those stretching across three rows in green. Two longer, but kinked structures are marked by white circles.

Mostly single molecules, which are positioned on top of one Si dimer row, appear for the lowest TBP pressure used of 0.31 mbar. Some of these are marked exemplarily by blue circles in fig. 4.40. In addition to that also longer rows form. Yellow circles highlight features, which are stretched across 2 dimer rows, and the green ellipse marks a structure placed above three dimer rows. Since these features resemble straight lines, which are arranged perpendicular to the Si dimer rows, they are presumably formed by two or three molecules, which are positioned on two or three neighbouring Si dimers. Furthermore elongated, kinked structures, circled exemplarily in white, appear. These might consist of several shorter rows, which formed in close proximity to each other, not on neighbouring Si dimers, but slightly shifted. A detailed analysis of the length of these rows in dependency of the supplied TBP partial pressure is displayed in fig. 4.41. Therefore, the kinked structures (marked in white in fig. 4.40), were treated as separate short structures, for example, as two features stretching across two dimer rows each for the highlighted structure in the upper part of the image, rather than as long ones.

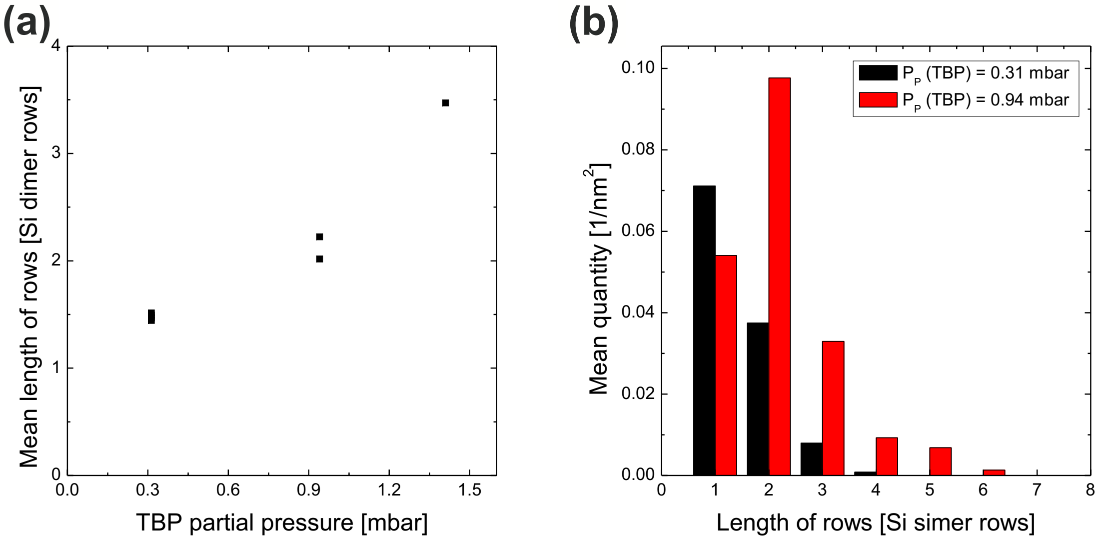

Figure 4.41: Evaluation of the influence of the TBP partial pressure on the length of structures, which result from the TBP deposition. The mean length of the forming rows in dependency of the TBP partial pressure is shown in (a). The number of rows per nm^2 found for each particular row length for two different TBP partial pressures is compared in (b). STM micrographs, such as shown in fig. 4.38 where analyzed.

The diagrams show the influence of the TBP partial pressure on the mean length of the observed rows in relation to the Si dimer rows (a) and the quantity of each particular row length normalized to 1 nm^2 for the two lower TBP partial pressures used, i.e., for 0.31 mbar and for 0.94 mbar (b). All sufficiently well resolved measurements available for each sample were evaluated for this analysis. This means that four different measurements, recorded on various positions on the sample, were included for the lowest TBP partial pressure of 0.31 mbar, two for the sample prepared with a TBP partial pressure of 0.94 mbar and only one for a TBP partial pressure of 1.41 mbar. Additionally, only an inferior resolution was achieved for the sample prepared with the highest TBP partial pressure, probably due to molecules accumulating at the STM tip. Therefore, the data point given in (a) must be treated with great caution as not enough data was available for a reliable analysis. For this reason this sample was also excluded from diagram (b). However, a clear trend of a growing mean length of the rows with increasing TBP partial pressure can be observed in (a). Diagram (b) additionally illustrates, that mostly single molecules were found on the sample with the lowest TBP partial pressure and the row length does not exceed four Si dimer rows. In comparison, the larger TBP partial pressure leads to an increased formation of longer rows, with length up to 6 Si dimer rows. The quantity of structures is maximum for a row length of 2 Si dimer rows. Density functional theory (DFT) calculations were performed, to clarify the atomic processes leading to this preferential formation of molecular rows perpendicular to the Si dimer rows [103]. First the adsorbate configuration for TBP on a hydrogen passivated Si (001) surface was studied. However, no minimum in energy was found for an adsorption of TBP on neighbouring Si dimers perpendicular to the Si dimer rows. The formation of the molecular rows found in experiment can therefore not be explained by reasons of adsorption energy.

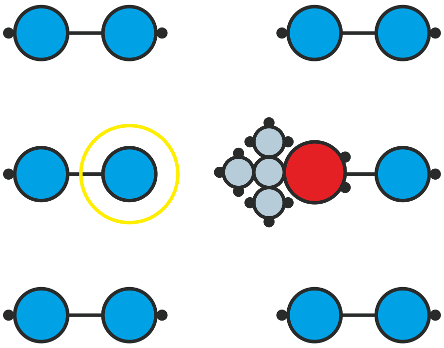

Figure 4.42: Scheme of a stable H vacancy (highlighted by yellow circle) neighbouring a TBP adsorbate (red) on H passivated Si (001) (blue); adapted from [103].

An explanation for the preferential formation of these particular structures, is the generation of hydrogen vacancies on the Si surface, which might induce this effect. It was found, that hydrogen vacancies, which are created on the passivated surface, can be locally stabilized at the neighbouring surface sites of a TBP adsorbate. The DFT calculations identified the nearest neighbour dimer of the TBP adsorbate in the adjacent dimer row as the energetically most favorable site for H vacancy stabilization. This site is depicted in image 4.42, presenting the Si atoms or dimers in blue, the TBP molecule as red structure and the H vacancy highlighted by a yellow circle. H vacancies are expected to exist on the Si surface, which was used for TBP deposition, since only molecular H_2 is provided in the growth reactor at the deposition temperature of 450 °C. Furthermore a H vacancy is a preferred adsorption site for TBP on a hydrogen passivated Si (001) surface. This result could explain the preferential adsorption of TBP on neighbouring dimers in different dimer rows.

4.5 Gallium deposition on gallium phosphide

As mentioned in the beginning of the previous section, a thin GaP layer should be used as an interlayer for the deposition of Ga on Si (001) to prevent an intermixing of those. In section 4.2, results on the Ga deposition on Si (001) and on the influence of several growth parameters thereon were presented. The growth conditions applied for this material system have to be adjusted for the deposition of Ga on GaP.

As a starting point, TEGa or TMGa were deposited on a thin GaP layer applying the same growth conditions as used for the Ga deposition on Si. AFM images of a Si (001) surface and the surface of a GaP layer on Si (001) after the deposition of TEGa

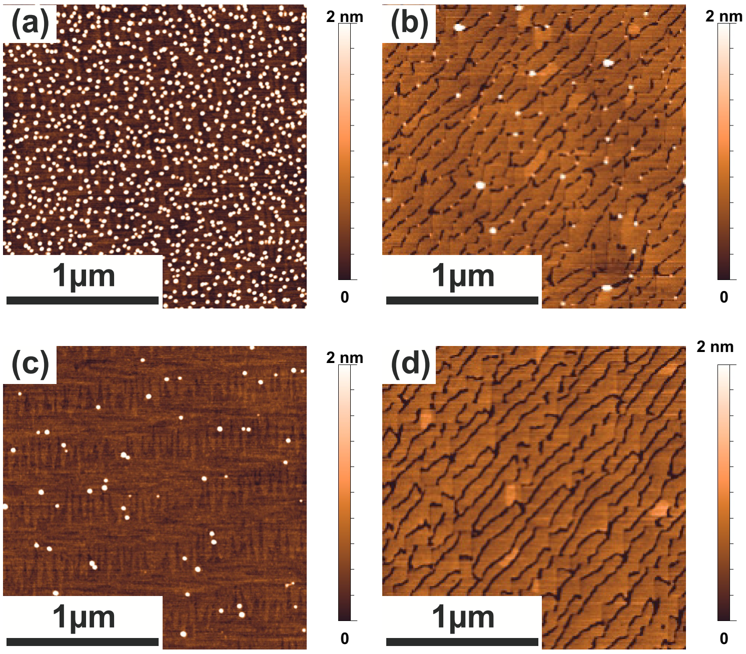

Figure 4.43: AFM images of samples after a deposition of TEGa on Si (001) (a) or on a thin GaP layer on Si (001) (b) and after a deposition of TMGa again on Si (001) (c) or a thin GaP layer on Si (001) (d). Ga was deposited for 1 s at 450 °C for all samples.

or TMGa are displayed in fig. 4.43. The growth conditions for the Ga deposition on Si and on GaP were chosen equivalently. However, for the deposition of TEGa and of TMGa different growth conditions were applied due to the different decomposition rates for both precursors. For the deposition on the GaP interlayer, initially an approximately 3 nm thick GaP layer was grown. After a growth interruption of 60 s, Ga was deposited on this layer. A Ga growth temperature of 450 °C was chosen for all samples. The Ga partial pressure multiplied by the deposition time was set to approximately 0.011 mbar×s for the deposition of TEGa and to 1 mbar×s for TMGa. But, although the amount of Ga precursor used for the deposition on Si, and on the GaP interlayer was equivalent for the corresponding samples, the quantity of aggregates formed on GaP is considerably smaller than that formed on Si for either precursor. This is presumably due to TBP, which remained in the reactor or on the sample surface despite the growth interruption, resulting in the growth of additional GaP rather than Ga aggregates. To compensate for this, the Ga deposition time was extended for the samples presented in the following.

A comparison of the deposition of TEGa on Si (001) and on GaP (001), by means of AFM measurements, is displayed in fig. 4.44. Comparable growth conditions were chosen for both samples. The Ga was deposited at a temperature of 450 °C and a partial pressure of 7.6×10^{-3} mbar, corresponding to a deposition of approximately 1.4 MLs per second, judging from GaP growth on Si (001). A growth time of 1 s was used for the deposition on Si (001) (a). The deposition time was increased to 4 s for the deposition on GaP (b), to

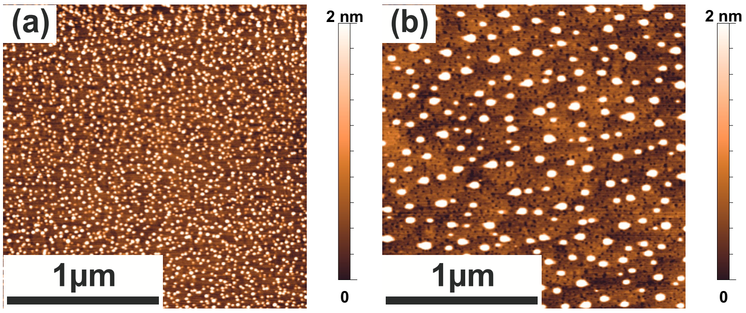

Figure 4.44: AFM images of TEGa deposited on Si (001) (a) and on GaP (001) (b) substrate at 450 °C.

compensate the effect shown in fig. 4.43. On both substrates mounds form. However, the structures on the GaP substrate (fig. 4.44 (b)) are clearly larger but exhibit a considerably lower density than those occurring on the Si substrate (a). The GaP substrate additionally shows holes after the Ga deposition, with a density similar to the density of the mounds on the Si substrate. It was assumed before that the deposited material is not mobile for the growth of TEGa on Si (001) at 450 °C, leading to the formation of a large number of small aggregates on this substrate. This appears to be different for the TEGa deposition on GaP (001). Judging from the voids detected in the GaP surface after the TEGa deposition, it is assumable that for the growth on GaP (001) initially small aggregates form, too, as on the Si (001) surface. The liquid Ga seemingly dissolves some crystalline material at the surface here; however, being mobile on GaP, the Ga structures merge at a sufficient temperature, provided at the beginning of the cool-down after growth. Hence, larger Ga aggregates emerge, and voids are left in the GaP (001) surface.

As GaP is only employed as an interlayer to separate the metallic Ga from the Si surface, it is desirable to keep this layer as thin as possible. To analyse the influence of the GaP layer's thickness on the characteristics of the structures forming, Ga was deposited on two different GaP layers with varying thicknesses. AFM images of those samples after TEGa deposition on an approximately 3 nm (a) and an approximately 22 nm (b) thick GaP layer on Si (001) are presented in fig. 4.45. Like for the previous samples, the TEGa deposition was performed at a growth temperature of 450 °C, but using a growth time of 4 s. For both samples mounds form after the Ga deposition, which are positioned at the GaP APBs breaking through the surface. This is in accordance with the earlier assumption stated in section 4.2.1 for the deposition of TEGa on Si, that the Ga aggregates form at defect sites on the surface. In addition to the mounds, voids appear in the GaP surface, as seen before in fig. 4.44. An evaluation of the number and size of mounds forming on the different GaP layers is given in fig. 4.45 (e). For this evaluation, two samples were used each for a 3 nm as well as for a 22 nm thick GaP layer grown with identical growth conditions. The diagram reveals that for a thick GaP layer a lower number of structures forms with an increased structure's size, in comparison to the structures occurring on a

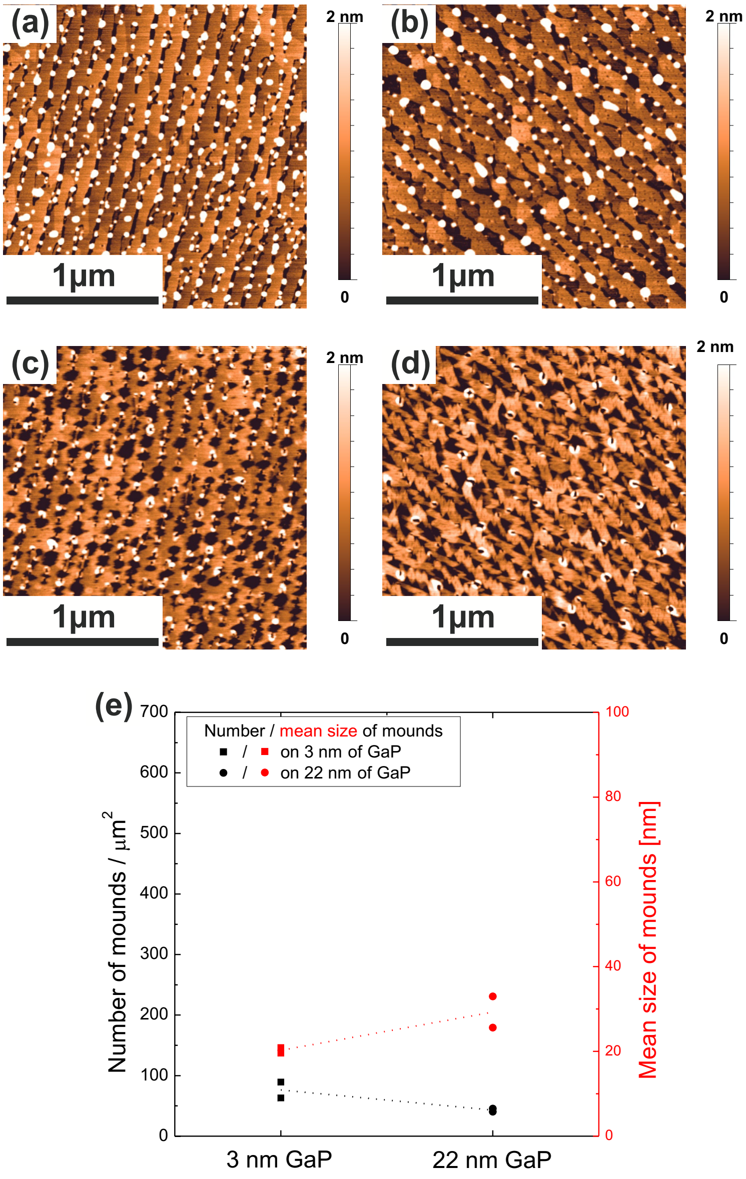

Figure 4.45: AFM micrographs of TEGa deposited for 4 s at 450 °C on an approximately 3 nm (a) and an approximately 22 nm (b) thick GaP layer on Si (001). AFM measurements of the same samples after etching for 1 s in 30% HCl (c) (corresponding to (a)) and (d) (corresponding to (b)). Evaluation (e) of the samples shown in (a) and (b) and of samples deposited under equivalent growth conditions.

thin GaP layer. AFM micrographs of the same samples after etching in 30% HCl for 1 s are displayed in fig. 4.45 (c) for a 3 nm GaP layer and in fig. 4.45 (d) for a 22 nm thick GaP layer. The images show that the Ga-containing structures can partly be removed by etching with hydrochloric acid leaving holes in the surface. However, especially for the sample where only a thin GaP layer was used (c), remains stay on the surface which are arranged circular around the holes resulted by etching. To analyse this behaviour and the difference in the structures forming for the different GaP layer thicknesses more closely, STEM was performed. Cross-sectional HAADF STEM images recorded at the as-grown samples are presented in fig. 4.46.

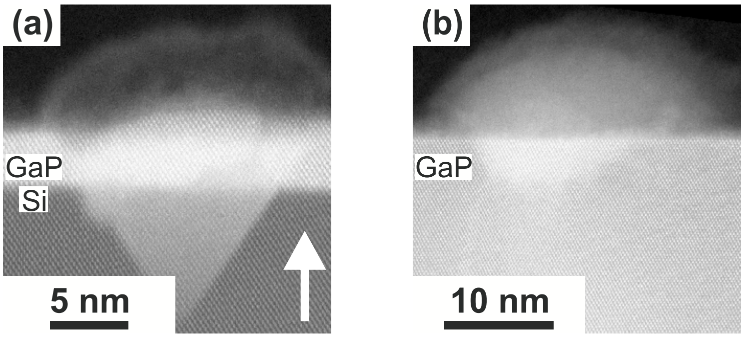

Figure 4.46: Cross-sectional HAADF STEM micrographs of TEGa deposited on an approximately 3 nm (a) and an approximately 22 nm thick (b) GaP layer on Si (001), as shown in the AFM images in fig. 4.45 (a) and (b).

The STEM measurements exhibit a significant difference between the two samples. For the thin GaP layer, shown in fig. 4.46 (a), Ga diffuses through the GaP layer, reaching the Si underneath and forming pyramidal structures bounded by the Si {111} lattice planes as on Si (001) (e.g. fig. 4.5). For the thicker GaP layer (b) the Si substrate is outside the image section displayed here; only the GaP layer is visible. For this sample, the Ga etches into the GaP similar to the structure in the thin GaP layer. However, the Ga does not diffuses as deep into the material. The structures forming here do not reach the Si substrate and are not limited by lattice planes but exhibit boundaries with a flatter angle. This difference between the two samples with different GaP layer thicknesses could explain the differences observed in fig. 4.45. Firstly, it was detected for the deposition of TEGa on Si (001) that the mobility of the liquid Ga on the Si surface seems hindered, and small aggregates formed. A contact between the deposited metallic Ga and the Si substrate might result in a similar effect. Therefore, on the thin GaP layer a larger number of smaller structures might form than on the thick GaP layer, as seen in fig. 4.45 (e). Secondly, the Ga structures reaching into the Si for the thin GaP layer might explain the remains found in fig. 4.45 (c) after etching in HCl, as this contact might lead to an intermixing of Si and Ga. As observed in section 4.2.3, such an intermixing might also lead to a formation of Si-containing structures above the Ga aggregate covering it.

Most of the structures containing Ga observed after TEGa deposition on the 3 nm thick GaP layer on Si (001) looked like the structure shown in fig. 4.46 (a). However, two particular structures found in this sample are displayed in fig. 4.47. Inside the pyramidal Ga-containing structure shown in image (a) numerous lattice defects can be recognized. Additionally the contrast in this area, being darker than the surrounding GaP, differs from the expected contrast for Ga diffused in GaP. This peculiar feature probably originates

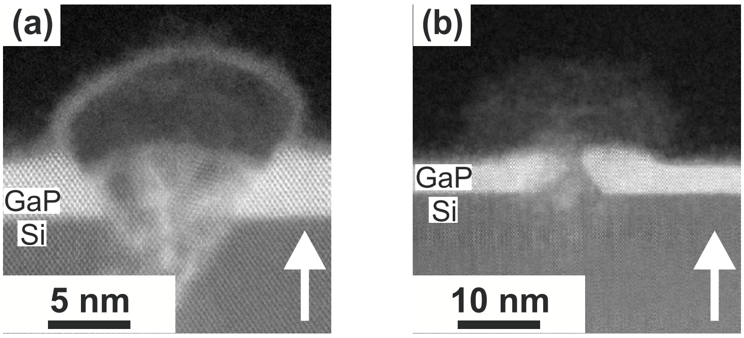

Figure 4.47: Cross-sectional HAADF STEM images of a sample after TEGa deposition on a 3 nm thick GaP layer on Si (001) as shown in fig. 4.45 (a) and 4.46 (a).

from an intermixing of GaP and Si during the Ga deposition. Similar to what was found in fig. 4.19 for the TMGa deposition on Si, it is assumed that GaP as well as Si dissolves in the liquid Ga at the growth temperature. Subsequently, due to a supersaturation of the Ga at lower temperatures during the cool-down, a new crystal structures forms exhibiting numerous lattice defects. This intermixing is also visible in image (b), showing a Si pyramidal structure formed in the GaP layer underneath a Ga aggregate. This pyramidal shape might originate from Si dissolving in Ga during the deposition and recrystallizing during the cooling of the sample. This particular pyramidal shape presumably results from the greater stability of the {111} interface between Si and GaP in comparison to the {001} or other low index interfaces [91], similar to the pyramidal shape of the Ga-containing structures in Si.

As the Ga-containing structures are supposed to be used as catalyst for the growth of ordered C structures, the influence of a high-temperature treatment after growth was studied, as in section 4.2.3 for the Ga deposited on Si (001). This analysis was performed since an intermixing of Ga, Si and GaP was already observed for the as-grown samples when a 3 nm thick GaP interlayer was used (fig. 4.47). For these samples, some amount of metallic Ga was still present at the surface (fig. 4.45 (c)). A loss of the metallic Ga at the surface, due to a possible further intermixing during the annealing, is expected to hinder the catalytic growth of C. Samples after TEGa deposition on a 3 nm and on a 22 nm thick GaP layer on Si (001), as shown after growth in fig. 4.45 (a) and (b), were annealed for 5 min at 500 °C in hydrogen atmosphere. AFM measurements of the annealed samples are shown in fig. 4.48 (a) for the 3 nm and (b) for the 22 nm thick GaP layer.

Judging from the AFM measurement, the structures containing Ga seem only slightly changed after annealing, compared to the as-grown samples shown in fig. 4.45. Due to the mobility of the liquid Ga at this temperature, a further merging of the Ga aggregates occurred during the annealing for the sample having a 22 nm thick GaP interlayer (fig. 4.48 (b)). This led to a decrease in the number of structures and an increase in their

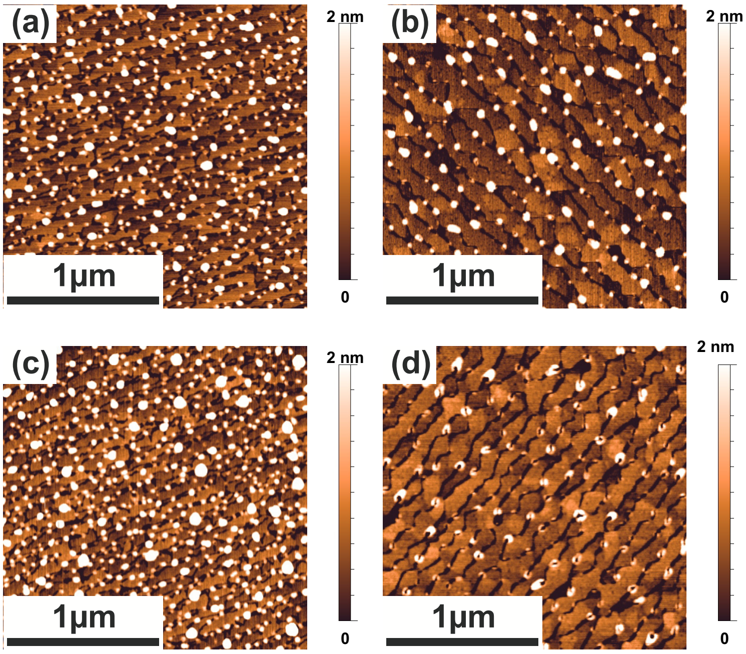

Figure 4.48: AFM images of TEGa deposited on an approximately 3 nm (a) and an approximately 22 nm thick (b) GaP layer on Si (001) after annealing (as-grown samples shown in fig. 4.45) and after additional etching for 1 s in 30% HCl (c) (corresponding to (a)) and (d) (corresponding to (b)) respectively.

size in comparison to the as-grown sample shown in fig. 4.45 (b). While the annealing seemingly effects the appearance of the structures only slightly, after etching only marginal changes can be detected for the sample where Ga was deposited on a thin GaP interlayer (c). The removal of the aggregates using HCl was at least partly possible for the as-grown sample, as shown in fig. 4.45 (c). It was detected before, for the as-grown samples, that an intermixing between Si and Ga occurs if the thickness of the GaP interlayer is chosen too small as the Ga diffuses through this interlayer, as can be clearly seen in fig. 4.47. A further intermixing presumably occurs at a sufficient temperature during the annealing. For the sample with a 22 nm thick GaP interlayer the center of the Ga-containing structures can be etched off with HCl (d).

All measurements just presented indicate that an intermixing of Si and Ga occurs for a GaP layer with an insufficient thickness, as Ga reaches into Si. Similar to the deposition of Ga directly on Si (001), this leads to the formation of more stable structures, which is probably due to a formation of a protective Si layer atop the Ga aggregates. To achieve an improvement compared to the direct deposition on Si (001) by the usage of a GaP interlayer on the Si (001) surface, a sufficient GaP layer thickness is necessary. For this reason, a GaP layer thickness of at least 22 nm will be applied for all following samples exhibiting a GaP interlayer.

Influence of the gallium phosphide surface properties

In the STEM measurement presented in fig. 4.46, it was found that for the deposition of TEGa, pyramidal Ga-containing structures form in GaP similar to those found in Si (001). As this was detected for Ga deposited on a GaP layer grown on Si (001), it is unclear whether this effect intrinsically occurs for Ga deposition on GaP or if it is due to the influence of the underlying Si substrate. Additionally, it was observed that Ga aggregates preferably form in the APBs of the GaP surface. However, the actual influence of the APBs on the structures forming is not yet clear. For an extensive comprehension of this growth process, TEGa was deposited on two GaP interlayers on different Si (001) substrates as well as on GaP (001) substrate. TEGa was deposited for 4 s at 450 °C applying identical growth conditions for all samples. A comparison of the structures forming by means of AFM measurement is depicted in fig. 4.49.

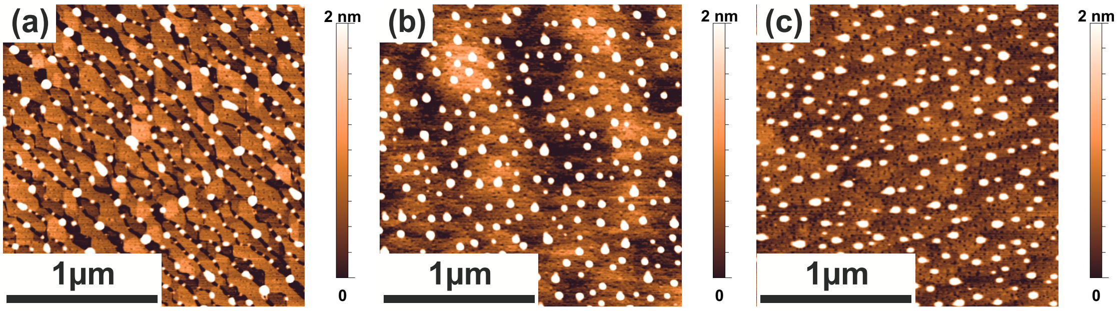

Figure 4.49: AFM micrographs of TEGa deposited for 4 s at 450 °C on a GaP layer on Si (001) with a high density of APBs (a), on a GaP layer on Si (001) with a low density of APBs (b) and on a GaP substrate (c); besides the difference in substrates used, all samples were deposited using equivalent growth conditions.

Image 4.49 (a) displays a GaP layer with a high density of defects at the surface, such as especially APBs, after TEGa deposition. This was already shown in fig. 4.45 and fig. 4.46. For the preparation of the sample presented in image 4.49 (b) a 12" Si (001) substrate with a lower defect density was used. Additionally, special care was taken to the formation of double-layer steps on the Si surface prior to the GaP deposition, resulting in a significant reduction of APBs in GaP, and therefore, a lower density of defects at the surface. For the sample shown in image 4.49 (c), TEGa was deposited on a GaP buffer on GaP (001), which was prepared as displayed in fig. 4.28. Ga-containing mounds form on all of the substrates. However, the number of structures forming strongly depends on the quality of the substrate. An evaluation of the number of aggregates forming for the three different surfaces displayed is shown in fig. 4.50.

The comparison clearly reveals that the number of mounds occurring considerably decreases with decreasing APB density of the surface used for the Ga deposition. As the amount of deposited Ga is constant for all samples, the mean size of mounds increases with

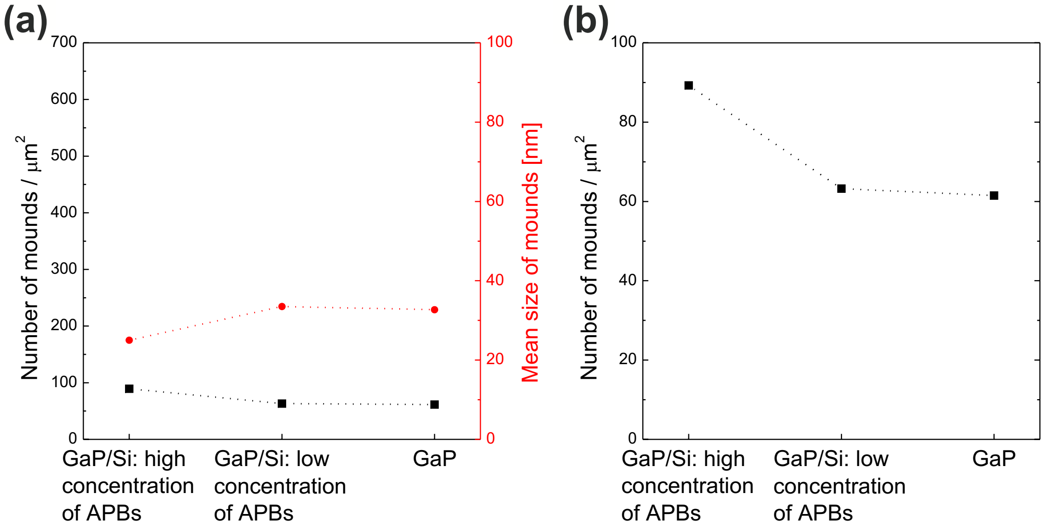

Figure 4.50: Evaluation of the relation between the number of structures, which form during TEGa deposition, or their mean size and the quality of the substrate (a) for the three different samples shown in fig. 4.49. For a better visibility an enlarged section of (a) is shown in (b).

a reduced defect density. This is in good agreement with findings for the Ga deposition on Si discussed earlier, which also indicated that the formation of Ga aggregates preferably occurs at defects, such as step edges (fig. 4.16). Similar to the step edges for the differently pretreated Si substrates, the amount of possible aggregation sites seemingly influences the formation of the Ga-containing structures. It is not yet know, which exact characteristic of the defects causes this influence. APBs, as well as S_B step edges, generate charged defects at the surface, and this charge might have an effect on the formation of the Ga-containing structures. Besides the Ga aggregates, the AFM images in fig. 4.49 additionally reveal a large number of holes in the GaP surface. These holes presumably originate from small Ga aggregates initially forming on the GaP surface during the growth and etching into the GaP. Since the deposited Ga is mobile on the GaP surface at a sufficient temperature, the initial Ga-containing structures merge to larger aggregates. Based on these findings, it is assumed that the defect density of the growth surface does not influence the initial deposition, but rather the mobility of the Ga on the GaP surface, and thus the converging of the smaller Ga structures.
HAADF STEM measurements were performed at the samples just discussed, to analyze the influence of the underlying Si (001) substrate or the quality of the GaP growth surface on the structures forming in the GaP after Ga deposition. Images of those measurements are displayed in fig. 4.51.

Like for fig. 4.49, image (a) was taken at a sample after TEGa deposition on a GaP layer on Si (001) exhibiting a high density of APBs. Sample (b) shows Ga on a GaP

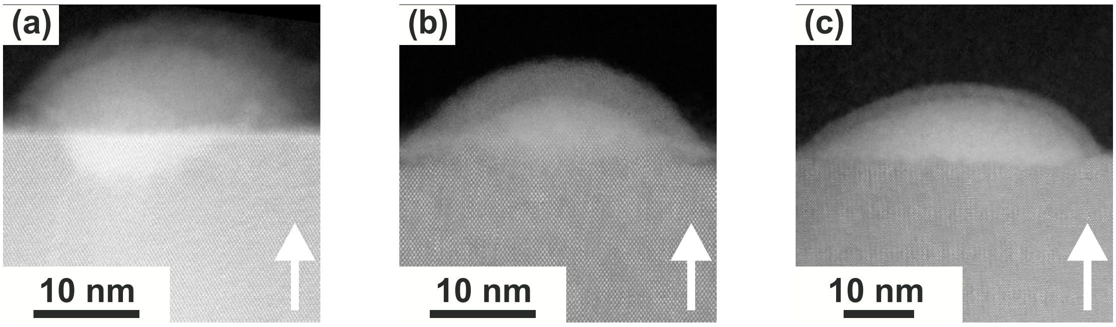

Figure 4.51: Cross-sectional HAADF STEM images of TEGa deposited at 450 °C for 4 s on two GaP layers on Si (001) with a high or a low densities of APBs (a) and (b) respectively and on GaP (001) substrate (c); AFM images of the same samples are shown in fig. 4.49.

layer on Si (001) with a low density of APBs and image (c) presents Ga deposited on a GaP (001) substrate. Aggregates on the surface are visible for all samples in the STEM measurements. These aggregates were already revealed by AFM. For the sample with a high density of APBs (a), a structure with bright contrast in the GaP layer is clearly apparent, originating from Ga diffused into the GaP; this can not be seen for neither of the other samples. However, as the AFM images (fig. 4.51) of these samples clearly revealed holes in the GaP surface, originating from the initial Ga aggregates etching into the surface, it is not assumed that no Ga diffuses into the GaP for the samples (b) and (c). Rather, it is probable, that less Ga diffuses into the GaP, and therefore, smaller structures form in the GaP. Additionally a difference in the samples' thickness could explain a difference in contrast, since the amount of crystalline GaP, which is unaffected by the metallic Ga and penetrated by the electron beam, increases with growing sample thickness. Due to the reasonably low difference in contrast between the GaP crystal and the Ga structures in the STEM measurement, these might not be clearly visible. While the structures forming on the GaP have a similar dimension for the three different samples investigated here, the Ga diffusion into the GaP is only considerably pronounced for the sample with the high density of APBs. The structures forming resembles the structures found for the Ga deposition on Si (001), although, as said before (fig. 4.46) they are limited by boundaries with a flatter angle than the {111} lattice planes. As the structures occurring after Ga deposition on a GaP layer on Si (001) with a low density of APBs resemble those arising for the Ga deposition on GaP (001) substrate, it can be stated that the APBs have a great effect on the diffusion of Ga into GaP and the formation of the pyramidal structures, such as seen in image 4.51 (a). One noticeable feature of the structure presented in fig. 4.51 (b), are the crystalline pyramidal shaped GaP structures inside the amorphous Ga. These peculiarly shaped structures are supposedly also caused by GaP lattice planes with higher indices being more stable than the GaP (001) lattice plane, as for Si. The GaP building these structures might originate from crystalline GaP from the GaP layer, dissolving in the liquid Ga at growth temperature and forming a new crystal at lower temperatures, as seen before for Si or GaP. For this effect a more pronounced etching of the Ga into the GaP is expected, though, as considerable amounts of GaP must have been dissolved in the Ga at growth temperature. Rather it is assumed, that some TBP, from the GaP growth, might have remained in the growth reactor or on the samples surface despite the growth interruption, resulting in GaP growth during the Ga deposition.

Temperature dependency

The influence of the growth temperature on the characteristics of the structures arising was analysed for the deposition of Ga on a GaP layer on Si (001), as before for the deposition of Ga on Si (001). Again the two Ga precursors TEGa and TMGa were used and will be compared in the following.

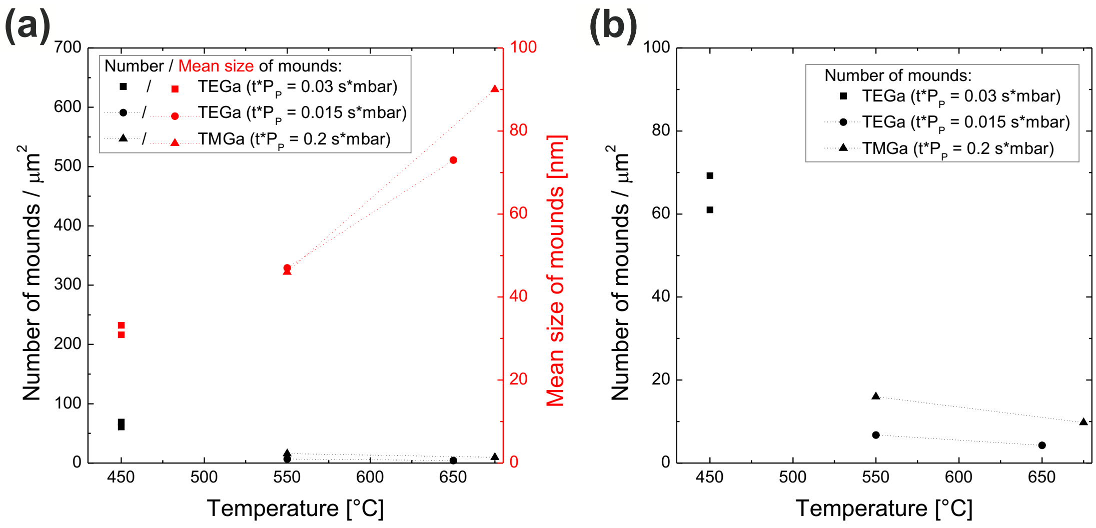

Figure 4.52: Analysis of the temperature dependency of the number and size of structures forming for the deposition of TEGa or TMGa on a GaP layer on Si (001) with low density of APBs, as shown in fig. 4.49 (b). An enlarged section of (a) is shown in (b).

To exclude effects by surface defects as far as possible, GaP with a low density of APB was utilized as growth surface for the samples discussed in this section. An evaluation of various samples grown with TEGa or TMGa at different temperatures between 450 °C and 675 °C is shown fig. 4.52. To compensate for the differences in the decomposition rate at different temperatures and between the different precursors, varying growth times or partial pressures were applied. Seemingly, this does not have an influence on the temperature dependency, though. The diagram presents the number as well as the mean size of the Ga-containing aggregates forming, plotted against the Ga deposition temperature. It reveals that the size of the structures rises with increasing temperature for either precursor, while the number of mounds decreases. As for other samples before, this behaviour can be explained by the increasing mobility of the Ga on the GaP surface with rising deposition temperature. Remarkable, though, is the fact that, in contrast to the results for the Ga deposition on Si, the characteristics of the structures forming here are similar for both Ga precursors. Comparing the results depicted in this diagram with those presented in fig. 4.15 and fig. 4.22 on the deposition of TEGa and TMGa on Si (001) reveals that the behaviour of TEGa on GaP differs significantly from that on Si. For the latter a largely increased number of smaller Ga-containing mounds emerged for all growth temperatures investigated. Rather, the behaviour observed here for the deposition of TMGa as well as of TEGa resembles the characteristics of the deposition of TMGa on Si (001). Therefore, it is assumed that the special features found for the deposition of TEGa on Si (001) do not directly result from the decomposition characteristics of the TEGa itself. More likely, as already suggested in fig. 4.6, polyethylene chains, formed by the residual organic groups, might be deposited on the Si (001) surface during the TEGa deposition, resulting in a reduction in the mobility of Ga on the Si surface. Seemingly, this process does not occur for the deposition of TEGa on GaP or for the deposition of TMGa.

Annealing

As before, also for this material system the influence of a high-temperature treatment was investigated. This was done to analyze the possibility of using this sample pretreatment for the deposition of C, or especially the possibility of utilizing the Ga structures for the catalytic growth of ordered C structures.

Exemplary, results will be shown for various annealings of a sample were initially TEGa was deposited for 4 s at 450 °C on a GaP layer on Si (001). Each annealing was performed in the growth reactor in H_2 atmosphere and a reactor pressure of 50 mbar. AFM measurements of the as-grown sample and samples after different annealings at various annealing temperatures or times are displayed in fig. 4.53 (a) and (b)-(e) respectively. To study the influence of an increasing annealing temperature on the Ga-containing structures, an annealing was performed for 5 min each at 500 °C (b), 600 °C (d) and 700 °C (e). To examine the time dependency, samples were annealed for 5 min (b) and 15 min (c) each at 500 °C.

The measurements reveal that, due to the annealing, the number of structures on the surface decreases, while their size grows. This effect increases for a raise in the annealing duration as well as for increasing annealing temperatures. It is presumably caused by a merging of the Ga-containing structures on the GaP surface for sufficiently high temperatures, as given during the annealing. After an annealing for 15 min at 500 °C (c), the surface structure of the GaP appears significantly changed, as the step structure is not clearly noticeable any more and elongated gaps arise. As these gaps seemingly occur in close proximity to the Ga aggregates, two mechanisms for their formation are conceivable. Firstly, this change might result from the movement of the Ga-containing

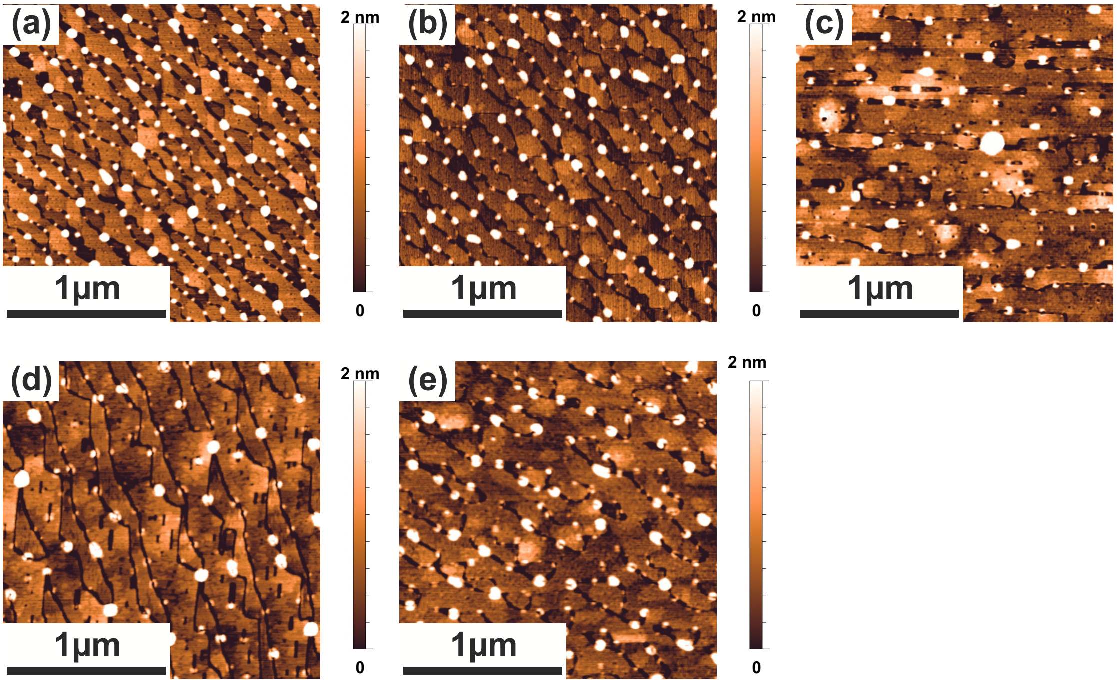

Figure 4.53: AFM images of TEGa deposited on an approximately 22 nm thick GaP layer on Si (001) substrate, as-grown (a) and with different annealings. An annealing at 500 °C for 5 min or 15 min was performed for (b) and (c) respectively. An annealing for 5 min and a temperature of 600 °C or 700 °C was carried out for (d) and (e) respectively.

mounds on the surface during the annealing. The liquid Ga presumably dissolves some of the crystalline GaP surface layers, which might lead to a considerably change in the overall surface structure. On the other hand, it was found that the Ga structures preferentially form at surface defect sites, such as APBs. The gaps in the surface might origin from an evaporation of P from the surface, as no stabilization was performed during the annealing. No significant changes in the GaP surface structure were observed for an unstabilized annealing of samples without a previous Ga deposition even at considerably higher temperatures (fig. 4.29). However, for these samples GaP substrates or GaP with a low defect density was used. The gaps, as well as their particular form, might simply result from the surface defects of the GaP used here, as these might also serve as sites for a facilitated evaporation. Also a combination of both mechanisms might be possible, as the Ga-containing aggregates might cause additional surface defects, again serving as desorption sites. Lesser changes can also be observed at the other samples after annealing. Here the step size grows with rising annealing temperature. For the sample annealed at 700 °C (e) the round shape of the aggregates is not as pronounced any more and holes appear in the structures, which are arranged along the APBs of the GaP. This appearance of holes could be caused by different effects. Possibly, at this high temperature the Ga might either desorb from the surface or diffuse further into the GaP layer. An emerging of holes in the surface after an annealing was observed before in section 4.2.3 for TMGa deposited on Si. For those samples though, this effect did not occur for an annealing temperature of 700 °C, but only for an annealing at 800 °C. But, as the loss of Ga appears especially at the APBs here, these defects might have a major influence on the Ga loss process and lead to a lowering of the temperature needed. Based on the particular shape of the Ga-containing structures after the high-temperature annealing, it is not expected, that after this treatment metallic Ga is still present on the surface, since metallic Ga, being liquid during the annealing, is expected to form round droplets. To verify this hypothesis and study the state of the Ga-containing structures of the other samples, the annealed samples shown in fig. 4.53 (b)-(e) were etched for 1 s in 30 % hydrochloric acid; thereby all metallic Ga was removed from the surface. AFM images of the samples after etching are presented in fig. 4.54.

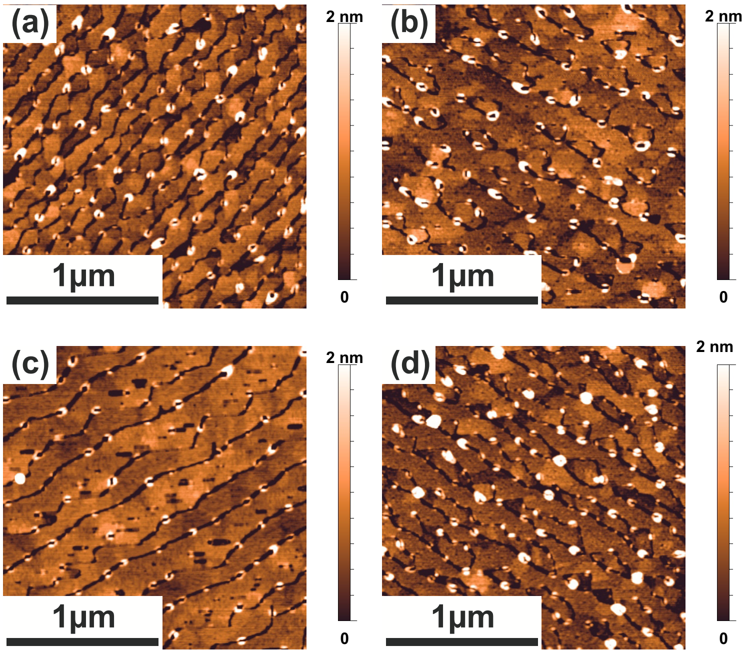

Figure 4.54: AFM images of TEGa deposited on an approximately 22 nm thick GaP layer on Si (001) substrate with different annealings after etching for 1 s in 30 % HCl; the annealings were carried out for 5 min at 500 °C (a), 15 min at 500 °C (b), 5 min at 600 °C (c) or 5 min at 700 °C (d). The as-grown samples are shown in fig. 4.53 (b)-(e).

The measurements were performed after etching of two samples annealed at 500 °C for 5 min (a) and 15 min (b) respectively and of two samples annealed for 5 min at 600 °C (c) and 700 °C (d) respectively. The Ga aggregates can partly be etched of for all samples, leaving remnants on the GaP surface. These remnants are especially pronounced for the sample annealed at 700 °C (d). Since holes were already observed in the Ga-containing structures prior to the etching, only marginal changes are noticeable for this sample caused by the etching in HCl. Presumably, the remains found for all samples consist of GaP forming from the Ga aggregates during the annealing. Two possible explanations can be given for the formation of this GaP. On the one hand, the liquid Ga structures might dissolve the underlying GaP at a sufficient temperature during the annealing. During the cool-down amorphous or crystalline GaP might form again. As seen for Si in fig. 4.19 and 4.21, this formation might begin at the outer edges of the Ga-containing structure. Thus, the structures might be covered by a protective GaP layer. On the other hand, at the temperatures applied for annealing, phosphorous from the sample or reactor, especially the susceptor, might have desorbed from its original position and adsorbed again at the metallic Ga, again leading to the formation of crystalline GaP.

As a conclusion, it can be stated that the deposition of Ga on a GaP layer on Si (001) is possible, although a sufficient thickness of the GaP layer is required to prevent intermixing of Ga and Si. For a high-temperature treatment of the deposited Ga, special care has to be taken, as a considerable movement of the Ga structures on the surface, as well as the formation of a covering GaP layer might hinder the growth of ordered C structures.

4.6 Carbon deposition

The previous sections mostly presented the results found for the deposition of Ga. However, as already stated, the motivation to explore Ga deposition was to make use of the catalytic effect of metallic Ga on the growth of ordered C structures. Therefore, utilizing this approach, the findings introduced in the last chapters build a crucial basis for the deposition of C. This section looks at the C deposition and the influences of the various C precursors (benzene, TBEthylene, TBEthyne and ethylene), different substrates, and different pretreatments.

4.6.1 Carbon deposition on gallium-pretreated silicon (001)

Firstly, C deposition on Si (001) substrates pretreated with Ga will be discussed. C deposition, using TBEthylene as the precursor, was performed at the same time as the Ga deposition for the samples shown first.

AFM measurements for three samples, each grown at a temperature of 450 °C and a deposition time of 15 s are displayed in fig. 4.55. For all samples the partial pressure of the Ga precursor TEGa was kept constant at 7.6×10^{-4} mbar.

For the sample shown in fig. 4.55 (a) only TEGa was offered, while for the samples in (b) and (c) TBEthylene was supplied simultaneously during the whole 15 s using a partial pressure of 3.1×10^{-3} mbar for (b) and 3.1×10^{-2} mbar for (c) respectively. The AFM images reveal that mounds form on the Si surface for all chosen conditions, while the underlying surface structure is still clearly detectable. However, a comparison of the different samples shows that the C precursor influences the deposition. The coverage of the surface decreases with increasing TBEthylene partial pressure. A particular evaluation

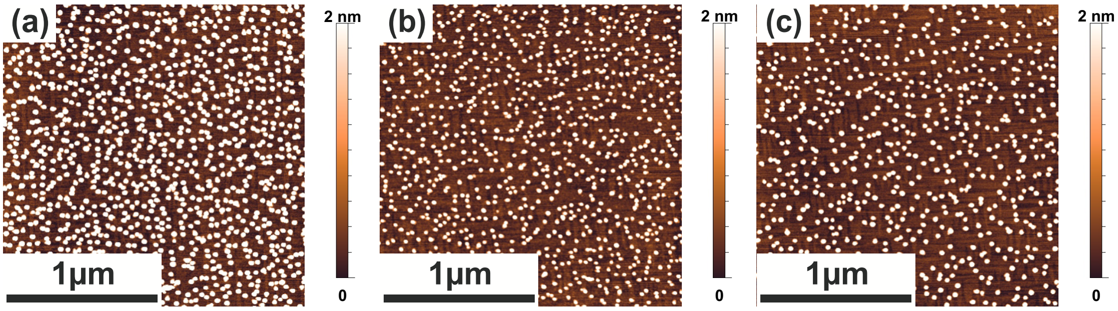

Figure 4.55: AFM images of samples after TEGa deposition on Si (001) for 15 s at 450 °C without additional C precursor (a) and with additional TBEthylene deposition. The TBEthylene partial pressure was increased from 3.1×10^{-3} mbar for (b) and to 3.1×10^{-2} mbar for (c)

of this behaviour is depicted in the diagram in fig. 4.56, where the number and mean size of the aggregates forming is plotted against the TBEthylene partial pressure chosen.

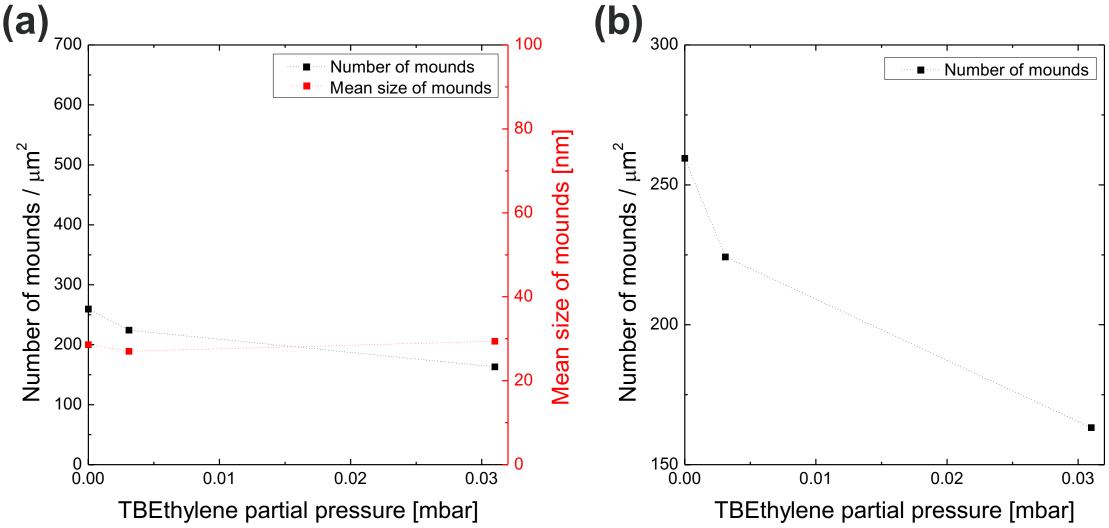

Figure 4.56: Analysis of the influence of the partial pressure of TBEthylene on the deposition of TEGa using the samples shown in fig. 4.55. An enlarged section of (a) is shown in (b).

As can be seen especially in fig. 4.56 (b), which is an enlarged section of (a), the number of structures formed clearly decreases with increasing TBEthylene partial pressure. At the same time, no explicit trend is found for a dependency of the mean size of the aggregates on the TBEthylene partial pressure. To get a deeper understanding of the processes occurring during this deposition, further investigations of those structures were performed by HAADF STEM. Cross-sectional images of samples after a deposition of only Ga (a) and of Ga and C simultaneously (b) are displayed in fig. 4.57.

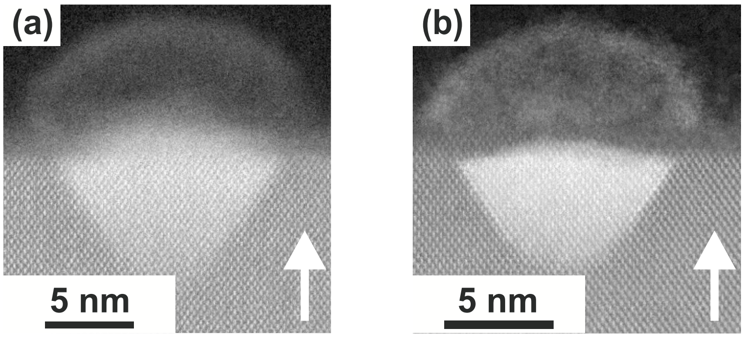

Figure 4.57: Cross-sectional HAADF STEM images of Si (001) after 15 s of TEGa deposition at 450 °C without (a) and with simultaneous deposition of TBEthylene (b), as shown in the AFM measurement in fig. 4.55 (a) and (c).

For both samples, bright pyramidal structures containing Ga occur in the Si, capped by an amorphous layer, as seen before for the deposition of only Ga on Si. Only marginal differences between the two samples with different growth conditions were found by STEM, but no indications of an influence by the C precursor. As no significant changes were found in the structures forming with or without a simultaneous deposition of TBEthylene, only in the amount of the structures on the surface, it is assumed that the influence of the C precursor observed is due to gas phase reactions between the two different precursors utilized. This would be in accordance with the results for TEGa deposition on Si displayed in fig. 4.9. These results revealed that a reduction of the TEGa partial pressure, which is comparable with a loss of TEGa due to gas phase reactions, results in a significant decrease in the number mounds forming that contain Ga, while the influence of the Ga partial pressure on their size is low. This was also observed in fig. 4.56 for the samples just discussed.

To prevent any possible gas phase reactions, the Ga and C precursor were therefore deposited separately. This growth process was now performed using a GaP interlayer on Si (001), as it was found that Ga structures might not possess a metallic Ga phase at the surface after deposition on Si. The growth of different C precursors was tested for varying deposition times. The growth temperature was kept constant at 500 °C for all samples, as it was found in fig. 4.53 and 4.54 that a high-temperature treatment significantly changes the characteristics of the Ga aggregates.

Samples after the deposition of benzene on a GaP surfaces, which was first pretreated with TEGa for 4 s at 450 °C, are shown in fig. 4.58. The deposition time for the benzene was increased from 5 min in image (a) to 15 min in (b) and 25 min, shown in (c). Comparing the structures found on the surface after the benzene deposition with an equivalent sample directly after TEGa deposition (fig. 4.53 (a)) or samples after an annealing without precursor, again at 500 °C (fig. 4.53 (b) for 5 min and (c) for 15 min respectively), reveals significant changes of the surface characteristics, presumably caused by the addition of

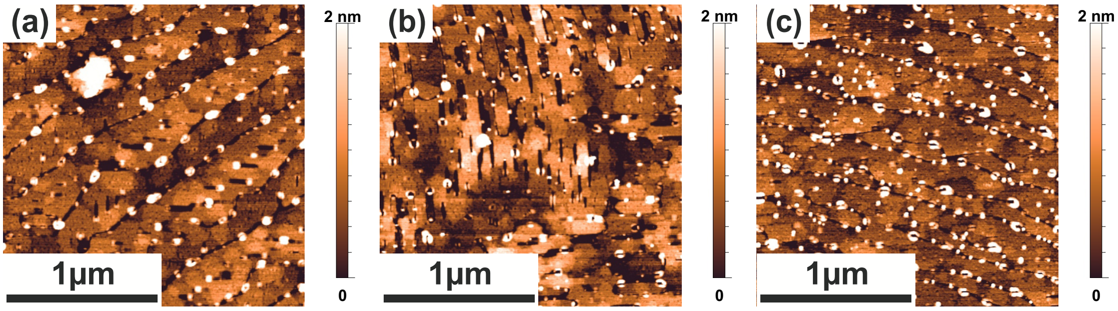

Figure 4.58: AFM micrographs of a GaP layer on Si (001) after 4 s of TEGa deposited at 450 °C followed by a deposition of benzene at 500 °C for 5 min (a), 15 min (b), or 25 min (c).

benzene. After the deposition of the C precursor all samples exhibit holes in the initially complete Ga-containing aggregates. While only small holes are found after a deposition time of 5 min, their extent increases with increasing deposition time. In addition, especially in images (a) and (b), elongated gaps appear in the GaP. Similar gaps were already observed before, after annealing of an equivalent sample without a precursor at 500 °C for 15 min (fig. 4.53 (c)). This effect, though, is considerably increased for the deposition of benzene, as no effect is recorded for an annealing duration of only 5 min without precursor. It was assumed before, that those elongated gaps might be caused by the defect-enhanced desorption of GaP from the surface, as no stabilization is performed. Presumably, the addition of benzene increases this desorption. This behaviour might be explained by benzene molecules initially adsorbing on the GaP surface building larger molecules including Ga or P from the surface. Thereby the bond strength between the atoms on the surface might by reduced, resulting in an enhanced desorption of the surface atoms. A similar process, leading to an etching of the Ga structure, could explain the holes found in the Ga-containing aggregates. As these holes occur solely atop of APBs, it has to be assumed that these strongly influence the vanishing of the Ga. However, it was found before (fig. 4.45) that similar holes appear in the Ga aggregates deposited on an equivalent GaP surface under identical growth conditions after etching in HCl. Therefore, it is assumed, that metallic Ga is only present in the center of the mounds, while the outer parts consist of (poly-)crystalline GaP, which might not evaporate at the chosen conditions. In addition to the existence of the elongated gaps, the AFM images also reveal that those gaps run perpendicular to each other in different regions of the sample. This is probably due to the surface reconstruction of the GaP on the Si (001). It is assumed that, similar to the findings on the Si (001) surface, also here dimer rows form, which run parallel or perpendicular to the step edges. Presumably, the desorption of surface atoms is either enhanced along the dimer rows, or vacancies diffuse along the rows and coalesce, forming elongated gaps in the direction of the dimer rows. As the dimer rows run in perpendicular directions on different terraces of the surface, separated by the APBs, perpendicular gaps arise.

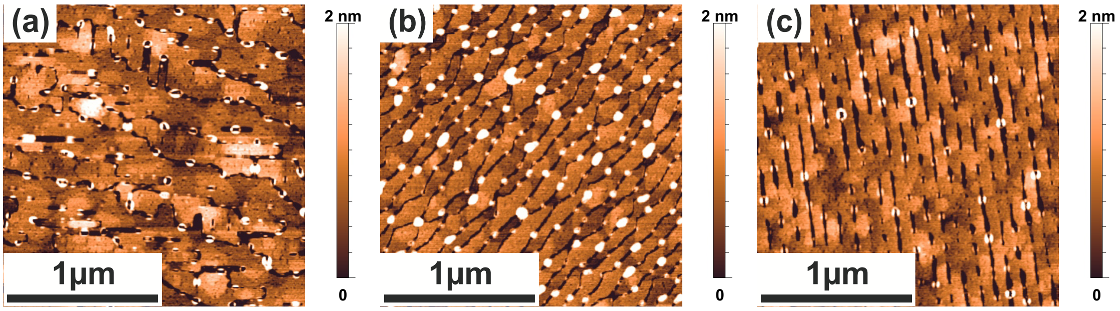

Figure 4.59: AFM micrographs of a GaP layer on Si (001) after 4 s of TEGa deposited at 450 °C followed by a deposition of TBEthyne for 5 min (a) or TBEthylene for 5 min (b) and 25 min (c) at 500 °C.

AFM images of samples deposited utilizing equivalent conditions as in fig. 4.58, only with different C precursors, are presented in fig. 4.59. For the usage of TBEthyne, presented in fig. 4.59 (a), holes appear in the mounds already after a deposition time of 5 min. Also, for this sample elongated gaps occur in the GaP surface, as before for the benzene deposition. After 5 min of TBEthylene deposition (b) the structures as well as the surface are still intact. For an increased deposition time, for this precursor, too, holes develop in the Ga-containing aggregates and gaps in the surface, as shown here for a growth time of 25 min (c). This C precursor might attach to the surface to a lesser degree resulting in a reduced etching rate in comparison to benzene or TBEthyne. However, as a similar effect was also found after 15 min of annealing at 500 °C in hydrogen atmosphere without supplying a C precursor (fig. 4.53). Therefore, for TBEthylene supply possibly only the effect of the annealing is observed.
STEM investigations were performed on those samples to verify the hypothesis given that the particular surface structures found in fig. 4.58 and fig. 4.59 evolve by etching and not by a deposition of additional material on the surface or perhaps a diffusion of Ga deeper into the substrate.

STEM images of a sample already shown by means of AFM in fig. 4.59 (c) are shown in fig. 4.60. TBEthylene was deposited for 25 min at 500 °C on a GaP layer on Si (001) which was pretreated with TEGa. After the TBEthylene deposition, structures with a dark contrast appear in the GaP, replacing the bright Ga-containing structures after the TEGa deposition seen in fig. 4.46. These dark structures presumably display the voids found by AFM. No difference in the GaP crystal structure was found surrounding those voids. Also, no additional layer can be detected originating from the C deposition. This confirms the hypothesis stated above that the deposition of benzene, TBEthyne and TBEthylene on Ga pretreated GaP surfaces leads to an etching of the Ga-containing structures and the surface, rather than to a growth process.

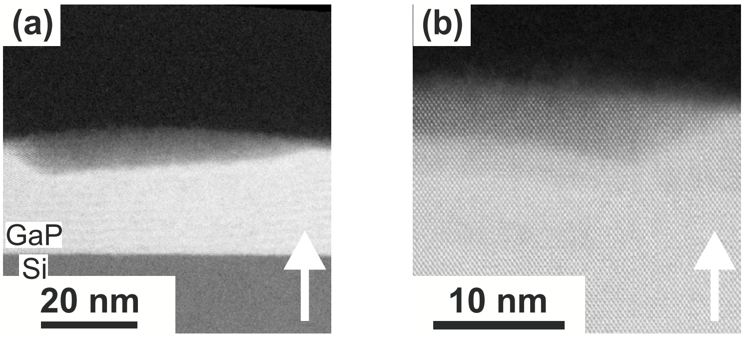

Figure 4.60: Cross-sectional HAADF STEM images, utilizing two different magnifications, of a GaP layer on Si (001) after deposition of TEGa at 450 °C for 4 s followed by 25 min of TBEthylene deposition at 500 °C as already shown in the AFM measurement in fig. 4.59.

Astonishingly, different results were gained when a slow sample cool-down was performed after the C deposition by applying a low cooling rate in order to allow additional surface diffusion. To achieve a low cooling rate and controlled temperatures the sample was cooled down in 100 °C steps and kept at each respective temperature for 10 min. This was started at 500 °C and four such intervals were applied during the cooling. Two such samples after deposition of benzene (a) or TBEthyne (b) are presented in fig. 4.61 by means of AFM.

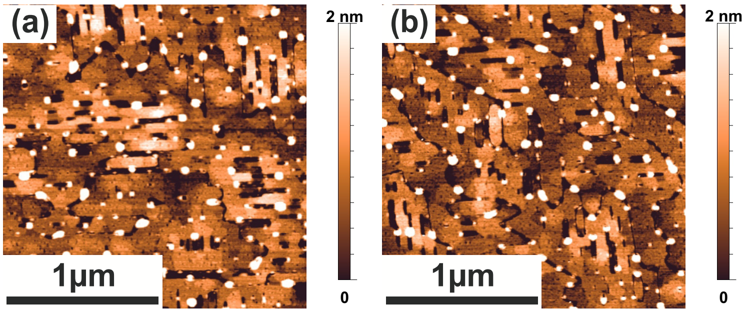

Figure 4.61: AFM images of TEGa deposited at 450 °C for 4 s on a GaP layer on Si (001) and additional deposition of Benzene (a) or TBEthyne (b) for 5 min at 500 °C . Equivalent growth conditions were used for the samples shown here as for the samples in fig. 4.58 (a) and fig. 4.59 (a) respectively, but a slow cooling rate was applied.

For those samples the particular C precursor was deposited for 5 min at 500 °C. A GaP layer on Si (001), which was pretreated with TEGa prior to the C deposition, was used as substrate. Besides the low cooling rate, the growth conditions chosen resemble those used for the samples shown in fig. 4.58 (a) for the benzene, and fig. 4.59 (a) for the TBEthyne deposition respectively. Again gaps occur in the GaP surface, but here the mounds on the surface appear intact after the deposition. This is in contrary to the samples grown with the commonly used, faster cooling rate. Judging from the AFM measurements, no influence of the C precursor on the Ga-containing aggregates was found for this treatment. To gain a better understanding of the effect resulting from a slow cooling, STEM measurements were performed at one of the samples discussed.

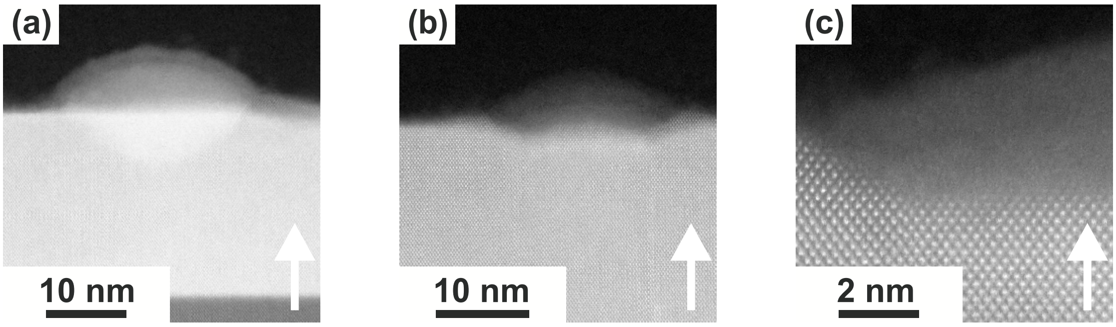

Figure 4.62: Cross-sectional HAADF STEM images of a GaP layer on Si (001) after the deposition of TEGa for 4 s at 450 °C (a) and after additional 5 min of TBEthyne deposition at 500 °C with slow cool-down (b) and (c), as already shown in the AFM image in fig. 4.61 (b).

A STEM image of a sample after the TEGa pretreatment is displayed in fig. 4.62 (a). A STEM measurement of this sample, utilizing a different magnification, was already shown in fig. 4.51. It shows a bright Ga-containing structure partly etched into the GaP. The micrographs shown in fig. 4.62 (b) and (c) were taken on a sample after an equivalent Ga treatment, but with an additional 5 min of TBEthyne deposition at 500 °C followed by a slow cool-down of the samples, as already shown in fig. 4.61 (b). In contrast to the sample shown in fig. 4.60, which was grown using similar conditions but no slow cooling, amorphous aggregates remained on the GaP surface after this sample treatment. But, also in comparison to the as-grown sample (a), clear changes in the Ga-containing structures were found after the deposition of TBEthyne (b). The amorphous structure does not seem to expand into the GaP any more but is presumably only located at the surface after this treatment. Also, the contrast has changed from being brighter than that of GaP for the as-grown sample, as expected for Ga, to being darker than GaP after the TBEthyne deposition. Until now, neither the effect of the slow cooling nor the composition of these amorphous aggregates is understood. Further investigations are necessary.

In addition to the deposition of Ga, large Ga droplets on GaP can also be generated by annealing GaP at suitable annealing conditions, as demonstrated in fig. 4.33. Since for this method, the size of the Ga-containing structures and therefore the amount of metallic Ga is significantly increased in comparison with the Ga structures generated by TEGa or TMGa deposition, these droplets might have a different effect on the deposition of C. Here not only surface effects might be of major importance but an increased diffusion of the C precursor, or decomposition products thereof, into the liquid Ga structures might occur.

A SEM map (a) as well as two EDX spectra (b) taken on a GaP (001) substrate after a high-temperature annealing at a reactor pressure of 950 mbar generating Ga droplets,

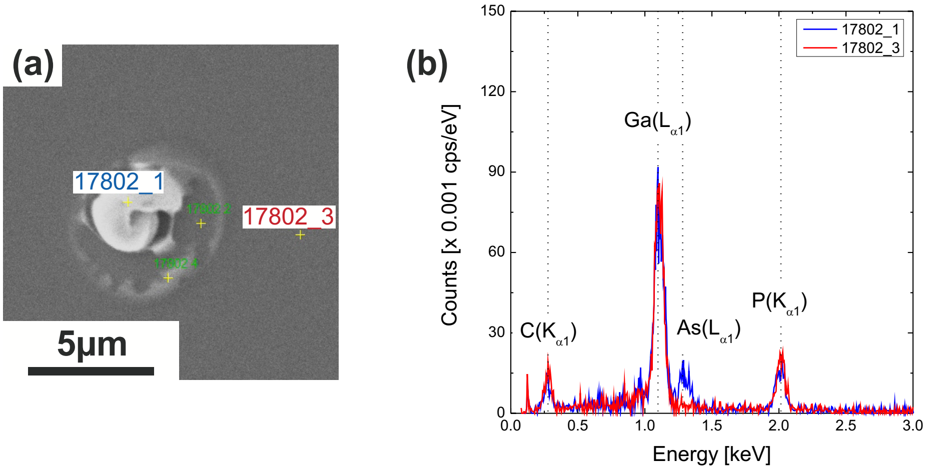

Figure 4.63: SEM (a) and EDX (b) measurements of the surface of a GaP substrate after annealing for 15 min at 675 °C under H_2 at a reactor pressure of 950 mbar followed by a deposition of TBEthyne at 675 °C for 15 min.

as described in section 4.3, and an additional TBEthyne deposition for 15 min at 675 °C using a TBEthyne partial pressure of 2 mbar are presented in fig. 4.63. A similar sample after an equal annealing but without an additional TBEthyne deposition is presented in fig. 4.33, exhibiting significant Ga droplets on the surface. No such droplets appear here. Rather, bright remains are revealed in the SEM map (a). The circular outer shape of the remnant might indicate the existence of a Ga droplet at this location prior to the TBEthyne deposition. The two EDX spectra presented were recorded at the spots marked in the SEM image as 17802_1, placed on the protruding bright structure, and 17802_3, at the border of the SEM image, in some distance to the bright features. A comparison of the EDX point measurements indicates that those remnants consist of GaAs instead of pure Ga (b). Due to the high-temperature annealing, Ga droplets developed on the surface before the C deposition. However, as seen before, those Ga droplets were etched off by the C precursor. Coincidentally, small amounts of residual arsenic from earlier experiments in the growth reactor formed crystalline GaAs with some of the liquid Ga prior to the etching and account for the remains found on the surface.

In conclusion, it can be stated that, with all C precursors studied, namely TBEthyne, TBEthylene and benzene, a C deposition on Ga pretreated GaP surfaces led to an etching process rather than to a growth of C-containing structures. This is presumably due to chemical reactions between the Ga atoms and the C precursor molecules. Therefore, it was found that the initial approach of using liquid, metallic Ga as catalyst for the growth of ordered C structures appears not to be feasible.

4.6.2 Carbon deposition on gallium phosphide (001)

It was just shown that metallic Ga droplets, which were deposited prior to the C growth until now in this study, are etched off by the C precursor. In the mean time, graphene growth had been reported on germanium (Ge) [104], [88]. Atmospheric pressure chemical vapor deposition APCVD was used in the former, low pressure chemical vapor deposition (LPCVD) in the latter report. For theses studies Ge substrates or Ge deposited on Si substrates was used. As for the deposition on transition metals, the C precursor CH_4 was supplied in combination with H_2 or a mixture of H_2 and Ar using a horizontal tube furnace. Growth temperatures around 900 °C and deposition times in the minute to hour range were applied. Homogeneous monolayer graphene was observed on the Ge surface, after optimizing the growth conditions. This single layer growth, is based on the low solubility of C in the Ge substrate [104], as previously discussed for Cu (section 2.1.3). Si, however, exhibits a high solubility of C. A direct growth of graphene on Si would therefore not be possible by surface diffusion, but only by a saturation of the Si substrate with C and a precipitation process during the cool down. For this reason, the C deposition is performed directly on GaP without catalyst in the following. GaP (001) or a GaP layer on Si (001) was chosen over Si (001) substrate here, since the low C diffusivity on a Si surface and the high C solubility might hinder the direct growth of high-quality graphene on Si (001) surfaces [88]. Additionally, instead of the C precursors benzene, TBEthyne and TBEthylene used in the last section, now only the more commonly used C precursor ethylene was chosen. This was done as a graphene deposition using this particular precursor has already been performed on other metallic surfaces as Ru (0001) [41], Ni (111) [105] or Pt (111) [106] and is therefore studied more intensely. Presumably though, a higher deposition temperature is required for the decomposition of ethylene in comparison to the other C precursors used. The deposition of ethylene on Ga pretreated samples is infeasible so, as low growth temperatures are necessary here (see fig. 4.53 and 4.54). However, as shown in section 4.3, GaP is stable up to rather high temperatures of at least 800 °C, making the usage of ethylene possible.

The initial growth conditions were adapted from the high-temperature deposition of TBP on GaP, which leads to a C coverage of the surface (fig. 4.31). Figure 4.64 displays AFM images of two GaP (001) surfaces after different treatments. For both samples a GaP buffer was deposited first, as described in section 4.3. While the sample presented in fig. 4.64 (a) was subsequently annealed for 15 min at 800 °C in H_2 environment, the sample in (b) was annealed for the same time again at 800 °C applying an ethylene partial pressure of 1.5 mbar.

As already shown in fig. 4.29, the GaP appears still intact after annealing in hydrogen at 800 °C (a). Solely, the size of the surface steps changed due to the high-temperature treatment. After an ethylene deposition, though, the GaP surface structure

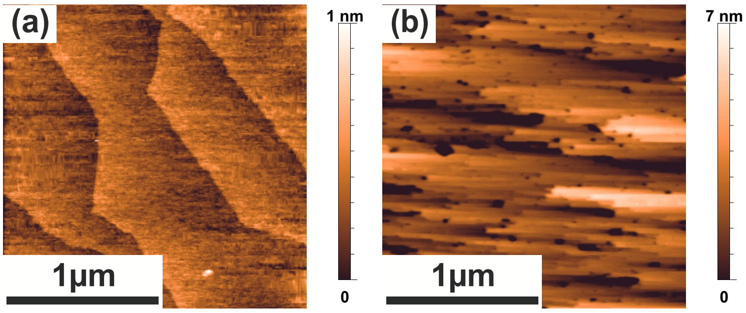

Figure 4.64: AFM images of a GaP (001) surface after the pretreatment described in fig. 4.28 followed by an annealing under H_2 (a) and the deposition of ethylene (b) respectively, each at 800 °C for 15 min. For better visibility two different height scales were used.

seems significantly changed and exhibits an increased roughness. Instead of atomic steps with relatively smooth step edges, now large holes and small terraces with ragged edges developed. Already in the previous section an etching of GaP due to a deposition of various C precursors was observed. Although the growth conditions applied here differ distinctly from those used in the last section, as a different substrate, varying C precursors and different deposition temperatures were utilized, based on the earlier results, it appears probable that again an etching process could have occurred.

The grown structure was also analyzed by secondary ion mass spectrometry, as a deposition of C on the GaP surface is not excluded, even for a simultaneously occurring etching process.

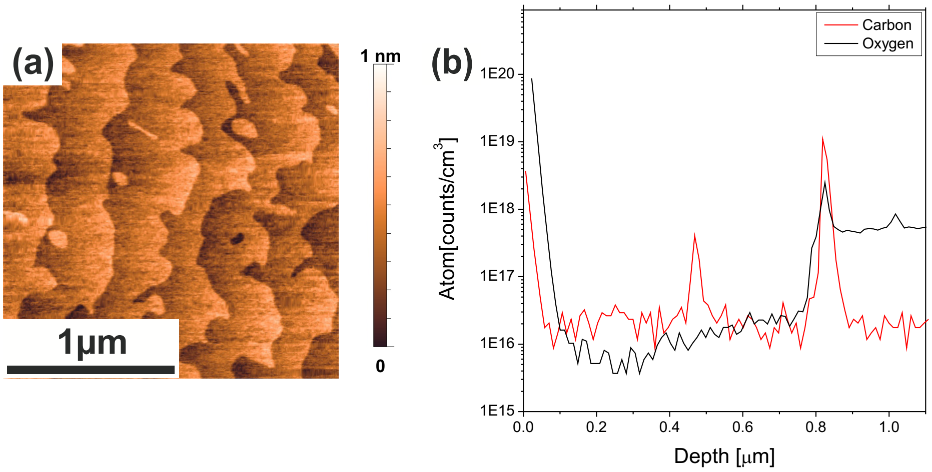

Figure 4.65: AFM (a) and SIMS (b) measurement of a 500 nm thick GaP layer grown on GaP (001) after annealing at 800 °C under ethylene, as shown in figure 4.64 (b).

For this reason, first a sample was prepared as shown in fig. 4.64 (b), depositing ethylene for 15 min at 800 °C on a GaP buffer. To protect the layer evolving due to this treatment, this surface was then covered by an approximately 500 nm thick GaP layer. This is necessary to ensure a reliable SIMS measurement, nevertheless, an influence of the GaP deposition on the structures to be investigated can not be excluded. An AFM image of this sample is displayed in fig. 4.65 (a), the corresponding SIMS measurement in (b). The AFM measurement, revealing smooth monoatomic surface steps on the GaP, displays that a good quality growth of GaP is possible despite the increased roughness of the ethylene treated surface. For the SIMS measurement the depth profiles for C and O are displayed. The O profile, as expected, exhibits only an increased O content at the interface between the GaP substrate and buffer and at the sample surface, which is among other things also due to measurement artifacts. The C content, however, is additionally slightly increased at the interface between the buffer layer and the 500 nm thick cap layer due to the ethylene treatment. A comparison with fig. 4.30, though, reveals that the amount of C deposited by this treatment is by several orders of magnitude lower than that found for a high-temperature treatment of GaP with the phosphorous precursor TBP. However, despite the low C content, ordered C structures might have formed during the deposition of ethylene.

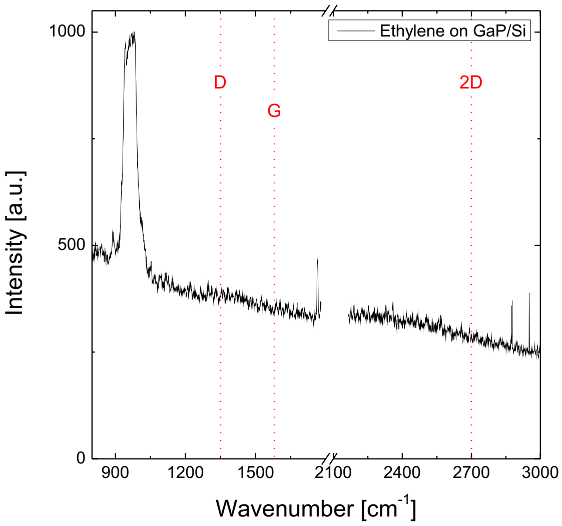

Figure 4.66: Raman spectrum of a GaP layer on Si (001) after 15 min of ethylene deposition at 800 °C .

To clarify whether this is true, Raman measurements were performed on as sample treated as shown in fig. 4.64 (b). But, as mentioned previously, the detection of small Raman signals is not possible in the wavenumber region above approximately 1000 cm^{-1} for the growth on GaP substrates, due to the significant background observed in this region. Therefore, instead of depositing ethylene on a GaP (001) substrate, a GaP layer on Si (001) was used as growth surface. As in fig. 4.64 (b) and 4.65 the ethylene deposition was performed for 15 min at 800 °C, applying a ethylene partial pressure of 1.5 mbar. The Raman spectrum taken at this sample is presented in fig. 4.66. Separate measurements were performed for the different wavenumber regions displayed. The red dotted lines demonstrate the expected approximate position for graphene originating Raman bands. While the amount of C at the surface of this sample is expected to be equivalent to the C content at the interface between the GaP buffer and cap, detected by SIMS, no C related peaks occur in the Raman spectra taken at this samples. Presumably the amount of ordered C structures on the surface is not sufficiently high for detection.

Small amounts of C can be deposited by this approach. But, it is not assumed that a growth of significant amounts of ordered C structures is possible. Perhaps, this is due to the etching process observed in fig. 4.64 (b) being more decisive than the C growth process. As the desorption of surface atoms increases with increasing temperature, lowering the C deposition temperature might lead to a reduction of the etching rate.

Therefore, again a GaP buffer was grown on GaP (001) followed by 15 min of ethylene deposition with a partial pressure of 1.5 mbar. Only, the deposition temperature was set to 700 °C, instead of 800 °C as used before. An AFM micrograph of this sample is displayed in fig. 4.67.

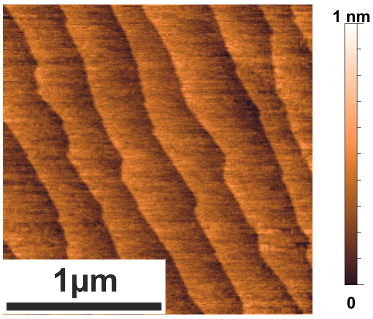

Figure 4.67: AFM images of a GaP (001) surface after 15 min of ethylene deposition at 700 °C.

For this treatment, though, no major alteration in comparison to a surface annealed at high temperature without C precursor (e.g. fig. 4.64 (a)) appears. This implies that an ethylene deposition using the growth conditions applied here has no influence on the sample. Apparently, neither a growth nor a etching process occurs. A C precursor enhanced etching was already observed at a deposition temperature of 500 °C, thus a considerably lower temperature, for the samples presented in section 4.6.1. There, however, different C precursors were used, which are expected to decompose at lower temperatures as compared to ethylene. This indicates that the etching process might not be caused by the precursor itself but by decomposition products thereof. Additionally, for those samples a GaP layer grown on Si (001) was used as substrate rather than GaP (001), which is used here, hence a substrate exhibiting significantly more defects. As mentioned before, it is assumed that these defects have a major impact on the etching process.

While no indication for etching was found here, no sign for C growth was found either. Until now H_2 was used as carrier gas for all deposition processes. However, the H_2 partial pressure is known to have a great influence on the C deposition for other CVD processes using different growth conditions. High hydrogen pressures lead to an etching rather than to a deposition of C there [107]. To verify whether this mechanism also occurs for the usage of GaP substrates and the growth conditions applied here, the deposition was also performed using N_2 as carrier gas.

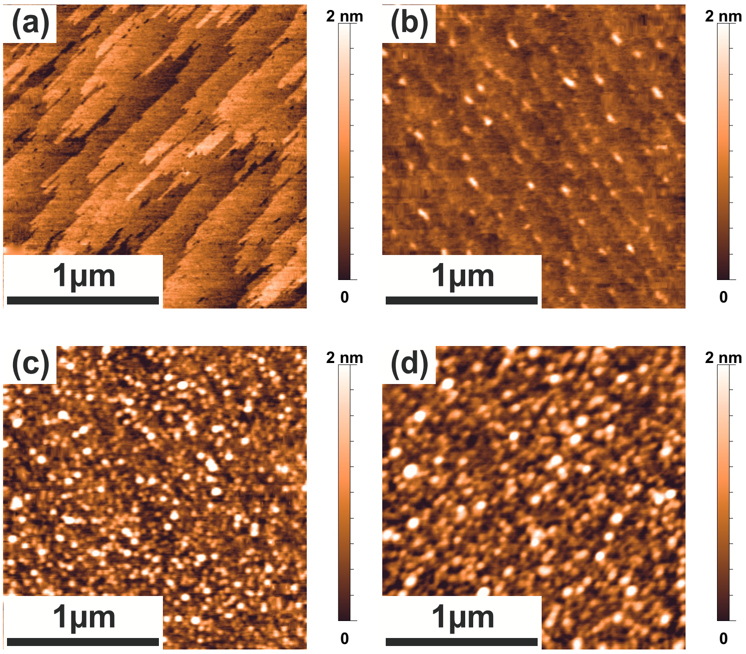

Figure 4.68: AFM micrographs of GaP (001) surfaces after an annealing in N_2 for 15 min (a) or a deposition of ethylene at 800 °C for increasing growth times of 1 min (b), 5 min (c) or 15 min (d) using N_2 as carrier gas.

GaP (001) samples after 4 differently treatments are displayed in fig. 4.68. For all surfaces initially a GaP buffer was prepared in H_2 atmosphere as described in section 4.3. The carrier gas was then switched to N_2 and the reactor temperature was increased to 800 °C. While the sample presented in (a) was only annealed in N_2 atmosphere for 15 min at this temperature, serving as a reference, ethylene was deposited in N_2 atmosphere on the samples shown in (b)-(d). The C deposition time was increased from 1 min in fig. 4.68 (b), to 5 min in (c) and 15 min for sample (d). The AFM measurement (a) reveals a clear change in the surface structure due to the annealing in N_2 compared to the surface found after an equivalent annealing in H_2, as shown in fig. 4.64 (a). However, although the GaP step edges seem significantly frayed and small holes occur after this treatment, the surface still appears rather intact and exhibits atomic steps. After 1 min of ethylene deposition (b) the GaP surface steps are still dimly recognizable, but evidently some material was deposited on the surface, accumulating especially along the step edges. A comparison of the three samples prepared with an increasing C deposition time (b)-(d) reveals that the roughness of the surface rises with increasing growth time. After 5 min of ethylene deposition the surface structure of the underlying GaP is not detectable any more. This indicates a growing deposition with increasing growth time.

Due to its lower defect density, GaP (001), rather than GaP on Si (001) substrate, was used for the samples discussed to investigate the deposition of ethylene preferably disregarding the influence of potential defects in the growth surface. However, as mentioned before, no reliable Raman measurements are possible for C deposited on GaP (001) substrates, like for the samples presented in fig. 4.68. Therefore the C deposition was performed on thin GaP layers on Si (001) for the samples discussed in the following. To verify whether C was deposited on the samples just discussed, the treatment presented in fig. 4.68 (b) was performed again on a GaP layer on Si (001). Additionally, as the aim of this work is to deposit graphene on existing, previously grown crystalline structures, the C growth temperature should be chosen as low as possible to avoid temperature caused damages of the underlying material. Therefore, the influence of a lower growth temperature on the C deposition will also be discussed in the following.

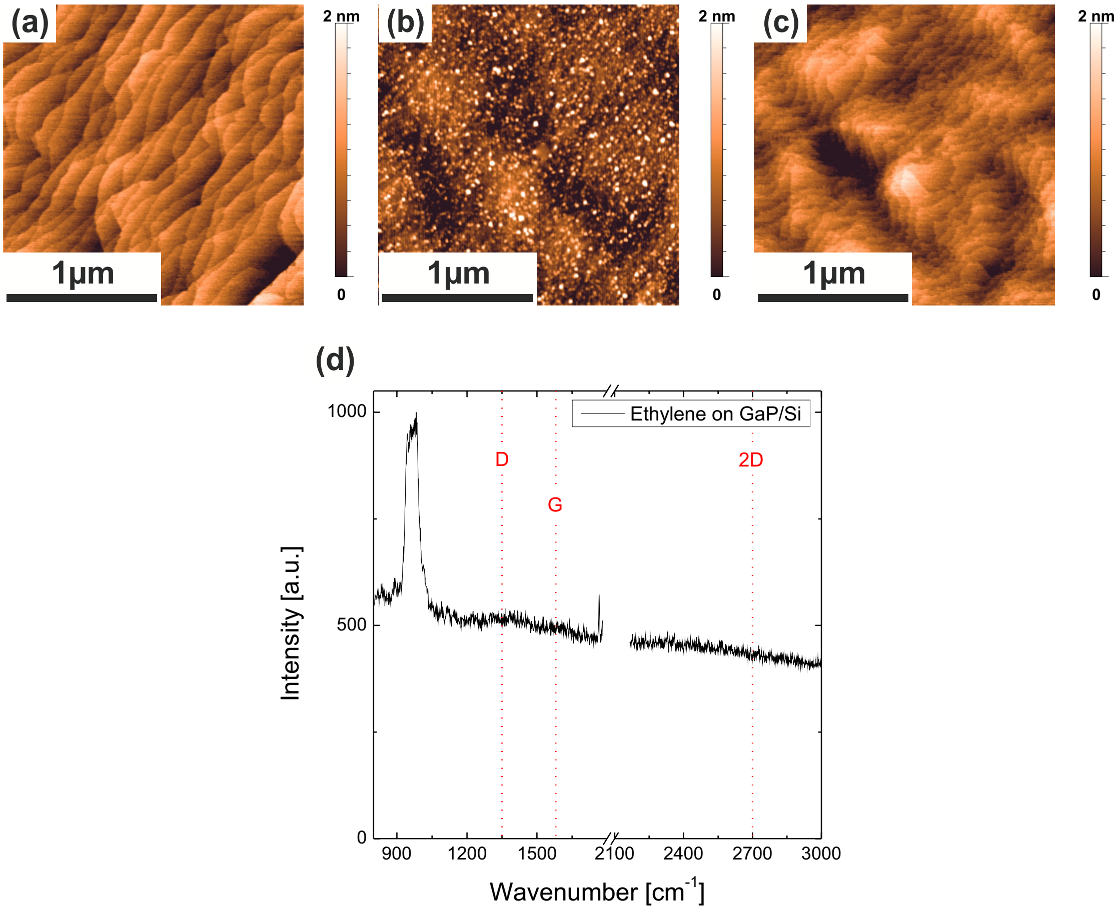

Figure 4.69: AFM images of GaP (001) surfaces after an annealing in N_2 for 5 min at 800 °C (a) or a 5 min deposition of ethylene at 800 °C (b) or 700 °C (c) using N_2 as carrier gas. The Raman spectrum of the sample presented in (b) is displayed in (d).

GaP on Si (001) samples, treated in H_2 atmosphere after the GaP layer growth, are shown in figure 4.69 by means of AFM and Raman measurement. The samples presented in fig. 4.69 (a) and (b) were both prepared at 800 °C using similar growth conditions, but while the reference sample in (a) was only annealed in H_2 for 5 min, for sample (b) ethylene was deposited during this time. While an annealing in nitrogen for 15 min (fig. 4.68 (a)) led to an etching of the GaP surface, an equivalent but shorter annealing for 5 min as shown in fig. 4.69 (b) does not seem to have a significant influence on the surface structure. The GaP surface steps are intact, showing smooth atomic steps. After the ethylene deposition at 800 °C, though, the surface exhibits a significantly increased roughness in comparison to the annealed sample. The GaP surface structure is hardly recognizably any more after this treatment and elevated aggregates appear, as observed before in fig. 4.68 on GaP (001) substrate. This might be due to the deposition of C-containing material. To review this assumption, i.e., to verify whether C was deposited, Raman spectroscopy was performed on this sample. The measured Raman spectrum is presented in image (d). It displays a combination of various measurements taken in different spectral regions. Only the two striking features described before appear in the measurement; the Si-induced peak at around 960 cm^{-1} and the presumably C-O caused peak at approximately 1765 cm^{-1}, which was found for all investigated samples. No additional Raman peaks appear in the spectrum, i.e., no C structures were detected. If C was deposited, the C coverage of the surface might be below a detectable amount. This might especially be the case if the C-containing structures deposited on the surface are amorphous rather than ordered, which would lead to Raman scattering with various energy shifts, depending on the binding types present. No clear peaks, distinguishable from the background, might therefore appear in the spectrum.

A GaP surface after an ethylene depositing at a lower growth temperature of 700 °C is depicted in (c). The deposition was performed for 5 min with an ethylene partial pressure of 1.5 mbar, like for the growth at 800 °C. While after an annealing in nitrogen, even at 800 °C , the GaP surface structure is intact, a deposition of ethylene appears to again lead to an etching process for the conditions applied. While the surface steps are still clearly visible, for this sample the step edges appear considerably roughened in comparison to the sample annealed under N_2. Additionally, no indication for a deposition of material is found. So apparently, no C deposition is possible at lower growth temperatures, i.e., temperatures of 700 °C or below, for the usage of the C precursor ethylene and the chosen growth conditions. The disappearing of indications for C deposition for a T decrease from 800 °C to 700 °C is in accordance with the results on the ethylene deposition using H_2 as carrier gas (fig. 4.67). There, however, no etching was observed. The variance between the two results might be caused by a different ethylene decomposition in H_2 or H_2.

As image 4.69 (b) indicate a deposition of C at 800 °C using the C precursor ethylene and N_2 as carrier gas, but no C signature was found in the Raman spectrum, it is assumed that amorphous C or C hydrogen compounds were deposited instead of ordered material. The growth of ordered C structures might be hindered by two factors. Possibly the ethylene partial pressure and thereby the C deposition rate was too high. The mobility of C on the GaP surface might not be sufficiently high to enable the growth of an ordered layer at this growth rate. Instead, three-dimensional amorphous structures could evolve. Additionally, it is conceivable that too much material was deposited, covering any ordered C structure which might form.

To analyze whether the effects just described occur, the ethylene partial pressure was decreased and the C growth time was varied for the following samples. AFM images of these samples are shown in fig. 4.70.

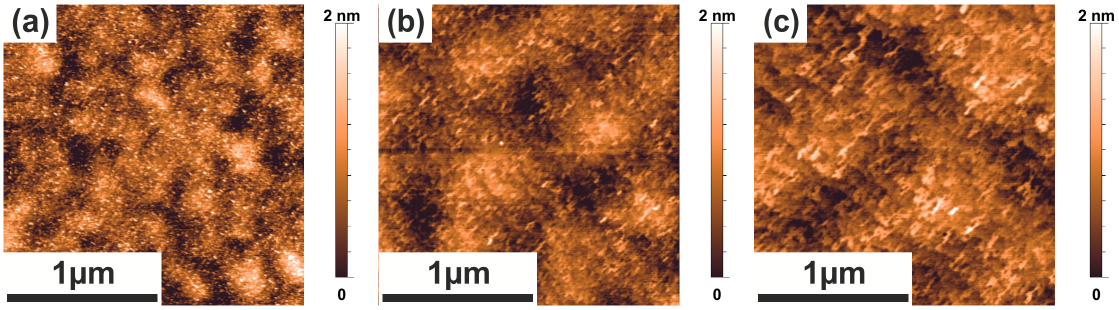

Figure 4.70: AFM images of GaP on Si (001) surfaces after a deposition of ethylene at 800 °C. Starting from a deposition time of 6 min and a partial pressure of 0.5 mbar in (a) the deposition time was decreased by a factor of 2 to 3 min, while the ethylene partial pressure was kept unchanged at 0.5 mbar for the sample (b). Likewise for the sample (c) the ethylene partial pressure was decreased by a factor of 2 to 0.25 mbar compared to (a), while again a deposition time of 6 min was applied.

All images display GaP layers on Si (001) after a deposition of ethylene at 800 °C in N_2 atmosphere. For the sample shown in fig. 4.70 (a) the ethylene partial pressure was reduced by a factor of 3 from 1.5 mbar to 0.5 mbar compared to the sample shown in fig. 4.69 (b), while the growth time was slightly increased to 6 min. For the preparation of the sample presented in (b) only the growth time was then reduced by a factor of two to 3 min in comparison to the time used in (a) keeping the ethylene partial pressure at 0.5 mbar. For the sample (c) the partial pressure was decreased by a factor of 2 to 0.25 mbar while the time was again set to 6 min as used in (a). Comparing image (a) with the sample shown in fig. 4.70 (a) reveals that a reduction of the partial pressure from 1.5 mbar to 0.5 mbar leads to a decrease in the surface roughness. Significantly smaller structures, which additionally exhibit less height, form on the surface. The reduction of the deposition time in (b) or a further reduction of the ethylene partial pressure in (c) seemingly have similar influences on the morphology of the structures forming. For both treatments the GaP surface steps are faintly visible in the AFM image. In addition to the step structure, elongated features dominate the surface. Those structures run perpendicular to the direction of the step edges. Also they are not confined by one terrace, but cut across the step edges. Based on this particular arrangement of the structure, it is assumed that ordered rather than amorphous material appears on the GaP surface after this sample treatment. However, two possible origins for these ordered structures are conceivable. Firstly, again a C enhanced etching process might have occurred during the ethylene deposition, leading to frayed GaP structures on the surface. Secondly, a growth of ordered C structures for the chosen conditions is possible. A growth of ordered carbonic structures, though, should be detectable by Raman measurements, which were therefore performed on these samples.

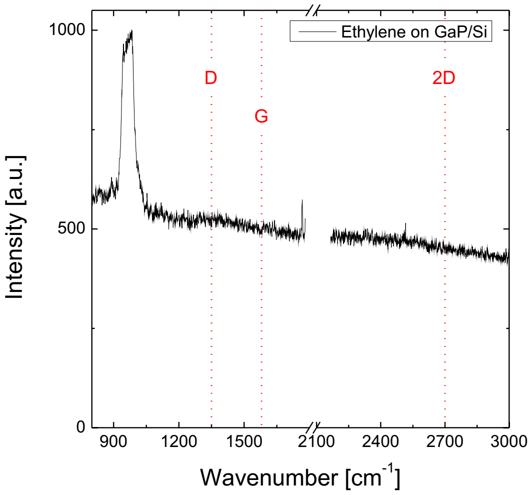

Figure 4.71: Raman spectrum of a GaP layer on Si (001) after 6 min of ethylene deposition at 800 °C in N_2 atmosphere, as shown in fig. 4.70 (c) by means of AFM.

The Raman spectrum for the sample depicted in fig. 4.70 (c) by means of AFM is presented in fig. 4.71. Again a combination of several measurements is shown. As seen before, this spectrum is dominated by the Si originated peak at around 960 cm^{-1} and additionally reveals the always occurring, probably C-O generated, peak at 1765 cm^{-1}. However, no additional peaks indicating the presence of ordered carbonic structures were detected for this sample, as well as for the sample shown in fig. 4.70 (b). Therefore, it can not be assumed that a growth of C occurred here. Rather, it is to be expected that the structures observed by AFM were generated by an etching process of the GaP caused by the ethylene supply.

As observed in section 4.3, a high-temperature treatment of GaP under TBP supply leads to a deposition of a considerable amount of C. This can be explained by the decomposition pathway of TBP and the residual alkyl-groups, which are generated by the decomposition. It was found that TBP mainly decomposes via two reaction pathways generating different alkyl groups, namely isobutane (C_4H_{10}) or isobutene (C_4H_8) [108]. No deposition of P is expected at high temperatures, due to the high volatility of P molecules in this temperature range. The alkyl groups, though, can further decompose at high temperatures via CH_3 abstraction forming C-containing species, such as C_3H_3 or C_3H_5, which can adsorb at the surface [109], [110]. As this approach led to the most convincing deposition of C so far, further investigations were performed and will be discussed in the following. For the sample shown in section 4.3, TBP was offered for 15 min at 800 °C, using a TBP partial pressure of 0.15 mbar. After this treatment a significant C concentration at the surface was found by SIMS measurement (fig 4.30). While Raman spectroscopy revealed the existence of a D and a G band in the spectrum of this sample, indicating the presence of C_6-rings in the deposited C, no 2D band was observed (fig. 4.31). As this feature necessarily occurs in the Raman spectrum of high-quality graphene, it has to be stated that C, which is ordered in form of C_6-ring structures to some extent, but no long-range ordered graphene was deposited by the performed high-temperature treatment. Starting from these results, the growth parameters were varied to study their influence on the deposition of the C structures. Exemplary some samples with different growth conditions will be presented here.

Firstly, the TBP deposition time as well as partial pressure were varied while the growth temperature was kept at 800 °C. AFM and Raman measurements for these samples are presented in fig. 4.72. Image (a) shows the sample already discussed in section 4.3 after 15 min of TBP supply at a partial pressure of 0.15 mbar. For the sample displayed in (b), the TBP partial pressure was increased by a factor of two to 0.3 mbar while the deposition time was kept at 15 min. Two samples with a doubled deposition time of 30 min are shown in (c) and (d). The same TBP partial pressure as for (a) of 0.15 mbar was used for (c), while a partial pressure of 0.30 mbar, as for (b), was used for (d). Although a significant amount of C was deposited (fig 4.30), sample (a) still reveals a rather smooth surface and the GaP surface steps are still slightly recognizable. Due to the increase in the TBP partial pressure shown in (b) the surface roughness rises. Small aggregates form and no step structure is visible any more after this treatment. This trend is even more pronounced for a change in the deposition time, rather than the partial pressure. For a deposition time of 30 min a large number of three-dimensional structures form on the GaP surface for both partial pressures used. However the size of the structures grows with increasing TBP partial pressure. Despite the stabilization with TBP, an intense roughening of the surface with increasing deposition time could occur due to an incongruent evaporation of P at the chosen temperature, resulting in metallic Ga droplets on the surface. However, no enhancement of this evaporation is expected for an increase in the TBP partial pressure offered. Therefore, it is assumed that the structures observed on the surface form due to a deposition of C. This deposition seemingly increases with an increasing TBP partial pressure, even more though with a rising deposition time. To analyze, whether the change in growth parameters realised here also influences the formation of ordered C structures,

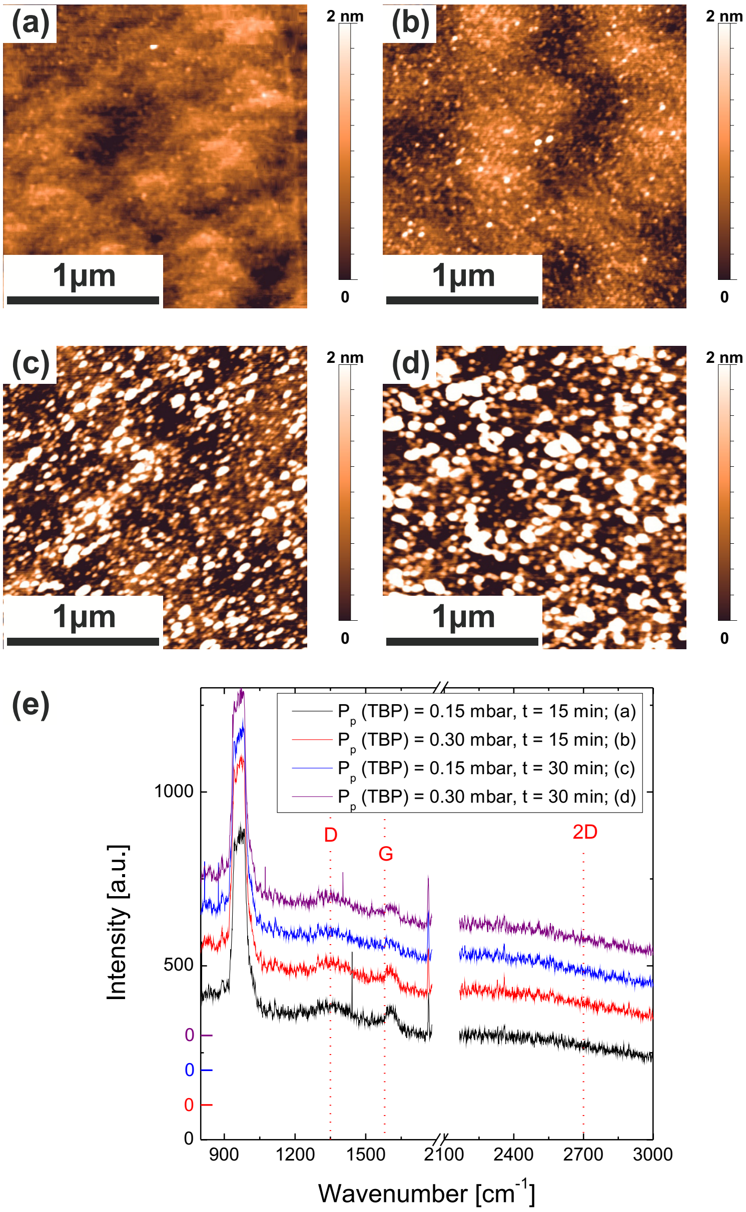

Figure 4.72: AFM micrographs (a)-(d) and Raman spectra (e) of GaP layers on Si (001) after a supply of TBP at 800 °C. Starting from (a) (already shown in fig. 4.31) the TBP partial pressure was increased by a factor of two from 0.15 mbar to 0.3 mbar while the deposition time was kept at 15 min for (b). The deposition time was increased to 30 min and a TBP partial pressure of 0.15 mbar or 0.3 mbar was used for (c) and (d) respectively. The Raman spectra of all these samples are combined in the diagram (e).

Raman spectroscopy was performed. Image 4.72 (e) displays a combination of the Raman spectra for the different samples; the legend displays the connection between each spectrum and the individual AFM micrographs. While variations occur in the Raman spectra of the different samples, a broad D and a G peak, as marked by the red dotted lines, appear for all samples presented. No peak in the region of the 2D band, at around 2700 cm^{-1}, was found in any of the spectra, though. Additionally, besides a shift in the height of the background, which is caused by slight variations in the Raman set-up, as the measurements were performed on different days, small change in the peaks' shapes or heights occur. Although seemingly a larger amount of material is deposited for a longer growth time or higher TBP partial pressure, this variation has no considerable influence on the characteristics of the ordered C structures which form. An additional supply of TBP, however, might not even be necessary for the growth of ordered C, as a significant amount of C is already present on the surface after 15 min of TBP supply at a partial pressure of 0.15 mbar (fig 4.30). Judging from the results presented in fig. 4.72, an additional offer of TBP might only lead to a deposition of amorphous C, which could possibly also hinder a formation of ordered C structures. An ordering might also be possible by surface diffusion of the present C and a formation of new C bonds at suitable conditions. Assumingly, a sufficient surface temperature is necessary for this process. To verify this consideration, various annealings were performed following the high-temperature TBP treatment.

AFM micrographs as well as the combined Raman spectra for samples annealed under various conditions are shown in fig. 4.73 (a)-(c) and (d) respectively. The sample already discussed above and in section 4.3, after 15 min of TBP deposition at 800 °C using a partial pressure of 0.15 mbar, is displayed in image (a) as a reference for the changes caused by an annealing. The samples presented in (b) and (c) were initially treated equally with TBP. However, following the high-temperature TBP treatment sample (b) was annealed in H_2 atmosphere at 800 °C for 30 min, while image (c) shows a sample that was annealed in H_2 for 15 min again at 800 °C. Comparing the three AFM images reveals significant influences of the different annealings on the sample surface. As mentioned before, the as-grown sample (a) exhibits a reasonably flat surface. Only small aggregates formed due to the TBP treatment, nevertheless, the GaP step structure is still indistinctly visible. After the 30 min of annealing in H_2 atmosphere (b) a flat surface is still visible. However, no step structure can be found any more. It was found for a GaP surface (fig. 4.29 (c)) that the step size grows significantly after 15 min of annealing in H_2 at 800 °C in comparison to an as-grown GaP buffer. This effect might also occur for a C containing GaP surface and increase for rising annealing time, as 30 min rather than 15 min of annealing were chosen here. Additionally, the disappearance of the step structure might also be caused by etching, as it was suggested earlier in this section that the treatment of C containing surfaces in H_2 atmosphere might lead to an etching process [107]. The Raman spectrum of this sample, which is represented by the red curve in image (d), also exhibits a broad D as well a G peak, like found for the as-grown sample. Comparing the Raman spectrum for the surface annealed in H_2 atmosphere with the spectrum recorded at the as-grown sample, though, reveals a decrease in the intensity of both peaks. Additionally, again no 2D peak was observed. Seemingly, an annealing in H_2 under the chosen conditions leads to an etching of the C present on the surface. Judging from the Raman measurement, no formation of

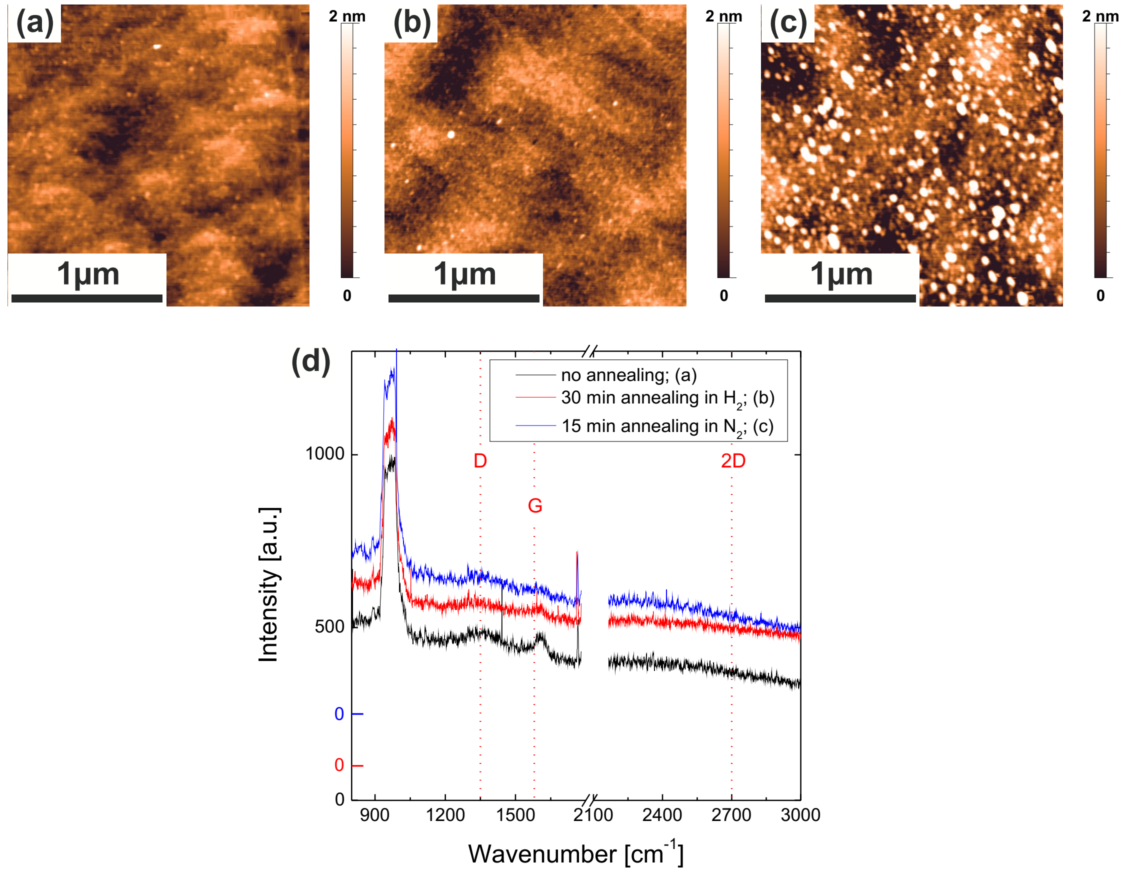

Figure 4.73: AFM (a)-(c) and Raman (d) measurements of a GaP layers on Si (001) after 15 min of TBP supply at 800 °C using a TBP partial pressure of 0.15 mbar. As a reference, no annealing was performed, but the sample was directly cooled down after this treatment for (a) (already shown in fig. 4.31). The other two samples were annealed at 800 °C for 30 min in H_2 (b) or for 15 min in N_2 (c). All Raman spectra of these samples are combined in (d).

long-range ordered graphene-like layers was achieved by this annealing. However, a similar annealing under H_2 using a different reactor pressure or temperature was not tested and might have a different effect.

Caused by the annealing in H_2 for 15 min, shown in image (c), comparatively large, three-dimensional structures form on the GaP surface. Supposedly, those are generated by an merging of material on the surface at the applied conditions. Additionally, a H_2 enhanced etching, as observed in fig. 4.68 (a), might occur, resulting in mobile remains, as e.g. Ga, which could then form the structures observed. No clear statement of the composition of the aggregates, though, can be given by this investigation technique. However, analysing the Raman spectrum of this sample, displayed by the blue curve in image (d), exposes a decrease in the height of the D as well as G peak due to this high-temperature treatment in H_2. Presumably C either desorbs from the surface or previously existing C bonds break during the annealing and amorphous C is generated. Both effects might lead to a reduction of the C-induced Raman signals and more importantly will hinder a formation of graphene. As mentioned before, the growth temperature has an important effect on the formation of ordered C structures, as a sufficient amount of energy must be supplied for the formation of the necessary C bonds. A treatment of GaP surfaces offering TBP at higher temperatures than the 800 °C used before was therefore investigated.

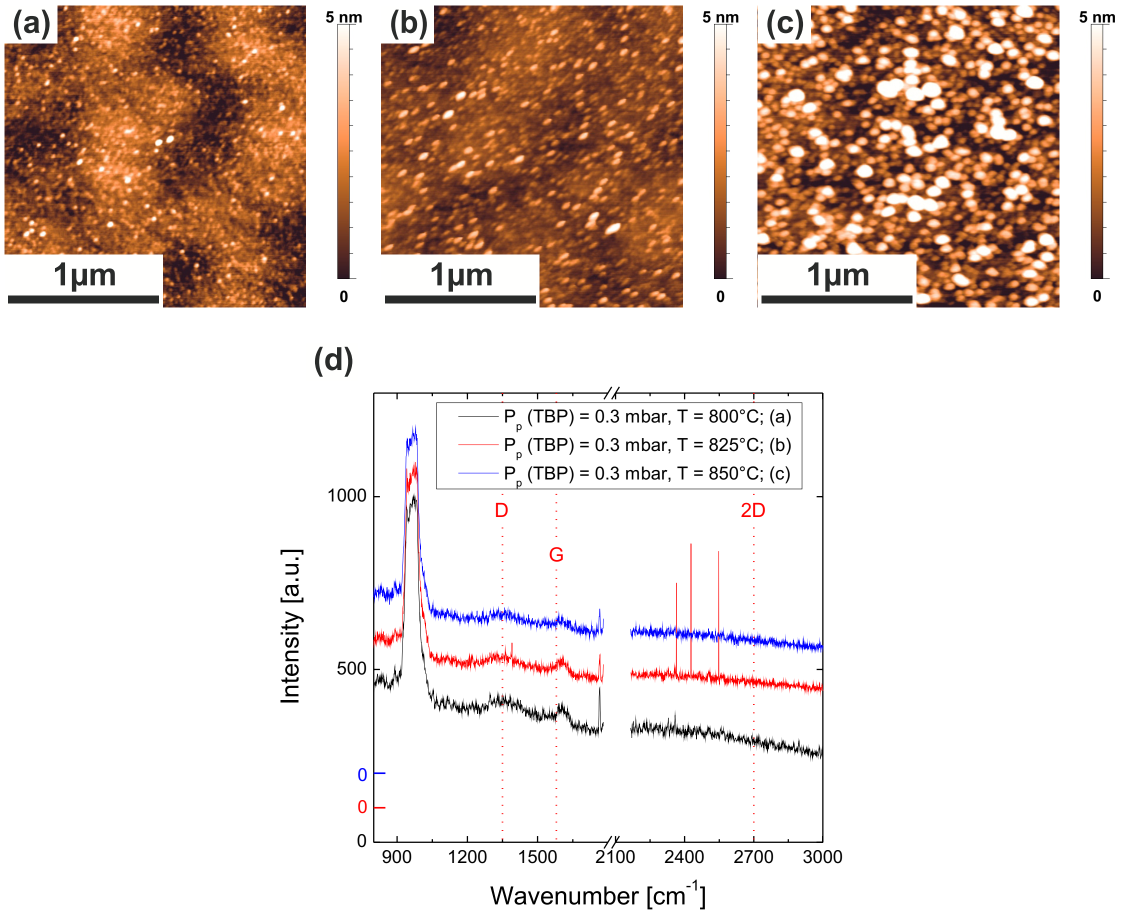

Figure 4.74: AFM micrographs (a)-(c) and Raman spectra (d) recorded on a GaP layer on Si (001) after 15 min of TBP supply at different temperatures. A TBP partial pressure of 0.3 mbar was used for all samples. The deposition temperature was increased from 800 °C used for (a) to 825 °C for (b), and 850 °C for the treatment of sample (c). The Raman measurements for these samples are presented (d), as indicated in the legend.

Samples treated at 825 °C and 850 °C are presented in fig. 4.74 by means of AFM and Raman spectroscopy. A sample prepared at 800 °C supplying TBP for 15 min at a partial pressure of 0.3 mbar is displayed in image (a). The deposition temperature was increased by 25 °C to 825 °C for the samples shown in (b) and again by 25 °C to 850 °C for (c). Aggregates appear on the GaP surface for all treatments. Additionally, the measurements reveal a growth of the size of the structures and an increase of the surface roughness. This roughening and formation of aggregates could occur either by desorption of P or Ga resulting from the high temperature used or by a deposition C-containing material. The Raman spectra (d) exhibits a broad D and a G peak for the TBP deposition at 800 °C and 825 °C , indicating the presence of ordered C structures. For a sample preparation at 850 °C, though, the intensity of those peaks, especially of the G peak, is significantly reduced. The deposition of C or the formation of C bonds might be hindered by the assumed increased evaporation. Presumably, a further increase in deposition temperature will thus not lead a to an increased formation of ordered C structures and was therefore not investigated. Again however, no 2D peak was found in the Raman spectra of these samples, which implies that also at higher temperature no long-range ordered graphene formed.

As a conclusion, it can be stated that a high-temperature treatment of GaP with TBP leads to a deposition of C and to a formation of graphene-like C bonds, as signals from C_6-ring stretching and breathing appear in the Raman spectra of these samples. As no 2D band appeared in the Raman spectrum of any sample yet, no growth of long-range ordered graphene was observed for any of the growth parameters used so far. A strong doping of the C_6-rings by P, which is indicated by the blue shift of the G band, can be an additional reason for the absence of the 2D band. However, as no C_6-rings are expected in the organic residual groups of TBP, this is a first sign for an actual growth of C_6-rings on GaP. A further investigation of the influence of the growth parameters on this formation is necessary to analyze whether graphene with a long-range order can be grown by this approach.

CHAPTER 5

Summary

The present study aimed at the direct deposition of graphene on Si (001) by CVD. CVD growth of graphene is presently performed using transition metal substrates such as Cu. However, to avoid the transfer step, which is necessary for these, it is preferable to realize graphene growth directly on Si (001). Ga, however, is a metal which is commonly used for semiconductor production. Additionally, Ga has also already been shown to have a catalytic effect on the growth of graphene for other growth methods. The deposition of graphene on Si (001) was therefore approached by firstly depositing metallic Ga on a Si surface, which was subsequently treated with a C precursor. A precise understanding of the growth surface and a controlled deposition of Ga is the prerequisite for this growth. This study therefore focussed on examining the growth surface and the deposition of Ga thereon. Si (001) was primarily used as the substrate, but since an intermixing of Ga and Si was observed, which might inhibit metallic Ga from accumulating at the surface, the usage of a GaP interlayer was also studied, to separate the pure Ga from Si. In the final part of this research the deposition of C on Ga-pretreated Si and on GaP/Si (001) templates was investigated.

As a starting point, the surface structure of an epitaxially grown Si buffer on Si (001) was analyzed after a high-temperature annealing at high H_2 pressure, like that used as preparation for most samples in this research. It was found by STM that this treatment results in a formation of primarily D_A Si-steps with remnants of S_B Si-steps. This structure is energetically unfavorable, but presumably originates from a generation, diffusion and annihilation of Si vacancies at the initially existing S_B step edges. This preferential annihilation at S_B step edges might result from the occurrence of broken dimers at this particular step edge, which influences the electronic structure of the surface. Due to a reduced diffusion rate at lower temperatures, this originally unfavorable structure is passivated by the cool-down after annealing.

Ga deposition on Si (001) was examined for two Ga precursors, namely TEGa and TMGa. The results obtained for the respective precursors differ in many aspects from each other due to the different reaction pathways for decomposition and, therefore, the differing residual organic groups. For all utilized conditions Ga etches into Si, forming pyramidal structures. Mounds occur on the surface above these pyramids. The pyramidal structures exhibit boundaries on the Si {111} lattice planes. This is probably due to the greater stability of these planes in comparison to other low index planes. An indication for this is the absence of pyramidal structures for the deposition of Ga on Si (111).

The dimensions of the pyramidal structures and mounds are significantly increased for TMGa deposition, leading to structures with a mean size of approximately 30-60 nm, compared to TEGa deposition, where structures with a mean size of approximately 10-40 nm occur. This might result from an organic layer formed by the residual groups on the Si surface for TEGa deposition. The organic layer only forms for TEGa, since the ethylene rest groups of TEGa can form polyethylene chains, whereas the methyl rest groups of TMGa do not. This layer might restrict the mobility of Ga, which is liquid at growth temperature, leading to a formation of relatively small aggregates.

For both Ga precursors an increase in size of aggregates with a concurrent decrease in their number was found with increasing growth temperature. Additionally, more Ga diffuses into the Si for rising deposition temperature, leading to an increased size of the pyramidal Ga-containing structures. A raise in the partial pressure of the Ga precursor mostly leads to a larger quantity of structures. No clear trend was found for an increase in deposition time, as merging of existing structures competes with developing of new structures. However, it was found that size and number of Ga-containing structures can be tailored by an adjustment of growth temperature, time and Ga partial pressure.

A preferential ordering of Ga aggregates at S_B step edges was observed for low surface coverages. No such preference was found for type A step edges. Like the preferential annihilation of Si vacancies at S_B step edges, this might be caused by a change in the electronic structure at these particular step edges, due to the broken dimers.

Considerable intermixing of Ga and Si was observed for TMGa deposition, resulting in the growth of new crystalline Si structures at the edges of the Ga-containing structures during the sample cool-down. This was not observed for TEGa, but the amount of Si dissolved might merely be too small, due to the considerably smaller size of the pyramidal structures. To prevent this intermixing, which might hinder a catalytic effect of Ga on any graphene growth, a GaP interlayer was grown on Si (001) prior to Ga deposition.

Initially the stability of GaP at high temperatures, which might be necessary for graphene growth, and the GaP growth on Si (001) was examined. It was found that a GaP buffer on GaP (001) as well as a GaP layer on Si (001) remains intact during annealing in H_2 at a reactor pressure of 50 mbar and temperatures up to 800 °C, without a supply of any precursor for stabilization. A formation of large Ga droplets was observed for annealing in H_2 at 950 mbar; incongruent evaporation appears enhanced by a high H_2 pressure.

Earlier studies have shown that a smooth interface and a high-quality growth of GaP on Si (001) is possible when a TBP preflow is applied. The precise processes at the interface, however, had not yet been studied and were therefore analyzed in this study, as a thin

GaP interlayer was used to separate Ga and Si. The usage of a sufficient amount of TBP led to an absence of the Ga-containing aggregates for both Ga precursors. GaP growth at 450 °C, though, only occurred for TBP in combination with TEGa. TBP does not thermally decompose at 450 °C, but only in the presence of a catalyst such as TEGa. TMGa, however, does not have a catalytic effect on the decomposition of TBP. As no Ga structures appear on the Si surface either for TMGa when a TBP preflow is used, it is assumed that the Si surface is covered by a protective layer of TBP after this preflow. A surface coverage of 25 % was determined by STM for a TBP deposition of 1 s at a partial pressure of 0.94 mbar, which corresponds to 1 ML of P, judging from results on GaP growth at equal growth conditions. This is in accordance with the absence of Ga mounds, if a TBP preflow of at least 5 s is used at these conditions. Additionally, it was observed that the TBP molecules preferentially order in rows perpendicular to the dimer rows on the Si (001) surface. The length of these rows increases with increasing TBP partial pressure. This preference is probably due to hydrogen vacancies having a stabilized position on the next-row dimer next to a TBP molecule, constituting a favored adsorption site for further TBP molecules.

Ga deposition on GaP (001) substrate and on GaP on Si (001) was also studied for TEGa and TMGa. As for the deposition on Si, Ga etches into the crystalline substrate and mounds form above these etched formations. The Ga-containing structures arising in the substrate strongly depend on the characteristics of the GaP layer. For thin GaP layers on Si (001), Ga etches through the GaP and reaches the Si, forming pyramidal structures like those observed for the direct deposition on Si. For thicker GaP layers and GaP substrates, less Ga diffuses into the GaP and structures with boundaries on lattice planes with a higher index than {111} form. Additionally, the number of aggregates increases with increasing density of APBs at the surface. Presumably, Ga aggregates preferentially form at anti-phase boundaries, which represent charged defects and therefore a disorder in the electric surface structure. The properties of the Ga-containing structures in terms of size and number resemble those found for TMGa deposition on Si. Unlike for Si, no difference in these properties was observed for TEGa or TMGa. This indicates that no organic layer hindering the Ga mobility is deposited on GaP for either precursor.

Annealing of Ga-pretreated samples in H_2 atmosphere led to a disappearance of the Ga-containing structures at high temperatures, i.e. at a temperature of 800 °C. Annealing at a lower temperature results in a further intermixing of the liquid Ga with the crystalline substrate. While this was observed for Si as well as GaP, a stronger intermixing was observed for Ga with Si. No metallic Ga was observed at the Si (001) surface after annealing, while on GaP metallic Ga is still present after an equivalent treatment. Only samples with a GaP interlayer were therefore used for C deposition.

A supply of C on Ga-pretreated samples led to etching of the initially existing Ga aggregates. This was observed for all C precursors studied, namely TBEthyne, TBEthylene and benzene, and most conditions applied. C deposition was therefore also studied on GaP surfaces without a prior deposition of metallic Ga. Small amounts of C could be deposited at a growth temperature of 800 °C, using the C precursor ethylene and H_2 as carrier gas. This was detected by SIMS measurement. Considerable amounts of material were deposited for the usage of N_2 as carrier gas. However, no signal induced by ordered C was detected by Raman spectroscopy indicating that no sufficient amount of ordered material was deposited. The most successful growth of ordered C structures was achieved by supplying TBP during a high-temperature treatment of GaP, i.e., by a TBP deposition at 800 °C. Considerable amounts of C were detected by SIMS and graphene-induced vibrational bands were found by Raman spectroscopy. No long-range ordered graphene layer was detected yet. However, C containing layers exhibiting sp^2-bonds, which form small scale graphene units to some extent, were deposited for all conditions applied for a high-temperature treatment with TBP supply. As no C_6-ring structures, or even sp^2-bonded C atoms, exist in the TBP molecule, these must have formed during or after deposition. This could be used as a starting point for further investigations of the deposition of long-range ordered graphene on Si (001).

Outlook

A thorough understanding of the growth surface was gained by this study. Additionally, first successes on the deposition of C_6-ring structures on GaP were achieved. This research therefore builds a good foundation for the deposition of graphene on Si (001) using a GaP interlayer. Further studies are necessary and could lead to long-range ordered graphene growth. Therefore, the influence of several growth parameters on this growth should be analyzed.

High-temperature deposition of TBP on GaP appears to be a good approach to the growth of ordered C_6-ring structures. The influence of the growth temperature, growth time and TBP partial pressure should be examined. An annealing at different temperatures or reactor pressures might lead to a diffusion of C on the surface and a formation of C-C bonds.

No values are known for the C solubility in GaP and a diffusion of C into the GaP layer might occur during deposition. A precipitation of C might therefore then occur during cool-down for appropriate conditions. This possible effect and the influence of different cooling rates after C deposition should be studied.

The H_2 partial pressure plays an important role for the decomposition of C precursors as well as for an etching of C off the surface. The influence of the H_2 pressure or the ratio of H_2 and N_2 carrier gas should therefore be investigated.

Additionally, different characterization methods could help to understand the processes occurring for C deposition. STM, especially in combination with X-ray photoelectron spectroscopy, might be used to analyze atomic structures and bonds forming on the surface. Alternatively, tip-enhanced Raman spectroscopy could be applied to gain spatially-resolved information of the vibrational modes of the deposited material.

CHAPTER 6

Zusammenfassung (Summary in German)

Ziel der vorliegenden Arbeit war die direkte chemische Gasphasenabscheidung von Graphen auf Si (001). Heutzutage erfolgt eine derartige Abscheidung von Graphen auf Übergangsmetall-Substraten wie Kupfer. Um den hier notwenigen Transfer zu vermeiden, ist eine direkte Abscheidung auf Si (001) wünschenswert. Gallium wird bereits standardmäßig in der Halbleiterproduktion eingesetzt, und auch ein katalytischer Effekt dieses Metalls auf das Wachstum von Graphen wurde schon für andere Methoden nachgewiesen. Zur Graphen Herstellung auf Si (001) wurde daher folgender Ansatz gewählt. Auf der Si Oberfläche wurde metallisches Ga abgeschieden, anschließend wurde ein C Präkursor angeboten. Die Vorraussetzung für diesen Ansatz ist allerdings eine genaue Kenntnis der Wachtsumsoberfläche und eine kontrollierte Abscheidung des metallischen Ga. Der Fokus dieser Arbeit lag daher auf der Untersuchung der Wachstumsoberfläche und der Abscheidung von Ga auf dieser. Zunächst wurde Si (001) als Substrat verwendet. Hierfür wurde aber eine Durchmischung von Ga und Si festgestellt, welche eine Ansammlung von metallischem Ga auf der Si Oberfläche möglicherweise verhindert. Daher wurde die Verwendung einer GaP Zwischenschicht untersucht, um das elementare Ga von dem Si zu trennen. Abschließend wurde auch die Abscheidung von C auf mit Ga präpariertem Si (001) und auf GaP/Si (001) Templaten untersucht.

Als Ausgangspunkt wurde die Si (001) Oberflächenstruktur nach einem Ausheizen bei hoher Temperatur und hohem H_2 Druck betrachtet, da ein solches Ausheizen für die meisten Proben in dieser Arbeit durchgeführt wurde. Mittels STM wurde festgestellt, dass eine derartige Behandlung zu einer durch D_A Si-Stufen dominierten Oberflächenstruktur mit Überresten von S_B Si-Stufen führt. Zwar ist eine solche Struktur energetisch ungünstig, sie entsteht aber vermutlich durch Erzeugung, Diffusion und Vernichtung von Si Fehlstellen an den ursprünglich vorhandenen S_B Stufenkanten. Eine bevorzugte Vernichtung dieser Fehlstellen an S_B Stufenkanten rührt vermutlich vom Auftreten gebrochener Dimer-Bindungen an diesen Kanten, welche die elektronische Struktur der Oberfläche beeinflussen. Diese eigentlich ungünstige Struktur wird vermutlich durch die verminderte Diffusionsrate beim Abkühlen passiviert.

Die Ga Abscheidung auf Si (001) wurde für die beiden Ga Präkursoren TEGa und TMGa untersucht. Aufgrund der unterschiedlichen Zerlegungswege und der verschiedenen organischen Restgruppen, die daraus resultieren, unterscheiden sich die Ergebnisse für die jeweiligen Präkursoren in vielen Bereichen. Für alle untersuchten Bedingungen ätzt das Ga in das Si, in welchem dadurch pyramidale Strukturen entstehen. Zusätzlich formen sich oberhalb dieser Pyramiden Hügel auf der Oberfläche. Die pyramidalen Strukturen werden durch die Si {111} Kristallebenen begrenzt, was vermutlich durch deren größere Stabilität, im Vergleich zu anderen Kristallebenen mit niedrigen Indizes, begründet ist. Dafür spricht, dass bei der Abscheidung von Ga auf Si (111) keine solchen pyramidalen Strukturen auftreten.

Die Größe der pyramidale Strukturen und Hügel, welche bei der Abscheidung von TEGa etwa 10-40 nm beträgt, ist bei der Verwendung von TMGa mit 40-60 nm deutlich erhöht. Dieser Unterschied lässt sich dadurch erklären, dass bei der Abscheidung von TEGa durch die organischen Restgruppen ein organischer Film auf der Oberfläche gebildet wird. Dieser entsteht nur bei der Verwendung von TEGa, da hier Polyethylen-Ketten durch die Ethylen-Restgruppen entstehen können. Für die Methyl-Restgruppen des TMGa ist dies nicht möglich. Die Mobilität des Ga, welches bei der Abscheidetemperatur flüssig vorliegt, könnte durch diesen Film beeinträchtigt sein, sodass kleinere Strukturen entstehen.

Eine Zunahme der Größe der auf der Oberfläche entstehenden Strukturen bei gleichzeitiger Abnahme ihrer Anzahl wurde mit zunehmender Temperatur für beide Präkursoren beobachtet. Auch diffundiert für höhere Temperaturen mehr Ga in das Si, sodass dort größere pyramidale Strukturen entstehen. Eine Erhöhung des Ga Partialdrucks führt hauptsächlich zu einer steigenden Anzahl an Strukturen. Für eine zunehmende Abscheidezeit konnte keine klare Abhängigkeit gefunden werden, da hier ein Verschmelzen von bestehenden Strukturen mit der Entstehung neuer Strukturen in Konkurrenz steht. Dennoch wurde festgestellt, dass Größe und Anzahl der entstehenden Ga-haltigen Strukturen durch genaue Regelung der Abscheidetemperatur und -zeit sowie des Ga Partialdrucks eingestellt werden können.

Für niedrige Bedeckungen wurde eine bevorzugte Anlagerung von Ga Agglomeraten an den S$_B$ Stufenkanten beobachtet, nicht allerdings an Typ A Stufenkanten. Dies könnte, wie die Vernichtung von Si Fehlstellen, durch die geänderten elektronische Struktur an diesen Kanten bedingt sein.

Für die Abscheidung von TMGa wurde eine deutliche Durchmischung von Ga und Si beobachtet, welche während des Abkühlens zu einem Wachstum von neuen kristallinen Si Formationen an den Rändern der Ga-haltigen Strukturen führte. Für TEGa wurde dies nicht beobachtet. Hier kann aber, aufgrund der deutlich niedrigeren Größe der Ga Strukturen, der Si Anteil lediglich zu gering gewesen sein. Um eine solche Durchmischung, welche sich negativ auf den katalytischen Effekt des Ga auf das Graphen Wachstum auswirken könnte, zu verhindern, wurde eine Zwischenschicht aus GaP vor der Ga Abscheidung auf dem Si aufgebracht.

Dazu wurde zuerst die Stabilität von GaP bei hohen Temperaturen untersucht, da diese für das Graphen Wachstum nötig sein könnten. Es wurde festgestellt, dass sowohl GaP Pufferschichten auf GaP (001) als auch GaP auf Si (001) beim Ausheizen bei einem Reaktordruck von 50 mbar ohne Angebot eines Präkursoren zur Stabilisierung bis zu Temperaturen von 800 °C stabil bleibt. Ausheizen bei einem Reaktordruck von 950 mbar führt allerdings zur Entstehung großer Ga Tropfen; die inkongruente Verdampfung scheint durch einen hohen H_2 Druck verstärkt zu werden.

Frühere Studien zeigten, dass ein Wachstum von qualitativ hochwertigem GaP und glatter Grenzflächen zwischen GaP und Si durch Verwendung eines TBP Vorlaufs möglich ist. Die genauen Abläufe hier wurden allerdings in diesen Studien nicht betrachtet. Da eine dünne GaP Schicht zur Trennung von Si und Ga verwendet wurde, wurden die Abläufe an der Grenzfläche in dieser Arbeit analysiert. Es wurde festgestellt, dass die Verwendung einer ausreichenden TBP Menge für beide Ga Präkursoren zum Verschwinden der Ga-haltigen Agglomerate auf der Oberfläche führte. Eine Herstellung von GaP war bei 450 °C allerdings nur möglich wenn TBP in Verbindung mit TEGa verwendet wurde, nicht für eine Verwendung von TMGa. Bei 450 °C findet keine thermische Zerlegung von TBP statt. Eine Zerlegung ist nur in Anwesenheit eines Katalysators wie TEGa möglich. TMGa hat keinen katalytischen Effekt auf die Zerlegung von TBP. Da allerdings auch für TMGa keine Ga-haltigen Strukturen auf der Oberfläche entstehen, wenn ein TBP Vorlauf verwendet wird, ist davon auszugehen, dass eine schützende molekulare TBP Schicht auf der Oberfläche entsteht. Mittels STM wurde eine Oberflächenbedeckung von 25% für eine TBP Abscheidung von 1 s bei einem Partialdruck von 0.94 mbar festgestellt. Dabei entspricht die abgeschiedene TBP Menge 1 ML P, ausgehend von Ergebnissen für die GaP Abscheidung auf Si bei entsprechenden Bedingungen. Dieses Ergebnis stimmt mit der Tatsache überein, dass nach einem 5 sekündigen TBP Vorlauf keine Ga-haltigen Strukturen mehr gefunden wurden. Zusätzlich wurde beobachtet, dass sich die TBP Moleküle bevorzugt in Reihen senkrecht zu den Si Dimerreihen anordnen, wobei die durchschnittliche Reihenlänge mit Erhöhung des verwendeten TBP Partialdrucks ansteigt. Diese bevorzugte Anordnung lässt sich vermutlich durch H-Fehlstellen erklären, die stabile Positionen auf neben liegenden Dimeren in der benachbarten Reihe eines gebundenen TBP Moleküls besitzen. Solche H Fehlstellen dienen als bevorzugte Anlagerungsstelle für ein weiteres TBP Molekül.

Auch auf GaP (001) Substrat und auf GaP auf Si (001) wurde die Abscheidung von TEGa und TMGa untersucht. Auch hier ätzt das Ga in das kristalline Substrat und es entstehen Hügel auf der Oberfläche, wie bereits für Si beobachtet. Die Charakteristik der Ga-haltigen Strukturen hängen stark von den Eigenschaften der GaP Schicht ab. Für dünne GaP Schichten auf Si ätzt das Ga durch das GaP und erreicht das Si. Hier entstehen pyramidale Strukturen, die denen auf dem Si Substrat entsprechen. Für dicke GaP Schichten oder GaP Substrat entstehen Strukturen, deren Grenzflächen auf Kristallebenen mit höheren Indizes als {111} liegen. Zudem steigt die Zahl der entstehenden Strukturen mit der Dichte der Antiphasengrenzen, da sich Ga bevorzugt an diesen anlagert. Antiphasengrenzen stellen geladene Defekte und damit Störungen der elektronischen Struktur der Oberfläche dar. Die Eigenschaften der auf der GaP Oberfläche entstehenden Ga Strukturen ähnelt denen, die bei der Abscheidung von TMGa auf Si beobachtet wurden. Anders als bei Si wurde hier kein Unterschied zwischen den mit TEGa und den mit TMGa abgeschiedene Strukturen festgestellt. Vermutlich entsteht auf GaP keine organische Schicht, welche die Mobilität des Ga behindert.

Wurden die mit Ga vorbehandelten Proben bei hohen Temperaturen, d.h. bei 800 °C, ausgeheizt, so wurde hinterher kein Ga mehr an der Oberfläche gefunden. Ein Ausheizen bei tieferen Temperaturen führte zu einer verstärkten Vermischung des Ga mit dem kristallinen Substrat. Dies wurde sowohl für Si als auch für GaP beobachtet, hatte aber für Si stärkere Auswirkungen. Hier wurde nach dem Ausheizen kein metallisches Ga mehr gefunden, auf GaP war dieses allerdings noch vorhanden. Aus diesem Grund wurden nur Proben mit einer GaP Zwischenschicht mit C behandelt.

Für die mit Ga vorbehandelten Proben führte eine Behandlung mit C zum Ätzten der ursprünglich vorhandenen Ga Agglomerate. Dieses wurde für sämtliche verwendeten C Präkursoren, also TBEthylen, TBEthen und Benzen, und für fast alle Bedingungen beobachtet. Daher wurde die C Abscheidung auf GaP ohne vorherige Abscheidung von metallischem Ga untersucht. Unter Verwendung des C Präkursors Ethen und des Trägergases H_2 konnten hier bei einer Abscheidetemperatur von 800 °C kleine Mengen C aufgebracht werden, welche per SIMS detektiert wurden. Unter Verwendung des Trägergases N_2 konnten deutliche Mengen abgeschieden werden. Für keine der Proben konnten aber Raman Signale gefunden werden, die von geordnetem C ausgingen. Es ist also davon auszugehen, dass keine Schicht mit langreichweitiger Ordnung abgeschieden wurde. Die erfolgreichste Abscheidung von geordneten C Strukturen wurde durch eine Angebot von TBP bei hoher Temperatur erzielt, genauer durch eine TBP Abscheidung auf GaP bei 800 °C. Hierfür wurden sowohl deutlich C Mengen durch SIMS, als auch Vibrationszustände von Graphen mittels Raman Spektroskopie detektiert. Zwar wurde bisher keine Graphenschicht mit langreichweitiger Ordnung gefunden, für alle TBP Behandlungen bei hohen Temperaturen wurden allerdings C-haltige Schichten abgeschieden, sp^2-Bindungen aufwiesen, die zu einem gewissen Anteil in kleine Graphen Einheiten geordent waren. Da keine C_6-Ringe, oder auch nur sp^2-Bindungen, im TBP Molekül vorkommen, müssen sie während oder nach der Abscheidung auf der Oberfläche entstehen. Dies stellt einen guten Ausgangspunkt für weitere Untersuchung zur Abscheidung von Graphen mit langreichweitiger Ordnung auf Si (001) dar.

Ausblick

Durch diese Studie wurde ein genaues Verständnis der Wachstumsoberfläche gewonnen. Zusätzlich konnten erste Erfolge bei der Abscheidung von C_6-Ring Strukturen auf GaP erzielt werden. Diese Arbeit stellt daher eine gute Grundlage für die Abscheidung von Graphen auf einer GaP Zwischenschicht auf Si (001) dar. Weitere Studien dazu sind nötig und können zu einem Wachstum von Graphen mit langreichweitiger Ordnung führen. Um dieses zu erreichen sollte der Einfluss verschiedener Abscheideparameter auf das Wachstum untersucht werden.

Die Abscheidung von TBP auf GaP bei hohen Temperaturen erscheint als sinnvoller Ansatz zum Wachstum von geordneten C Schichten. Hierfür sollte der Einfluss von Abscheidetemperatur und -zeit sowie des TBP Partialdrucks betrachtet werden. Ein Ausheizen bei unterschiedlichen Temperaturen oder Reaktordrücken kann zur Diffusion des C auf der Oberfläche und zum Entstehen von C-C Bindungen führen.

Die C Löslichkeit in GaP ist nicht bekannt und C könnte während der Abscheidung in das GaP diffundieren. Während des Abkühlens könnte eine Ausfällung dieses C stattfinden. Daher sollte das mögliche Auftreten dieses Effektes und der Einfluss verschiedener Kühlraten untersucht werden.

Der H_2 Partialdruck hat einen wichtigen Einfluss auf die Zerlegung der C Moleküle, aber auch auf ein Ätzen des C von der Oberfläche. Daher sollte auch der Einfluss des H_2 Drucks, beziehungsweise der Einfluss des Verhältnisses von H_2 zu N_2 Trägergas beobachtet werden.

Zusätzlich sollten weitere Charakterisierungsmethoden verwendet werden, um die bei der C Abscheidung stattfindenden Prozesse besser zu verstehen. Mittels STM können, besonders in Verbindung mit Röntgenphotoelektronenspektroskopie, die atomaren Strukturen auf der Oberfläche sowie die entstehenden Bindungen untersucht werden. Alternativ kann hier auch spitzenverstärkte Raman Spektroskopie verwendet werden um ortsaufgelöste Informationen über die Vibrationszustände des abgeschiedenen Materials zu erhalten.

Bibliography

[1] K. S. Novoselov et al.. 'Electric Field Effect in Atomically Thin Carbon Films.' *Science* **306, 5696**: 666 (2004)

[2] K. S. Novoselov. 'Nobel Lecture: Graphene: Materials in the Flatland.' *Reviews of Modern Physics* **83, 3**: 837 (2011)

[3] A. C. Ferrari et al.. 'Science and technology roadmap for graphene, related two-dimensional crystals, and hybrid systems.' *Nanoscale* **7, 11**: 4598 (2015)

[4] A. H. Castro Neto et al.. 'The electronic properties of graphene.' *Reviews of Modern Physics* **81, 1**: 109 (2009)

[5] K. S. Novoselov et al.. 'Two-dimensional gas of massless Dirac fermions in graphene.' *Nature* **438, 7065**: 197 (2005)

[6] L. Wang et al.. 'One-Dimensional Electrical Contact to a Two-Dimensional Material.' *Science* **342, 6158**: 614 (2013)

[7] S. S. Li and W. R. Thurber. 'The dopant density and temperature dependence of electron mobility and resistivity in n-type silicon.' *Solid-State Electronics* **20, 7**: 609 (1977)

[8] A. Zurutuza and C. Marinelli. 'Challenges and opportunities in graphene commercialization.' *Nature Nanotechnology* **9, 10**: 730 (2014)

[9] J. Wang et al.. 'High-mobility graphene on liquid p-block elements by ultra-low-loss CVD growth.' *Scientific Reports* **3** (2013)

[10] H. Ishikawa et al.. 'Thermal stability of GaN on (111) Si substrate.' *Journal of Crystal Growth* **189-190**: 178 (1998)

[11] M. Grundmann. *The Physics of Semiconductors. An Introduction Including Nanophysics and Applications.* Springer-Verlag Berlin Heidelberg (2010)

[12] G. B. Stringfellow. *Organometallic Vapour-Phase Epitaxy: Theory and Practice.* Academic Press (1999)

[13] Z. R. Robinson et al.. ‘Chemical Vapor Deposition of Two-Dimensional Crystals.’ In T. F. Kuech (Editor), ‘Handbook of Crystal Growth,’ 785–833. Elsevier (2015)

[14] Prentice-Hall Inc., ‘sp2 Hybrid Orbitals.’, `http://wps.prenhall.com/wps/media/objects/724/741576/chapter\_01.html`, 2015-07-16

[15] C. Riedl et al.. ‘Structural and electronic properties of epitaxial graphene on SiC(0001): a review of growth, characterization, transfer doping and hydrogen intercalation.’ *Journal of Physics D: Applied Physics* **43, 37**: 374009 (2010)

[16] A. K. Geim. ‘Graphene: Status and Prospects.’ *Science* **324, 5934**: 1530 (2009)

[17] Q. Zhao et al.. ‘Ultimate strength of carbon nanotubes: A theoretical study.’ *Physical Review B* **65, 14**: 144105 (2002)

[18] F. Liu et al.. ‘Ab initio calculation of ideal strength and phonon instability of graphene under tension.’ *Physical Review B* **76, 6**: 064120 (2007)

[19] C. Lee et al.. ‘Measurement of the Elastic Properties and Intrinsic Strength of Monolayer Graphene.’ *Science* **321, 5887**: 385 (2008)

[20] R. Van Noorden. ‘Chemistry: The trials of new carbon.’ *Nature* **469, 7328**: 14 (2011)

[21] P. R. Wallace. ‘The band theory of graphite.’ *Physical Review* **71, 9**: 622 (1947)

[22] a. K. Geim and K. S. Novoselov. ‘The rise of graphene.’ *Nature materials* **6, 3**: 183 (2007)

[23] a. C. Ferrari et al.. ‘Raman Spectrum of Graphene and Graphene Layers.’ *Physical Review Letters* **97, 18**: 187401 (2006)

[24] A. Gupta et al.. ‘Raman Scattering from High-Frequency Phonons in Supported n -Graphene Layer Films.’ *Nano Letters* **6, 12**: 2667 (2006)

[25] TU München, ‘Raman-Spektroskopie.’, `http://www.sces.ph.tum.de/fileadmin/w00bfe/www/content\_uploads/12\_Raman-Spektroskopie.pptx.`, 2015-07-19

[26] R. Beams et al.. ‘Raman characterization of defects and dopants in graphene.’ *Journal of Physics: Condensed Matter* **27, 8**: 083002 (2015)

[27] B. Müller. ‘Herstellung und Charakterisierung von epitaktischem Graphen auf präparierten Si(001)-Oberflächen.’ Diploma thesis, Philipps-Universität Marburg (2011)

[28] Moorfield Nanotechnology, ‘Graphene Produced Using nanoCVD Systems.’, `http://www.nanocvd.co.uk/graphene\_material\_nanoCVD.html`, 2015-07-21

[29] A. Jorio. ‘Raman Spectroscopy in Graphene-Based Systems: Prototypes for Nanoscience and Nanometrology.’ *ISRN Nanotechnology* **2012**: 1 (2012)

[30] M. A. Tamor and W. C. Vassell. ‘Raman "fingerprinting" of amorphous carbon films.’ *Journal of Applied Physics* **76, 6**: 3823 (1994)

[31] R. E. Peierls. ‘Quelques proprietes typiques des corpses solides.’ *Ann. I. H. Poincare* **5**: 177 (1935)

[32] L. Landau. ‘Zur Theorie der phasenumwandlungen II.’ *Phys. Z. Sowjetunion* **11**: 26 (1937)

[33] P. Sutter. ‘Epitaxial graphene: How silicon leaves the scene.’ *Nature Materials* **8, 3**: 171 (2009)

[34] X. Li et al.. ‘Large-area synthesis of high-quality and uniform graphene films on copper foils.’ *Science (New York, N.Y.)* **324, 5932**: 1312 (2009)

[35] S. Bae et al.. ‘Roll-to-roll production of 30-inch graphene films for transparent electrodes.’ *Nature Nanotechnology* **5, 8**: 574 (2010)

[36] C. Mattevi et al.. ‘A review of chemical vapour deposition of graphene on copper.’ *J. Mater. Chem.* **21, 10**: 3324 (2011)

[37] A. Obraztsov et al.. ‘Chemical vapor deposition of thin graphite films of nanometer thickness.’ *Carbon* **45, 10**: 2017 (2007)

[38] Q. Yu et al.. ‘Graphene segregated on Ni surfaces and transferred to insulators.’ *Applied Physics Letters* **93, 11**: 113103 (2008)

[39] L. Huang et al.. ‘Synthesis of high-quality graphene films on nickel foils by rapid thermal chemical vapor deposition.’ *Carbon* **50, 2**: 551 (2012)

[40] P. W. Sutter et al.. ‘Epitaxial graphene on ruthenium.’ *Nature materials* **7, 5**: 406 (2008)

[41] L. Jin et al.. ‘Tailoring the Growth of Graphene on Ru(0001) via Engineering of the Substrate Surface.’ *The Journal of Physical Chemistry C* **116, 4**: 2988 (2012)

[42] P. Sutter et al.. ‘Graphene on Pt(111): Growth and substrate interaction.’ *Physical Review B* **80, 24**: 245411 (2009)

[43] G. W. Cushing et al.. ‘Graphene Growth on Pt(111) by Ethylene Chemical Vapor Deposition at Surface Temperatures near 1000 K.’ *The Journal of Physical Chemistry C* **119, 9**: 4759 (2015)

[44] S. M. Wang et al.. ‘Synthesis of graphene on a polycrystalline Co film by radio-frequency plasma-enhanced chemical vapour deposition.’ *Journal of Physics D: Applied Physics* **43, 45**: 455402 (2010)

[45] E. Kim et al.. ‘Growth of Few-Layer Graphene on a Thin Cobalt Film on a Si/SiO2 Substrate.’ *Chemical Vapor Deposition* **17, 1-3**: 9 (2011)

[46] S. Marchini et al.. ‘Scanning tunneling microscopy of graphene on Ru(0001).’ *Physical Review B* **76, 7**: 075429 (2007)

[47] X. Li et al.. ‘Evolution of Graphene Growth on Ni and Cu by Carbon Isotope Labeling.’ *Nano Letters* **9, 12**: 4268 (2009)

[48] K. Natesan and T. F. Kassner. ‘Thermodynamics of carbon in nickel, iron-nickel and iron-chromium-nickel alloys.’ *Metallurgical Transactions* **4, 11**: 2557 (1973)

[49] W. J. Arnoult and R. B. McLellan. ‘The solubility of carbon in rhodium ruthenium, iridium and rhenium.’ *Scripta Metallurgica* **6, 10**: 1013 (1972)

[50] R. Siller et al.. ‘The solubility of carbon in palladium and platinum.’ *Journal of the Less Common Metals* **16, 1**: 71 (1968)

[51] G. López and E. Mittemeijer. ‘The solubility of C in solid Cu.’ *Scripta Materialia* **51, 1**: 1 (2004)

[52] J. M. Wofford et al.. ‘Graphene Islands on Cu Foils: The Interplay between Shape, Orientation, and Defects.’ *Nano Letters* **10, 12**: 4890 (2010)

[53] P. A. Khomyakov et al.. ‘First-principles study of the interaction and charge transfer between graphene and metals.’ *Physical Review B* **79, 19**: 195425 (2009)

[54] F. Mittendorfer et al.. ‘Graphene on Ni(111): Strong interaction and weak adsorption.’ *Physical Review B* **84, 20**: 201401 (2011)

[55] J. Lahiri et al.. ‘Graphene growth and stability at nickel surfaces.’ *New Journal of Physics* **13, 2**: 025001 (2011)

[56] M. Xu et al.. ‘Single-layer Graphene Nearly 100% Covering an Entire Substrate.’ *Technical report* (2010)

[57] B. C. Banerjee et al.. ‘Pyrolytic Carbon Formation from Carbon Suboxide.’ *Nature* **192, 4801**: 450 (1961)

[58] A. E. Karu and M. Beer. ‘Pyrolytic Formation of Highly Crystalline Graphite Films.’ *Journal of Applied Physics* **37, 5**: 2179 (1966)

[59] K. Takahashi et al.. 'In situ scanning electron microscopy of graphene growth on polycrystalline Ni substrate.' *Surface Science* **606, 7-8**: 728 (2012)

[60] J. Lahiri et al.. 'Graphene Growth on Ni(111) by Transformation of a Surface Carbide.' *Nano Letters* **11, 2**: 518 (2011)

[61] A. Kumar and H. C. Lee. 'Synthesis and Biomedical Applications of Graphene: Present and Future Trends.' In 'Advances in Graphene Science,' InTech (2013)

[62] X. Li et al.. 'Large-Area Graphene Single Crystals Grown by Low-Pressure Chemical Vapor Deposition of Methane on Copper.' *Journal of the American Chemical Society* **133, 9**: 2816 (2011)

[63] I. Vlassiouk et al.. 'Role of Hydrogen in Chemical Vapor Deposition Growth of Large Single-Crystal Graphene.' *ACS Nano* **5, 7**: 6069 (2011)

[64] W. Zhang et al.. 'First-Principles Thermodynamics of Graphene Growth on Cu Surfaces.' *The Journal of Physical Chemistry C* **115, 36**: 17782 (2011)

[65] C. B. Duke. 'Semiconductor Surface Reconstruction: The Structural Chemistry of Two-Dimensional Surface Compounds.' *Chemical Reviews* **96, 4**: 1237 (1996)

[66] 'WWW Picture gallery based on in the Surface Structure Database (SSD, NIST Standard Reference Database 42) by P. R. Watson, M. A. Van Hove, K. Hermann. The pictures have been prepared from SSD output and postprocessed with BALSAC by K. Hermann.'

[67] T. Tabata et al.. 'Order-disorder transition on Si(001): c(4×2) to (2×1).' *Surface Science* **179, 1**: L63 (1987)

[68] P. C. Weakliem et al.. 'Subpicosecond interconversion of buckled and symmetric dimers on Si(100).' *Surface Science* **232, 3**: L219 (1990)

[69] R. A. Wolkow. 'Direct observation of an increase in buckled dimers on Si(001) at low temperature.' *Physical Review Letters* **68, 17**: 2636 (1992)

[70] M. Dürr and U. Höfer. 'Hydrogen diffusion on silicon surfaces.' *Progress in Surface Science* **88, 1**: 61 (2013)

[71] G. Mette. 'Untersuchungen zur selektiven Reaktivität von Ethen, Cyclooctin und Tetrahydrofuran mit Si(001)-Oberflächen.' PhD thesis, Philipps-Universität Marburg (2012)

[72] J. J. Boland. 'Structure of the H-saturated Si(100) surface.' *Physical Review Letters* **65, 26**: 3325 (1990)

[73] J. E. Northrup. ‘Structure of Si(100)H: Dependence on the H chemical potential.’ *Physical Review B* **44, 3**: 1419 (1991)

[74] D. J. Chadi. ‘Stabilities of single-layer and bilayer steps on Si(001) surfaces.’ *Physical Review Letters* **59, 15**: 1691 (1987)

[75] B. S. Swartzentruber. ‘Scanning tunneling microscopy studies of structural disorder and steps on Si surfaces.’ *Journal of Vacuum Science & Technology A: Vacuum, Surfaces, and Films* **7, 4**: 2901 (1989)

[76] F. Reboredo et al.. ‘Hydrogen-induced instability on the flat Si(001) surface via steric repulsion.’ *Physical Review B* **63, 12** (2001)

[77] T. Roesener et al.. ‘MOVPE Growth of III-V Solar Cells on Silicon in 300 mm Closed Coupled Showerhead Reactor.’ In ‘EU PVSEC Proceedings,’ 964–968. Valencia (2010)

[78] A. Ishizaka and Y. Shiraki. ‘Low temperature surface cleaning of silicon and its application to silicon MBE.’ *Journal of the Electrochemical Society* **133, 4**: 666 (1986)

[79] Universität Regensburg, AG Prof. Gießibl, ‘Raster-Tunnel-Mikroskopie.’, `http://www.uni-regensburg.de/physik/giessibl/forschung/methoden/index.html`, 2015-07-31

[80] I. Németh et al.. ‘Heteroepitaxy of GaP on Si: Correlation of morphology, anti-phase-domain structure and MOVPE growth conditions.’ *Journal of Crystal Growth* **310, 7-9**: 1595 (2008)

[81] K. Volz et al.. ‘GaP-nucleation on exact Si (001) substrates for III/V device integration.’ *Journal of Crystal Growth* **315, 1**: 37 (2011)

[82] A. Beyer et al.. ‘GaP heteroepitaxy on Si(001): Correlation of Si-surface structure, GaP growth conditions, and Si-III/V interface structure.’ *Journal of Applied Physics* **111, 8**: 083534 (2012)

[83] S. Brückner et al.. ‘Anomalous double-layer step formation on Si(100) in hydrogen process ambient.’ *Physical Review B - Condensed Matter and Materials Physics* **86, 19** (2012)

[84] S. Brückner et al.. ‘Domain-sensitive in situ observation of layer-by-layer removal at Si(100) in H2 ambient.’ *New Journal of Physics* **15** (2013)

[85] P. Bedrossian and T. Klitsner. ‘Anisotropic vacancy kinetics and single-domain stabilization on Si(100)-2x1.’ *Physical Review Letters* **68, 5**: 646 (1992)

[86] T. W. Poon et al.. ‘Ledge interactions and stress relaxations on Si(001) stepped surfaces.’ *Physical Review B* **45, 7**: 3521 (1992)

[87] P. Thanh Trung et al.. ‘Direct growth of graphitic carbon on Si(111).’ *Applied Physics Letters* **102, 1**: 013118 (2013)

[88] J.-H. Lee et al.. ‘Wafer-scale growth of single-crystal monolayer graphene on reusable hydrogen-terminated germanium.’ *Science (New York, N.Y.)* **344, 6181**: 286 (2014)

[89] Z. W. Pan et al.. ‘Gallium-mediated growth of multiwall carbon nanotubes.’ *Applied Physics Letters* **82, 12**: 1947 (2003)

[90] K. Werner et al.. ‘Structural characteristics of gallium metal deposited on Si (001) by MOCVD.’ *Journal of Crystal Growth* **405**: 102 (2014)

[91] A. Beyer et al.. ‘Pyramidal Structure Formation at the Interface between III/V Semiconductors and Silicon.’ *submitted*

[92] M. Zinke-Allmang et al.. ‘Role of Ostwald ripening in islanding processes.’ *Applied Physics Letters* **51, 13**: 975 (1987)

[93] P. H. Keck and J. Broder. ‘The solubility of silicon and germanium in gallium and indium.’ *Physical Review* **90, 4**: 521 (1953)

[94] A. Dadgar et al.. ‘MOVPE growth of GaN on Si(111) substrates.’ *Journal of Crystal Growth* **248**: 556 (2003)

[95] R. Lin. ‘The decomposition of triethylgallium on Si(100).’ *Journal of Vacuum Science & Technology B: Microelectronics and Nanometer Structures* **7, 4**: 725 (1989)

[96] T. Kuech et al.. ‘The influence of growth chemistry on the MOVPE growth of GaAs and $\mathrm{Al_xGa_{(1\text{-}x)}As}$ layers and heterostructures.’ *Journal of Crystal Growth* **77, 1-3**: 257 (1986)

[97] P. W. Lee et al.. ‘In situ mass spectroscopy and thermogravimetric studies of GaAs MOCVD gas phase and surface reactions.’ *Journal of Crystal Growth* **85, 1-2**: 165 (1987)

[98] P. A. Temple and C. E. Hathaway. ‘Multiphonon Raman spectrum of silicon.’ *Physical Review B* **7, 8**: 3685 (1973)

[99] K. Yamane et al.. ‘Growth of pit-free GaP on Si by suppression of a surface reaction at an initial growth stage.’ *Journal of Crystal Growth* **311, 3**: 794 (2009)

[100] T. J. Grassman et al.. ‘Nucleation-related defect-free GaP/Si(100) heteroepitaxy via metal-organic chemical vapor deposition.’ *Applied Physics Letters* **102, 14**: 142102 (2013)

[101] M. Morita et al.. 'Growth of native oxide on a silicon surface.' *Journal of Applied Physics* **68, 3**: 1272 (1990)

[102] A. Stegmüller et al.. 'A quantum chemical study on gas phase decomposition pathways of triethylgallane (TEG, Ga(C2H5)3) and tert-butylphosphine (TBP, PH2(t-C4H9)) under MOVPE conditions.' *Physical chemistry chemical physics : PCCP* **16, 32**: 17018 (2014)

[103] A. Stegmüller. 'Description of Gallium Phosphide Epitaxy Growth by Computational Chemistry.' PhD thesis, Philipps-Universität Marburg (2015)

[104] G. Wang et al.. 'Direct Growth of Graphene Film on Germanium Substrate.' *Scientific Reports* **3** (2013)

[105] R. Addou et al.. 'Monolayer graphene growth on Ni(111) by low temperature chemical vapor deposition.' *Applied Physics Letters* **100, 2** (2012)

[106] T. A. Land et al.. 'STM investigation of single layer graphite structures produced on Pt (111) by hydrocarbon decomposition.' *Surf* **264**: 261 (1992)

[107] H. J. Park et al.. 'Growth and properties of few-layer graphene prepared by chemical vapor deposition.' *Carbon* **48, 4**: 1088 (2010)

[108] G. B. Stringfellow. 'Non-hydride group V sources for OMVPE.' *Journal of Electronic Materials* **17, 4**: 327 (1988)

[109] R. S. Konar et al.. 'The initiation of chains in the pyrolysis of isobutane.' *Journal of the Chemical Society A: Inorganic, Physical, Theoretical* 1543 (1967)

[110] J.-H. Oh et al.. 'Metalorganic molecular beam epitaxy of heavily carbon-doped InP using tertiarybutylphosphine as a carbon auto-doping source.' *Applied Physics Letters* **66, 21**: 2891 (1995)

List of Figures

Dictionary of presented samples

Following samples were displayed in the individual figures in chapter 4:

Figure 4.1: # 17213

Figure 4.2: # 17213

Figure 4.3: # 17359

Figure 4.4: # 17102

Figure 4.5: # 17102; # 17278

Figure 4.6: # 17278

Figure 4.7: # 16944; # 16945; # 16946; # 16951; # 16959;

Figure 4.8: # 16944; # 16945; # 16946; # 16951; # 16959;

Figure 4.9: # 16944; # 16945; # 16946; # 17205; # 17209

Figure 4.10: # 16944; # 16945; # 16946; # 17205; # 17209

Figure 4.11: # 17102; # 17209

Figure 4.12: # 17206; # 17207; # 17209; # 17210

Figure 4.13: # 17209; # 17210

Figure 4.14: # 17102; # 17902

Figure 4.15: # 16945; # 16951; # 17204; # 17205; # 17207; # 17210; # 17902

Figure 4.16: # 17363; # 17364; # 17365

Figure 4.17: # 17687

Figure 4.18: # 17458; # 17459

Figure 4.19: # 17471

Figure 4.21: # 17458

Figure 4.22: # 16951; # 17458; # 17459; # 17902

Figure 4.23: # 17572; # 17573; # 17579; # 17581; # 17582

Figure 4.24: # 17572; # 17573; # 17579; # 17581; # 17582

Figure 4.25: # 16961; # 17481

Figure 4.26: # 17480; # 17482

Figure 4.27: # 17471; # 17482

Figure 4.28: # 18046

Figure 4.29: # 18003; # 18004; # 18006; # 18008;

Figure 4.30: # 18009

Figure 4.31: # 18015

Figure 4.32: # 17792; # 17794

Figure 4.33: # 17794

Figure 4.34: # 17102; # 17160

Figure 4.35: # 17580; # 17570

Figure 4.36: # 17573; # 17574

Figure 4.37: # 17583

Figure 4.38: # 18059; # 18061; # 18065

Figure 4.39: # 17895; # 17897; # 18059; # 18061;

Figure 4.40: # 18061;

Figure 4.41: # 18059; # 18061; # 18065

Figure 4.43: # 17102; # 17459; # 17664; # 17665

Figure 4.44: # 17209; # 17779

Figure 4.45: # 17669; # 17676

Figure 4.46: # 17669; # 17676

Figure 4.47: # 17669

Figure 4.48: # 17673; # 17677

Figure 4.49: # 17676; # 17779; # 17787

Figure 4.50: # 17676; # 17779; # 17787

Figure 4.51: # 17676; # 17779; # 17787

Figure 4.52: # 17787; # 17788; # 17793; # 17795; # 18010; # 18078

Figure 4.53: # 17676; # 17677; # 17679; # 17684; # 17694

Figure 4.54: # 17677; # 17679; # 17684; # 17694

Figure 4.55: # 16951; # 17085; # 17086

Figure 4.56: # 16951; # 17085; # 17086

Figure 4.57: # 17086; # 17278

Figure 4.58: # 17690; # 17691; # 17693

Figure 4.59: # 17685; # 17695; # 17697

Figure 4.60: # 17697

Figure 4.61: # 17688; # 17692

Figure 4.62: # 17676; # 17688

Figure 4.63: # 17802

Figure 4.64: # 18006; # 18013

Figure 4.65: # 18047

Figure 4.66: # 18265

Figure 4.67: # 18048

Figure 4.68: # 18049; # 18051; # 18053; # 18054;

Figure 4.69: # 18074; # 18076; # 18077;

Figure 4.70: # 18080; # 18082; # 18083;

Figure 4.71: # 18083;

Figure 4.72: # 18015; # 18268 # 18270; # 18273

Figure 4.73: # 18015; # 18278 # 18279

Figure 4.74: # 18015; # 18267; # 18269; # 18274

Danksagung

Natürlich kann eine solche Arbeit nicht ohne die Hilfe anderer zustande kommen und erst durch eine gute Zusammenarbeit mit zahlreichen Kollegen erfolgreich werden. Zum Abschluss möchte ich mich daher an dieser Stelle sehr herzlich bei den Leuten bedanken, ohne deren Unterstützung diese Arbeit nicht hätte gelingen können:

Zunächst möchte ich mich bei Herrn Dr. habil. Wolfgang Stolz und Frau Prof. Dr. Kerstin Volz für die Möglichkeit bedanken in ihre Arbeitsgruppe forschen zu können. Vielen Dank für das Vertrauen und die Möglichkeit stets eigene Ideen umsetzten zu dürfen. Vielen Dank für die die gute Betreuung während der gesamten Zeit, die lehrreichen fachlichen Diskussionen und Anregungen und, dass ihre Türen bei Fragen und Problemen stets offen standen.

Herrn Prof. Dr. Wolfram Heimbrodt danke ich für die freundliche Übernahme des Zweitgutachtens meiner Arbeit.

Für die finanzielle Unterstützung in Form eines Promotionsstipendiums im Rahmen des Graduiertenkolleg "Funktionalisierung von Halbleitern" (GRK 1782) danke ich der Deutschen Forschungsgemeinschaft.

Bei Dr. Andreas Beyer bedanke ich mich für die vielfältige Unterstützung die ich während meiner Doktorarbeit erfahren durfte. Vielen Dank für die vielen Stunden, die du für mich am STEM verbracht hast, die zahlreichen Tassen Kaffee, die du nicht getrunken hast, um einen unfallfreien STM Transfer möglich zu machen und nicht zuletzt, dass du mir immer mit Rat und Tat zur Seite standest.

Bei Jürgen Belz, Zoe Bushell, Lennart Duschek, Dr. Rafael Fritz, Christian Lück, Dr. Jens Ohlmann und Patrick Sträßer, mit denen ich während meiner Zeit am STRL längerfristig ein Büro teilen durfte, bedanke ich mich für die vielen guten Stunden, die ich mit euch im Büro verbringen konnte und für die stets fröhliche aber immer auch konstruktive Atmosphäre. Ohne euch hätte die Arbeit nur halb so viel Spaß gemacht.

Dem Epitaxie-Team Dr. Henning Döscher, Christian Fuchs, Ulrike Häuplik, Dr. Philip Hens, Dr. Peter Ludewig, Lukas Nattermann, Stefan Reinhard, Antje Ruiz Perez, Eduard Sterzer und Michael Volk danke ich für die angenehme Atmosphäre im Labor, eure praktische und theoretischen Unterstützung bei Problemen und dafür, dass ich mich immer auf euch verlassen konnte, wenn ich mal Hilfe brauchte.

Bei Celina Becker, Dr. Andreas Beyer, Dr. Katharina Gries, Andrea Ott und Rainer Straubinger, möchte ich mich für die Präparation und die STEM- sowie SEM-Messungen an meinen Proben bedanken.

Celina Becker, Khaled El-Omar, Thomas Ochs, und Stefan Reinhard danke ich für die Unterstützung und schnelle Hilfe im Labor und dafür, dass ihr durch das morgendliche Starten der Schichten den Epitaxie-Leuten immer ein bisschen mehr Schlaf gönnt.

Isabelle Kimmel, Marina Koch und Elke Vaupel danke ich für die stets freundliche Unterstützung bei allen organisatorischen Fragen.

Allen Korrekturlesern, Dr. Andreas Beyer, Zoe Bushell, Dr. Henning Döscher, Lennart Duschek, Lucy Evans, Dr. Katharina Gries, Dr. Peter Ludewig, Lukas Nattermann, Eduard Sterzer, Helen Troup, Benjamin Uhlenbruck, Daniela Uhlenbruck, Leslie Uhlenbruck, Matthias Uhlenbruck, Stefanie Uhlenbruck und Thomas Uhlenbruck danke ich für ihre schnelle Hilfe, die konstruktive Kritik an und die guten Anregungen zu meiner Arbeit.

Zahlreichen Mitgliedern aus anderen Arbeitsgruppen, besonders Sebastian Gies, Dr. Uwe Kaiser, Dr. Gerson Mette, Jan Oliver Oelerich, Marcel Reutzel und Andraes Stegmüller danke ich für die Unterstüzung, gute Zusammenarbeit und lehrreichen Gespräche am STM, Raman und in theoretischen Fragen.

Den genannten und allen anderen Mitgliedern des STRL, die ich während meiner Arbeit hier kennenlernen durfte, danke ich für die schöne Zeit, die ich während aber auch außerhalb der Arbeit mit euch verbringen konnte.

Zuletzt möchte ich mich noch bei meinen Freunden und ganz besonders bei meiner Familie bedanken, ohne die ich niemals so weit hätte kommen können. Vielen Dank für jegliche Art von Unterstützung, die ich während meines Studiums immer von euch erfahren habe. Vielen Dank für euer Verständniss und, dass ihr immer aufmunternden Worte für mich gefunden habt, wenn ich sie nötig hatte.